LAWRENCE
LIVERMORE
NATIONAL
LABORATORY

LLNL-TR-814964

Shell Element Material Model Verification Problems for DYNA3D: Part II

Brian D. Giffin

September 28, 2020

This work was performed under the auspices of the U.S. Department of Energy by Lawrence Livermore National Laboratory under Contract DE-AC52-07NA27344.

Abstract

A suite of supplementary shell element material model verification tests were developed for the explicit finite element program DYNA3D, in continuation of the work performed in LLNL-TR-792469 (Shell Element Material Model Verification Problems for DYNA3D). The testing procedure developed in the preceding report is extended, and used to verify all remaining untested shell model features and inputs. A collection of 78 feature-specific verification tests are proposed, some of which are applicable to multiple material models, though many are specialized to a particular model. The collective suite of tests cover all 27 currently available material models in DYNA3D. In the course of developing the proposed test suite, 24 separate shell model-related issues were identified and have subsequently been resolved.

Contents

Shell Element Material Model Verification Problems for DYNA3D: Part II

Brian Giffin
Methods Development Group
Defense Technologies Engineering Division
Engineering Directorate

September 28, 2020

1 Introduction

In the preceeding work [3], a generic testing framework was developed to facilitate the creation of shell element material model verification problems for DYNA3D. This framework was then employed to develop a series of "feature-specific" verification tests applicable to different material models sharing particular features in common (e.g. orthotropic elasticity, or linear hardening plasticity). Consequently, the generic behavior of most shell material models in DYNA3D was successfully verified, but a number of model-specific features were left untested. Because many of the available material models for shell elements in DYNA3D possess unique features with commensurate input parameterizations, individual tests specific to each material model are required to verify these features.

The present work serves as a continuation of [3], with the aim of developing a compresensive suite of shell element material model verification tests in DYNA3D, covering all previously untested model-specific features. In keeping with the previous work, nearly all of the proposed tests admit a mathematically derived exact solution, against which the implementation of a given model-specific feature can be directly and quantitatively verified.

Section 2 of this report presents a brief overview of the existing material models currently available for use with shell elements in DYNA3D, and a high-level summary of the available "features" provided by each model. The resulting catalog of features forms the basis for the proposed test suite, with each test focusing on the verification of a specific model feature of interest.

Section 3 breifly reviews the generic problem setup and verification methodology introduced in [3], and makes note of relevant extensions of the aforementioned framework for the newly proposed set of verification problems.

Section 4 presents the newly proposed suite of verification tests, consisting of: a description of each model feature being verified; the definition of all problems designed to test a given feature; the derivation of corresponding reference solutions, as appropriate; and the presentation/comparison of the numerical results obtained for each test applied to every relevant material model.

Section 5 concludes with a tabulated presentation of the verification status of all tested model features, and a catalog of all issues that were discovered (and resolved) in the course of this work.

2 Overview of DYNA3D's Shell Element Material Models

Table 1: Index of shell element-specific material models.

Model	Name
1	Elastic
2	Orthotropic Elastic
3	Kinematic/Isotropic Elastic-Plastic
4	Thermo-Elastic-Plastic
12	Isotropic-Elastic-Plastic
15	Johnson/Cook Elastic-Plastic
18	Power Law Isotropic Elastic-Plastic
19	Strain Rate Dependent Isotropic Elastic-Plastic
21	Thermal Orthotropic Elastic
22	Fiber Composite with Damage
23	Thermal Orthotropic Elastic with Variable Properties
24	Rate-Dependent Isotropic Elastic-Plastic
28	Resultant Plasticity
30	Closed-Form Update Elastic-Plastic for Shells
33	General Anisotropic Elastic-Plastic
34	Normal Anisotropic Elastic-Plastic for Shells
35	Elasto-Plastic with Forming Limit Diagram
38	Bammann Plasticity Model
39	Sandia Damage Model
41	Fabric with Damage
42	Multi-Material Shell Element Model
46	Anisotropic Elastic (calls subroutine for model 2)
50	Braided Composite Model with Damage
52	Rate-Dependent Tabular Elastic-Plastic with Fracture
54	Zerilli-Armstrong Elasto-Plasticity with Fracture
71	General Elasto-Plastic with Optional Rate & Temperature Dependence
74	Laminated Composite with Damage

DYNA3D supports a broad range of different shell element formulations and material models. Currently, a total of 27 different material models are available for use with shell elements, enumerated in table 1. Henceforth, all material models will be referred to by their corresponding model number. For the complete enumeration of all input parameters – and a detailed description of the formulation for each model, the reader is referred to the DYNA3D manual [5].

It is emphasized that the primary goal of the proposed tests is to verify the correct implementation of each material model – not the individual shell element formulations, nor their kinematics. To this end, a number of simple single-element test problems were devised in [3] and reiterated in section 3.1 for the sake of comparing the computed stress state in the element to exact reference solutions, given known kinematic inputs.

2.1 Available Material Model Features for Shell Elements

Several of the available shell models share a number of similar features in common with one another. In such cases, a collection of general tests are created which may each be used to verify all models that implement the same feature. Nonetheless, there exist a variety of unique features specific to certain models which must be tested on their own. In these cases, feature-specific tests are devised for the model in question.

Table 2 summarizes the collection of verification tests for shell element material models that were proposed and implemented in the previous work [3]. In comparison, table 3 provides an overview of the newly proposed suite of tests presented in this report, covering all remaining features for shell element material models not addressed in [3].

Table 2: DYNA3D shell material model features tested in [3]

Model	Isotropic Elasticity	Orthotropic Elasticity	Isotropic Thermal Expansion	Orthotropic Thermal Expansion	Linear Hardening	Piecewise Hardening	Power-Law Hardening	Exponential Hardening	Hill Yield Criterion	Linear Rate-Hardening	Logarithmic Rate-Hardening	Drucker-Prager Yield Criterion
1	✓	-	-	-	-	-	-	-	-	-	-	-
2	✓	✓	-	-	-	-	-	-	-	-	-	-
3	✓	-	-	-	✓	-	-	-	-	-	-	-
4	✓	-	✓	-	✓	-	-	-	-	-	-	-
12	✓	-	-	-	✓	-	-	-	-	-	-	-
15	✓	-	-	-	✓	-	✓	-	-	-	-	✓
18	✓	-	-	-	-	-	✓	-	-	-	-	-
19	✓	-	-	-	✓	-	-	-	-	-	-	-
21	✓	✓	✓	✓	-	-	-	-	-	-	-	-
22	✓	✓	-	-	-	-	-	-	-	-	-	-
23	✓	✓	✓	✓	-	-	-	-	-	-	-	-
24	✓	-	-	-	✓	✓	✓	-	-	✓	-	✓
28	✓	-	-	-	✓	-	-	-	-	-	-	-
30	✓	-	-	-	✓	-	-	-	-	-	-	-
33	✓	✓	-	-	✓	-	-	-	✓	-	-	-
34	✓	-	-	-	✓	-	-	-	✓	-	-	-
35	✓	-	-	-	✓	✓	-	-	-	-	-	-
38	✓	-	-	-	✓	-	-	-	-	-	-	-
39	✓	-	-	-	✓	-	-	-	-	-	-	-
41	✓	✓	-	-	-	-	-	-	-	-	-	-
42	-	-	-	-	-	-	-	-	-	-	-	-
46	✓	✓	-	-	-	-	-	-	-	-	-	-
50	✓	✓	-	-	-	-	-	-	-	-	-	-
52	✓	-	-	-	✓	✓	-	-	-	-	-	-
54	✓	-	-	-	✓	-	✓	-	-	✓	-	-
71	✓	-	✓	-	✓	-	✓	✓	-	✓	✓	✓
74	✓	✓	-	-	-	-	-	-	-	-	-	-

✓: Verification tests have been created for this model feature.
✗: Model feature currently remains untested.

Table 3: Summary of newly proposed tests for shell material models in DYNA3D

Model	Kinematic Hardening (4.1)	Temp.-Dependent Elasticity (4.2.1)	Temp.-Dependent CTE (4.2.2)	Temp.-Dependent Plasticity (4.2.3-4.2.5)	Heat Generation & Softening (4.2.6)	Strain Rate-Dependent Plasticity (4.3)	Bammann Plasticity (4.4)	Minimum Time Step Deletion (4.5.1)	Plastic Strain Deletion (4.5.2)	Instantaneous Failure (4.5.3-4.5.6)	Progressive Damage (4.5.7-4.5.10)	Shear Correction Factor (4.6.1)	Material Axes Options (4.6.3)	Debug Run (4.6.4)	Non-linear Shear (4.6.5)	Kinematic Formulation (4.6.6)	Misc. (4.6.7-4.6.10)
1	-	-	-	-	-	-	-	-	-	-	-	✓	-	-	-	-	-
2	-	-	-	-	-	-	-	-	-	-	-	✓	✓	✓	-	-	-
3	✓	-	-	-	-	-	-	-	-	-	-	✓	-	-	-	-	-
4	-	✓	✓	✓	-	-	-	-	-	-	-	✓	-	-	-	-	-
12	-	-	-	-	-	-	-	-	-	-	-	✓	-	-	-	-	-
15	-	-	-	✓	✓	✓	-	✓	-	✓	-	✓	-	-	-	-	✓
18	-	-	-	-	-	-	-	-	✓	-	-	✓	-	-	-	-	-
19	-	-	-	-	-	✓	-	✓	-	✓	-	✓	-	-	-	-	-
21	-	-	-	-	-	-	-	-	-	-	-	✓	✓	-	-	-	-
22	-	-	-	-	-	-	-	✓	-	✓	-	✓	✓	-	✓	-	-
23	-	✓	✓	-	-	-	-	-	-	-	-	✓	✓	-	-	-	✓
24	-	-	-	-	-	-	-	✓	✓	-	-	✓	-	-	-	-	-
28	-	-	-	-	-	-	-	-	-	-	-	✓	-	-	-	-	-
30	✓	-	-	-	-	-	-	-	-	-	-	✓	-	-	-	-	-
33	-	-	-	-	-	-	-	-	-	-	-	✓	✓	-	-	-	-
34	-	-	-	-	-	-	-	-	-	-	-	✓	-	-	-	-	-
35	-	-	-	-	-	✓	-	-	✓	✓	-	✓	-	-	-	-	-
38	✓	-	-	-	✓	-	✓	-	-	-	-	✓	-	-	-	-	-
39	✓	-	-	-	✓	-	✓	-	-	-	✓	✓	-	-	-	-	-
41	-	-	-	-	-	-	-	✓	-	✓	-	✓	✓	-	✓	✓	✓
42	-	-	-	-	-	-	-	-	-	-	-	-	-	-	-	-	-
46	-	-	-	-	-	-	-	-	-	-	-	✓	✓	✓	-	-	-
50	-	-	-	-	-	-	-	✓	-	-	✓	✓	✓	-	-	✓	-
52	-	-	-	-	✓	✓	-	✓	✓	-	✓	✓	-	-	-	-	✓
54	-	-	-	✓	✓	✓	-	✓	✓	-	-	✓	-	-	-	-	-
71	-	-	✓	✓	✓	-	-	-	✓	-	-	✓	-	-	-	-	-
74	-	-	-	-	-	-	-	-	-	-	✓	✓	✓	-	-	-	-

✓: Verification tests have been created for this model feature.
✗: Model feature currently remains untested.

3 Review of the Generic Verification Testing Procedures

As described in [3], the generic single-element test problem reviewed in section 3.1 is employed by most of verification tests presented in this report. Particular specializations of the generic test are devised to establish a finite number of parameterized motions, termed "load cases." Each of the verification tests proposed in this report is identified by an assigned load case, and a corresponding material parameterization. The numerical results of each test are then analyzed according to the methodology reviewed in section 3.2.

3.1 Single-Element Test Setup

Unless otherwise noted, a square, planar quadrilateral element is henceforth considered for all test problems, as depicted in Figure 1. For convenience, $L = 1.0$ such that the element's isoparametric parent coordinates $\boldsymbol{\xi}$ coincide with the physical coordinates $\mathbf{X}$ of the element in its (undeformed) reference configuration. Furthermore, the element is prescribed to have unit thickness, and the time interval $t \in [0, 1]$ over which each test problem takes place is also assumed to have unit duration.

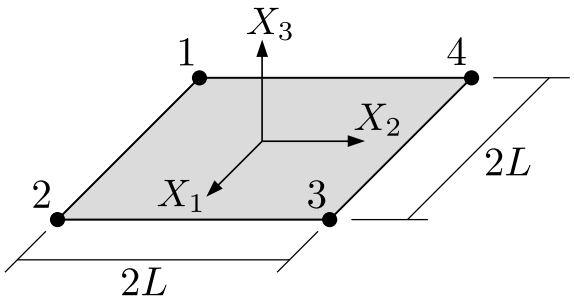

Figure 1: Single quadrilateral shell element used in all verification tests.

The kinematics resulting from the prescribed motions discussed in [3] result in the following kinematic input strain rate (minus the thickness strain component):

$$\dot{\boldsymbol{\varepsilon}}_u(t) + \dot{\boldsymbol{\varepsilon}}_\theta(t), \tag{1}$$

where

$$\boldsymbol{\varepsilon}_u(t) = [\epsilon(t) + \gamma(t)]\, \mathbf{q}_1 \otimes \mathbf{q}_1 + [\epsilon(t) - \gamma(t)]\, \mathbf{q}_2 \otimes \mathbf{q}_2, \tag{2}$$

$$\boldsymbol{\varepsilon}_\theta(t) = -\frac{1}{2}\theta_1(t)\,(\mathbf{e}_2 \otimes \mathbf{e}_3 + \mathbf{e}_3 \otimes \mathbf{e}_2) + \frac{1}{2}\theta_2(t)\,(\mathbf{e}_1 \otimes \mathbf{e}_3 + \mathbf{e}_3 \otimes \mathbf{e}_1)\,, \tag{3}$$

$$\mathbf{Q} = \begin{bmatrix} \mathbf{q}_1 & \mathbf{q}_2 & \mathbf{q}_3 \end{bmatrix} = \begin{bmatrix} \cos\alpha & -\sin\alpha & 0 \\ \sin\alpha & \cos\alpha & 0 \\ 0 & 0 & 1 \end{bmatrix} \quad \forall \alpha \in \left\{ \alpha \in \mathbb{R} \,:\, \alpha = \frac{n\pi}{4}\, \forall n \in \mathbb{Z} \right\}. \tag{4}$$

In the preceding expressions, $\boldsymbol{\varepsilon}_u$ denotes the in-plane Hencky (or logarithmic) strain tensor, while $\boldsymbol{\varepsilon}_\theta$ denotes the small strain tensor containing only the transverse shear terms.

3.1.1 Definition of Load Cases

Using the generic test setup previously established, a finite set of "load cases" which can be modulated by one or two scalar parameters are devised. Parameterized load cases of common interest are presented in table 4, and depicted graphically in figure 2.

For the majority of load cases described in table 4, the parameter $\bar{\gamma}$ denotes the constant strain rate (as well as the final value of total strain at $t = 1$) of one or more strain components, whereas the parameters T_0 and $\bar{T}$ denote the initial temperature and constant rate of temperature increase, respectively.

Load cases 1 and 7 are volume-changing deformations which produce a hydrostatic component within the overall state of stress. Load cases 2, 3, 4, 5, and 6 produce volume-preserving deformations, which for

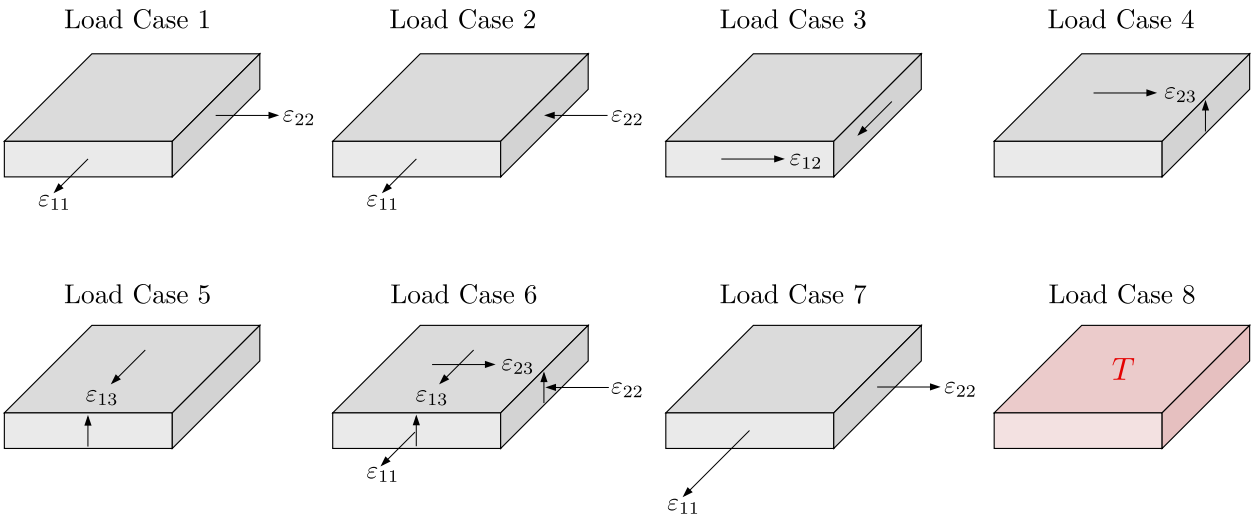

Figure 2: Depiction of all load cases for the generic single-element test setup.

Table 4: Summary of all load cases for the generic single-element test setup

Load Case	$\epsilon(t)$	$\gamma(t)$	$\theta_1(t)$	$\theta_2(t)$	α	$T(t)$	Description
1	$\bar{\gamma}\,t$	0	0	0	0	T_0	Isotropic in-plane expansion ($\dot{\varepsilon}_{11} = \dot{\varepsilon}_{22} = \bar{\gamma}$)
2	0	$\bar{\gamma}\,t$	0	0	0	T_0	Isochoric in-plane extension ($\dot{\varepsilon}_{11} = -\dot{\varepsilon}_{22} = \bar{\gamma}$)
3	0	$\bar{\gamma}\,t$	0	0	$\pi/4$	T_0	Pure in-plane shear ($\dot{\varepsilon}_{12} = \bar{\gamma}$)
4	0	0	$-2\bar{\gamma}t$	0	0	T_0	Pure transverse shear ($\dot{\varepsilon}_{23} = \bar{\gamma}$)
5	0	0	0	$2\bar{\gamma}t$	0	T_0	Pure transverse shear ($\dot{\varepsilon}_{13} = \bar{\gamma}$)
6	0	$\bar{\gamma}t$	$-2\bar{\gamma}t$	$2\bar{\gamma}t$	0	T_0	Combined shear ($\dot{\varepsilon}_{11} = -\dot{\varepsilon}_{22} = \dot{\varepsilon}_{23} = \dot{\varepsilon}_{13} = \bar{\gamma}$)
7	$3\bar{\gamma}t$	$\bar{\gamma}t$	0	0	0	T_0	Biaxial stretching ($\dot{\varepsilon}_{11} = 2\dot{\varepsilon}_{22} = 4\bar{\gamma}$)
8	0	0	0	0	0	$T_0 + \bar{T}t$	Static heating ($\dot{T} = \bar{T}$)

isotropic materials result in a purely deviatoric state of stress, and proportional loading conditions for von Mises plasticity models. Load case 6 in particular is used extensively by the various plasticity tests because it engages most of the components of the stress tensor in the computation of the effective stress. Load case 8 is used by tests involving thermal expansion, inducing changes in the normal strain and in-plane stress components due to heating.

3.1.2 Material Parameterizations

In addition to a prescribed load case, each test is assigned a set of relevant material parameters (as discussed in [3]), typically enumerated in a tabular format. For some of the generic test collections proposed in this report, similar tests within a grouped collection are defined to share a core set of common parameter values, but each test may introduce or vary additional parameters, as needed. To avoid repetition, partial parameterizations of a given model may be provided in separate tables, such that the complete parameterization for a given test is assumed from the union of all relevant parameters.

3.2 Numerical Analysis of the Test Results

To verify the implementation of each material model, verification tests are created by first postulating a relatively simple problem designed to isolate and independently verify a single model feature (e.g. isotropic linear hardening plasticity). For each test, an exact mathematical solution is derived to be consistent with the theoretical formulation of the model feature of interest. With an exact solution in hand for a given

test problem, the numerical solution computed by a specific material model in DYNA3D can be directly compared to the exact solution and verified through the evaluation of several appropriately chosen error metrics, originally defined in [3] and reiterated in the following sub-section.

3.2.1 Definition of Error Measures

The primary scalar- and tensor-valued relative (and absolute) error metrics of interest for all verification problems are established in [3], and restated below:

$$e^{\text{rel}}_{L^2}(f) \equiv \frac{e^{\text{abs}}_{L^2}(f)}{||f^{\text{model}}(t)||_{L^2}} \qquad e^{\text{abs}}_{L^2}(f) \equiv ||f^{\text{model}}(t) - f^{\text{exact}}(t)||_{L^2}, \qquad \forall f(t) \in C^0([0,1]), \tag{5}$$

$$e^{\text{rel}}_{L^2}(\mathbf{A}) \equiv \frac{e^{\text{abs}}_{L^2}(\mathbf{A})}{||\mathbf{A}^{\text{model}}(t)||_{L^2}} \qquad e^{\text{abs}}_{L^2}(\mathbf{A}) \equiv ||\mathbf{A}^{\text{model}}(t) - \mathbf{A}^{\text{exact}}(t)||_{L^2}, \qquad \forall \mathbf{A}(t) \in \left[C^0([0,1])\right]^{3\times 3}, \tag{6}$$

where superscripted text is used to distinguish between the "exact" solutions for a given quantity of interest and the approximate values computed numerically by a given material "model," and between the "absolute" and "relative" (normalized) measures of solution error. The reader is referred to [3] for additional details regarding these errors measures and their intuitive significance.

In the vast majority of cases, the generic scalar- (f) or tensor-valued quantity ($\mathbf{A}$) of interest is taken to be a function of time t. However, for select problems (namely in section 4.6.10), the quantity of interest is instead a function of some generic variable x. Nonetheless, the meaning of the chosen L^2 error measures remains unchanged in this context, although the particular domain of $x \in X$ may be different from $t \in [0,1]$.

For most tests, the accuracy of a given material model is determined by examining the errors in the complete time-history for the stress $\boldsymbol{\sigma}(t)$, the normal strain $\varepsilon_{33}(t)$, and the equivalent plastic strain $\bar{\varepsilon}^p(t)$ variables. A handful of tests (namely those in section 4.6.10) measure the error in model-specific quantity. For a given problem, if the exact solution for a particular quantity is identically zero for all time (e.g. if $\bar{\varepsilon}^p(t) = 0\,\forall t \iff ||\bar{\varepsilon}^p(t)||_{L^2} = 0$), the absolute error metric is used. Otherwise, the relative error metric is examined. For sufficiently refined time discretizations, it is expected that – when used in the aforementioned contexts – both metrics should produce errors on the order of machine precision (i.e. $e^{\text{rel/abs}}_{L^2}(\cdot) \approx 10^{-16}$). Larger errors may nonetheless persist with slower rates of convergence, as discussed in the following sub-section.

3.2.2 Error Estimation and Convergence Analysis

To distinguish between sources of temporal discretization error (discussed in greater detail in [3]) and potential inconsistencies in the implementation of a given model, the rate of convergence in a given error metric is examined under temporal refinement. An implementation error may be indicated either by a reduced rate of convergence compared to the theoretical rate for the dominant source of discretization error, or by a sudden loss of convergence below a certain threshold for Δt.

Given an upper bound on the measured L^2 error norm of the form:

$$e^{\text{rel/abs}}_{L^2}(\cdot) < C\,\Delta t^r, \tag{7}$$

for some $C > 0$, the value of r denotes the corresponding "rate of convergence" in $e^{\text{rel/abs}}_{L^2}(\cdot)$ with respect to the (assumed uniform) time step size Δt.

"Sufficient convergence" for most model features (particularly those pertaining to damage and failure) is herein defined to mean: convergence at a consistent rate across all chosen values of Δt. Given the wide variability in model features and their implementations, lower bounds on the numerical rate of convergence are less relevant for the present suite of tests. This contrasts with the work performed in [3], wherein bounded estimates were derived for specific model features and used to verify the measured rates of convergence.

In some rare cases, a negative rate of convergence with respect to increasing temporal refinement may be observed (as in section 4.6.6). Provided such behavior can be rationalized by a standard truncation error analysis, this may yet indicate that a given model is behaving as expected, according to its intended

numerical implementation. For the pupose of this work, such models are assigned a passing verification status. However, it is advised that these model features be revisited at a later time to address an apparent numerical stability issue.

4 Summary of Newly Proposed Verification Tests

This section of the report provides a comprehensive summary of all newly proposed tests to be added to the existing verification suite for shell element material models in DYNA3D. The presentation of the test suite is organized into collections of tests designed to verify individual model features, potentially shared between multiple material models. Each subsection provides a brief theoretical overview of a specific model feature of interest (e.g. kinematic hardening plasticity), along with a summary of the test(s) developed to verify the implementation of all relevant material models.

Each individual test is defined by its assigned load case (described in section 3.1.1), and its corresponding material parameterization (described in section 3.1.2). For brevity, collections of tests which share the same load case and/or material parameterization are noted as such up front.

For each test, closed-form reference solutions are derived to be consistent with the underlying mathematical theory for each model feature. The numerical results for each test are compared between all material models which implement the tested feature of interest, and against the mathematically derived reference solution. Solution errors in the $e^{\text{rel}}_{L^2}(\cdot)$ metric (or in the $e^{\text{abs}}_{L^2}(\cdot)$ metric when $e^{\text{rel}}_{L^2}(\cdot)$ is undefined) for the stress $\boldsymbol{\sigma}(t)$, the normal strain $\varepsilon_{33}(t)$, and the equivalent plastic strain $\bar{\varepsilon}^p(t)$ are examined for a highly refined time discretization of the problem, i.e. $\Delta t = 10^{-4}$.

The convergence of each error metric under temporal refinement is also examined across four different time discretizations, namely: $\Delta t \in \left\{10^{-1}, 10^{-2}, 10^{-3}, 10^{-4}\right\}$. Error convergence plots and the measured rates of convergence are presented for the sake of comparison between different models, and against the estimated theoretical convergence rate, where applicable. In certain cases, the error across all refinement levels is either identically zero or is on the order of machine precision for double precision arithmetic ($e^{\text{abs/rel}}_{L^2}(\cdot) \approx 10^{-16}$), and no further convergence can be obtained through temporal refinement. In such cases, the computed rate of convergence is not displayed in the tabulated results for the corresponding test.

In the course of creating the proposed suite of verification tests, a number of bugs were discovered and fixed. The complete list of resolved issues is presented at the end of the report, in section 5.1. Despite these efforts, a few discrepancies remain which are recognized (and in some cases quantified) to be the result of model-specific assumptions that are inconsistent with the theory employed by most other models in DYNA3D. In such cases, comparatively large errors or slow convergence rates in the tabulated results for each test are highlighted in red. A cautionary note is provided, and a recommendation is given regarding the scope of work required to properly address the observed inconsistencies.

Along with the tabulated results for each test, the verification "status" of each model is indicated symbolically using one of the following characters:

- ✓: The indicated model feature has been verified and is functioning properly.
- ⚠: The indicated model feature is functioning as intended, but makes an assumption that is inconsistent with most other models in DYNA3D.
- ✗: The indicated model feature is not functioning properly.

4.1 Kinematic Hardening Plasticity

Models 3, 30, 38, and 39 incorporate kinematic hardening with a tensorial back stress variable $\boldsymbol{\alpha}$. In particular, models 3 and 30 support linear kinematic hardening, with model 30 additionally operating under the assumption of plane stress conditions. In comparison, models 38 and 39 possess additional rate-dependencies and recovery terms governing the evolution of the back stress variable, but for select parameterizations these models likewise reproduce the behavior of linear kinematic hardening.

For the specialized (cylic) load case yielding $\varepsilon_{11}(t) = \varepsilon_{22}(t) = \log(L + \bar{u}\sin(\omega t))$ with $L = 1.0$ (arising from the specification of periodic nodal velocities $\mathbf{v}_a = \mathbf{X}_a \bar{u}\omega\cos(\omega t)$), and for the material parameterization given in table 5, one obtains a stress history driven according to

$$\boldsymbol{\sigma}(t) = E\left(\boldsymbol{\varepsilon}(t) - \boldsymbol{\varepsilon}^p(t)\right), \qquad \boldsymbol{\alpha}(t) = \frac{2}{3}E_p\,\boldsymbol{\varepsilon}^p(t), \qquad \boldsymbol{\varepsilon}^p(t) = \varepsilon_{33}(t)\,\mathbf{n}, \qquad \dot{\bar{\varepsilon}}^p = |\dot{\varepsilon}_{33}|, \tag{8}$$

where

$$\mathbf{n} = \begin{bmatrix} \frac{1}{2} & 0 & 0 \\ 0 & \frac{1}{2} & 0 \\ 0 & 0 & -1 \end{bmatrix}, \tag{9}$$

such that

$$\bar{\sigma}(t) = |E\varepsilon_{11}(t) + (E/2 + E_p)\,\varepsilon_{33}(t)| \leq \sigma_0. \tag{10}$$

During tensile/compressive plastic loading, the normal strain component evolves respectively as:

$$\varepsilon_{33}(t) = \frac{-E\varepsilon_{11}(t) - \sigma_0}{E/2 + E_p}, \qquad \varepsilon_{33}(t) = \frac{-E\varepsilon_{11}(t) + \sigma_0}{E/2 + E_p}. \tag{11}$$

For the prescribed motion, the periodic times at which the minimum/maximum strain occurs are given by

$$t_{\min} = \frac{4\pi k - \pi}{2\omega} \quad \forall k \in \mathbb{Z}, \qquad t_{\max} = \frac{4\pi k + \pi}{2\omega} \quad \forall k \in \mathbb{Z}. \tag{12}$$

Additionally, the time of first yielding under tensile loading occurs at

$$t_0 = \frac{1}{\omega}\sin^{-1}\left(\frac{1}{\bar{u}}\left[e^{\sigma_0/E} - L\right]\right), \tag{13}$$

whereas the periodic times at which yielding initiates thereafter under cyclic compressive/tensile loading are determined by:

$$t_- = \frac{1}{\omega}\sin^{-1}\left(\frac{1}{\bar{u}}\left[e^{\varepsilon_{11}(t_{\max}) - 2\sigma_0/E} - L\right]\right), \qquad t_+ = \frac{1}{\omega}\sin^{-1}\left(\frac{1}{\bar{u}}\left[e^{\varepsilon_{11}(t_{\min}) + 2\sigma_0/E} - L\right]\right). \tag{14}$$

The results of the kinematic hardening plasticity test under the aforementioned cyclic loading conditions are provided in table 6 and figure 3, confirming the correct behavior of all models with sufficient accuracy and convergence characteristics under temporal refinement.

Table 5: Material parameterization for the kinematic hardening plasticity test

Parameter	Value
Elastic modulus, E	2.0
Poisson's ratio, ν	0.0
Yield stress, σ_0	0.1
Tangent modulus, E_T	0.4
Hardening parameter, β	0.0 (pure kinematic hardening)

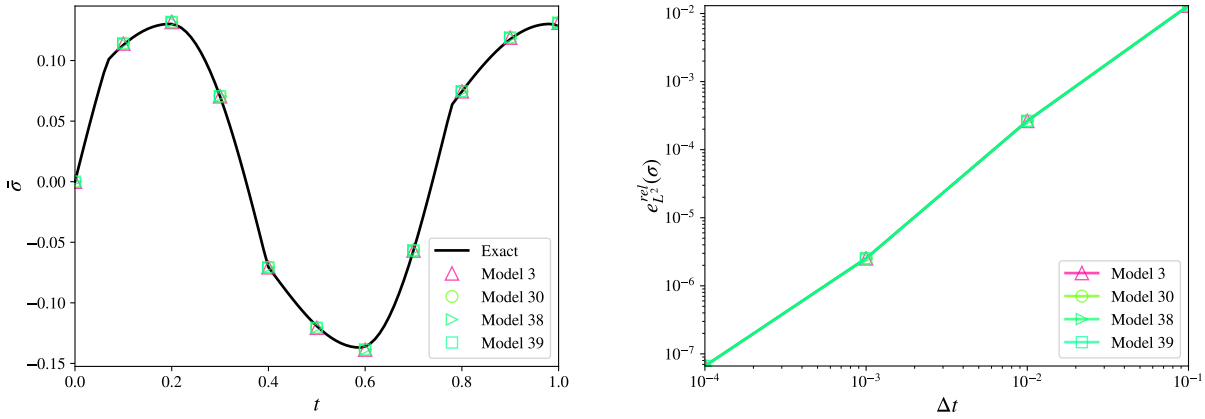

(a) Time-history plot of $\bar{\sigma}$ vs. t using $\Delta t = 0.1$.

(b) Convergence plot for $e^{\text{rel}}_{L^2}(\boldsymbol{\sigma})$ errors vs. Δt.

Figure 3: Kinematic hardening plasticity test.

Table 6: Computed errors for the kinematic hardening plasticity test.

Model	$e^{\text{rel}}_{L^2}(\boldsymbol{\sigma})$	r	$e^{\text{rel}}_{L^2}(\varepsilon_{33})$	r	$e^{\text{rel}}_{L^2}(\bar{\varepsilon}^p)$	r	Status
3	6.634e-08	1.58	8.756e-08	1.74	9.084e-08	1.32	✓
30	6.634e-08	1.58	8.756e-08	1.74	9.084e-08	1.32	✓
38	6.636e-08	1.58	8.743e-08	1.74	9.094e-08	1.32	✓
39	6.636e-08	1.58	8.743e-08	1.74	9.094e-08	1.32	✓

4.2 Temperature-Dependent Material Properties

Several material models allow for the specification of temperature-dependent elasticity, thermal expansion, or plasticity properties. Where possible, the behavior of a given temperature-dependent material property is verified by specifying a constant (non-zero) temperature time-history, specifically: $T(t) = \bar{T} \, \forall t$. The indicated temperature-varying material properties thus assume their (constant in time) values evaluated at $\bar{T}$, and the behavior of each temperature-depenent model is therefore consistent with the results of an equivalent temperature-invariant model. In most cases, the value of a given temperature-dependent material parameter at $T = \bar{T}$ is dictated by the corresponding material parameterization for the relevant temperature-invariant test presented in [3]. The results should therefore be identical to the original temperature-invariant test, which are used to directly verify the temperature-dependent behavior of each corresponding feature, wherever possible.

4.2.1 Temperature-Dependent Elasticity

Models 4 and 23 respectively possess isotropic and anisotropic elastic properties which may be independently varied with temperature. Isotropic elasticity tests 1-5 (described in [3]) are used to verify the temperature-dependent behavior of these properties (summarized in table 7) at a constant temperature of $T = 1 \, \forall t$. The results are presented in tables 8-12 and figures 4-8, demonstrating the anticipated behavior consistent with the original suite of temperature-invariant elasticity tests.

Table 7: Material parameterization for the temperature-dependent isotropic elasticity tests

Parameter	Value
Tabulated temperatures, T	{0.0, 1.0}
Tabulated elastic moduli, E	{15.0, 7.5}
Tabulated Poisson's ratios, ν	{0.375, 0.25}

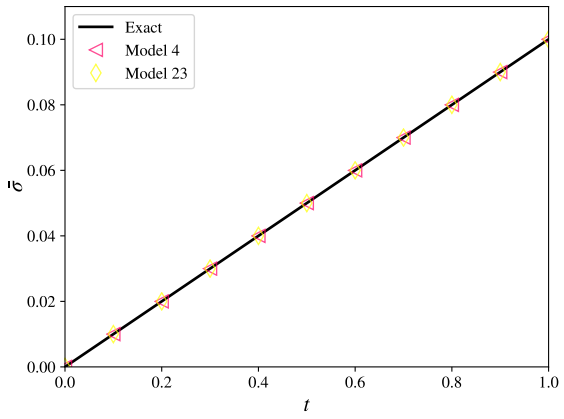

(a) Time-history plot of $\bar{\sigma}$ vs. t using $\Delta t = 0.1$.

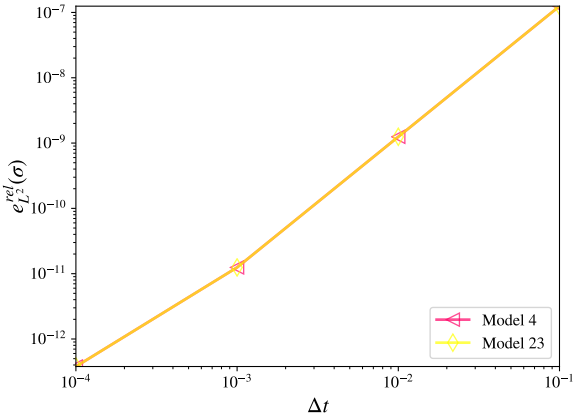

(b) Convergence plot for $e^{\text{rel}}_{L^2}(\boldsymbol{\sigma})$ errors vs. Δt.

Figure 4: Temperature-dependent isotropic elasticity test 1.

Table 8: Computed errors for temperature-dependent elasticity test 1.

Model	$e^{\text{rel}}_{L^2}(\boldsymbol{\sigma})$	r	$e^{\text{rel}}_{L^2}(\varepsilon_{33})$	r	$e^{\text{abs}}_{L^2}(\bar{\varepsilon}^p)$	r	Status
4	3.790e-13	1.52	1.822e-13	1.84	0.000e+00	-	✓
23	3.789e-13	1.52	1.822e-13	1.84	0.000e+00	-	✓

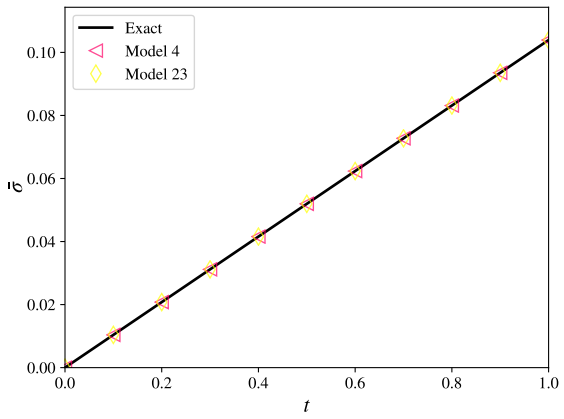

(a) Time-history plot of $\bar{\sigma}$ vs. t using $\Delta t = 0.1$.

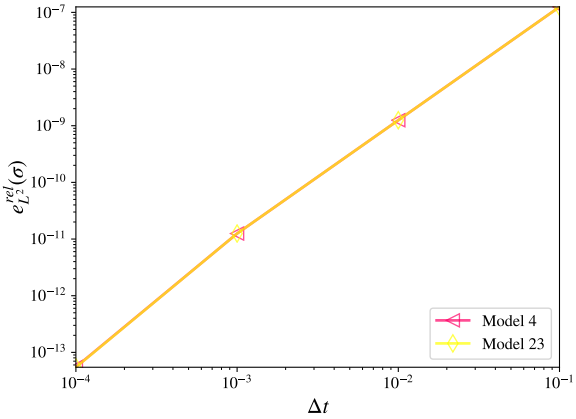

(b) Convergence plot for $e^{\text{rel}}_{L^2}(\boldsymbol{\sigma})$ errors vs. Δt.

Figure 5: Temperature-dependent isotropic elasticity test 2.

Table 9: Computed errors for temperature-dependent elasticity test 2.

Model	$e^{\text{rel}}_{L^2}(\boldsymbol{\sigma})$	r	$e^{\text{abs}}_{L^2}(\varepsilon_{33})$	r	$e^{\text{abs}}_{L^2}(\bar{\varepsilon}^p)$	r	Status
4	5.519e-14	2.00	6.274e-18	-	0.000e+00	-	✓
23	5.466e-14	2.00	3.568e-17	-	0.000e+00	-	✓

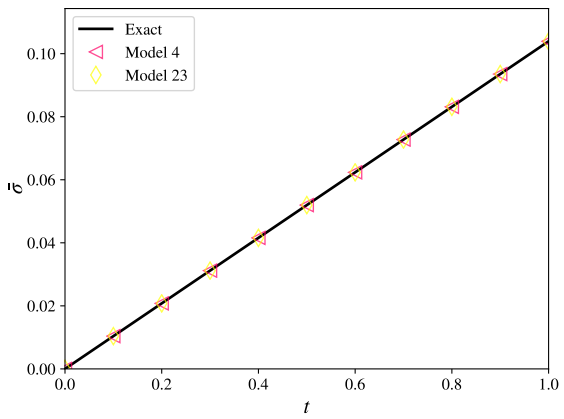

(a) Time-history plot of $\bar{\sigma}$ vs. t using $\Delta t = 0.1$.

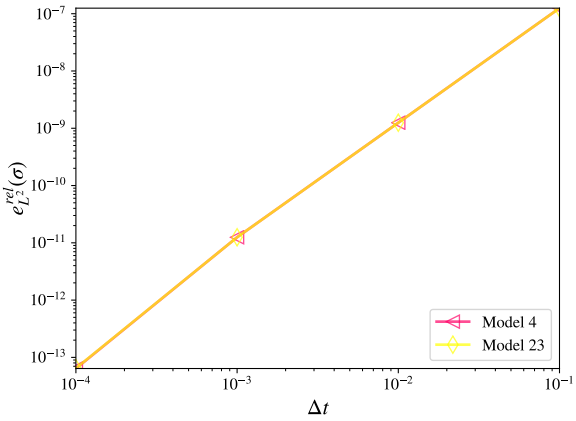

(b) Convergence plot for $e_{L^2}^{\text{rel}}(\boldsymbol{\sigma})$ errors vs. Δt.

Figure 6: Temperature-dependent isotropic elasticity test 3.

Table 10: Computed errors for temperature-dependent elasticity test 3.

Model	$e_{L^2}^{\text{rel}}(\boldsymbol{\sigma})$	r	$e_{L^2}^{\text{abs}}(\varepsilon_{33})$	r	$e_{L^2}^{\text{abs}}(\bar{\varepsilon}^p)$	r	Status
4	6.392e-14	2.00	6.217e-18	-	0.000e+00	-	✓
23	6.460e-14	2.00	1.558e-17	-	0.000e+00	-	✓

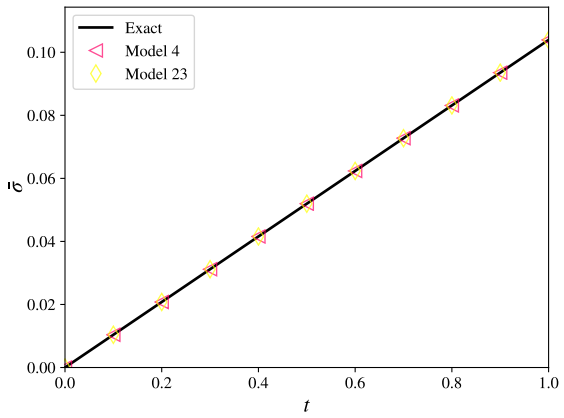

(a) Time-history plot of $\bar{\sigma}$ vs. t using $\Delta t = 0.1$.

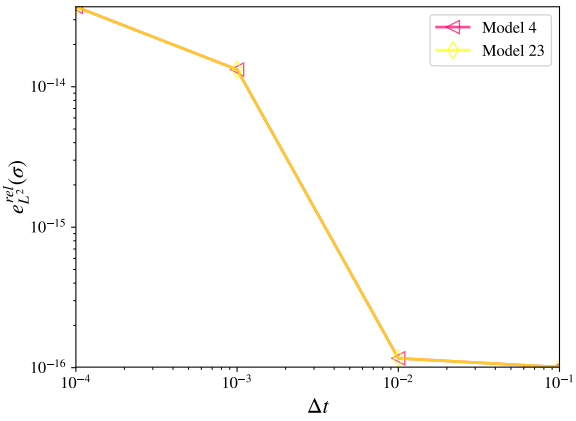

(b) Convergence plot for $e_{L^2}^{\text{rel}}(\boldsymbol{\sigma})$ errors vs. Δt.

Figure 7: Temperature-dependent isotropic elasticity test 4.

Table 11: Computed errors for temperature-dependent elasticity test 4.

Model	$e^{\text{rel}}_{L^2}(\boldsymbol{\sigma})$	r	$e^{\text{abs}}_{L^2}(\varepsilon_{33})$	r	$e^{\text{abs}}_{L^2}(\bar{\varepsilon}^p)$	r	Status
4	3.710e-14	-	0.000e+00	-	0.000e+00	-	✓
23	3.710e-14	-	0.000e+00	-	0.000e+00	-	✓

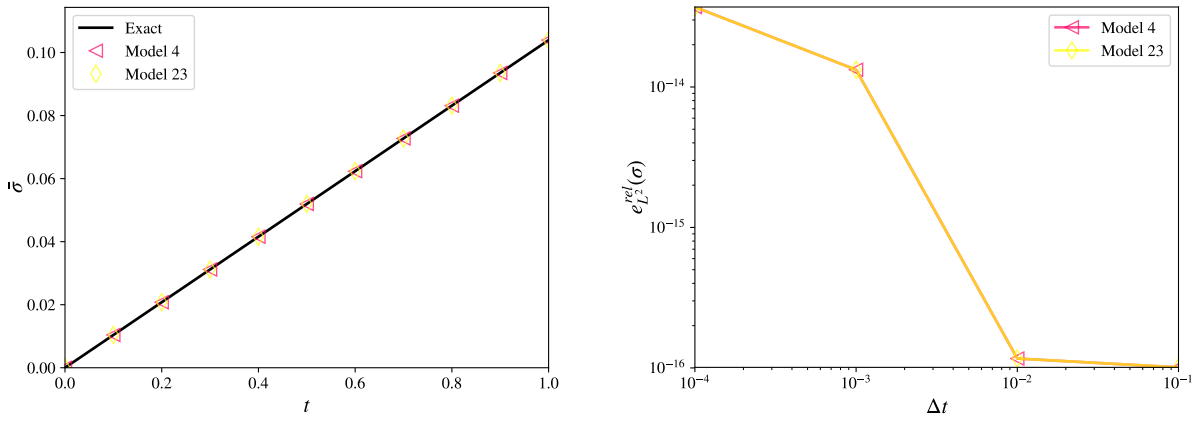

(a) Time-history plot of $\bar{\sigma}$ vs. t using $\Delta t = 0.1$.

(b) Convergence plot for $e^{\text{rel}}_{L^2}(\boldsymbol{\sigma})$ errors vs. Δt.

Figure 8: Temperature-dependent isotropic elasticity test 5.

Table 12: Computed errors for temperature-dependent elasticity test 5.

Model	$e^{\text{rel}}_{L^2}(\boldsymbol{\sigma})$	r	$e^{\text{abs}}_{L^2}(\varepsilon_{33})$	r	$e^{\text{abs}}_{L^2}(\bar{\varepsilon}^p)$	r	Status
4	3.710e-14	-	0.000e+00	-	0.000e+00	-	✓
23	3.710e-14	-	0.000e+00	-	0.000e+00	-	✓

4.2.2 Temperature-Dependent Thermal Expansion

Models 4, 23, and 71 possesses thermal expansion properties which may be independently varied with temperature. Despite their apparent similarities, however, all three models exhibit distinct behavior.

Namely, model 4 pre-computes the thermal strain at each of the tabulated input temperatures, and linearly interpolates these values with respect to temperature to determine intermediate values of thermal strain. The resulting behavior between two discretely specified temperatures is consequently linear. The peculiar behavior of model 4 is flagged as an inconsistent modeling approach which should be revisited and reevaluated at a later time.

Moreover, model 23 takes the tangent coefficients of thermal expansion as the user-specified tabulated input values, which for the present example are incidentally double the secant CTE values. In contrast, models 4 and 71 take the secant CTE as input.

The general thermal expansion solution derived in [3] is herein applied to the special case where $\bar{\alpha}(T)$ varies linearly with temperature. Assuming isotropic material behavior with load case 8 ($T_0 = 0.0$, $\bar{T} = 1.0$ such that $T(t) = \bar{T}t$), one obtains:

$$\varepsilon_{33}(t) = \frac{1+\nu}{1-\nu}\,\bar{\alpha}(T)\,T(t), \qquad \sigma_{11}(t) = \sigma_{22}(t) = -\frac{E}{1-\nu}\,\bar{\alpha}(T)\,T(t) \qquad \sigma_{12}(t) = \sigma_{23}(t) = \sigma_{13}(t) = 0. \tag{15}$$

The ensuing test utilizes the effective parameterization given by 13. The differing results obtained using model 4 are presented separately in table 14 and figure 9, while the coincident results for models 23 and 71 are provided together in table 15 and figure 10. For each model, the anticipated behavior (consistent with its description in the DYNA3D manual) is obtained.

Table 13: Material parameterization for the temperature-dependent isotropic thermal expansion test

Parameter	Value
Elastic modulus, E	7.5
Poisson's ratio, ν	0.25
Tabulated temperatures, T	{0.0, 1.0}
Tabulated secant coefficient of thermal expansion, $\bar{\alpha}$	{0.0, 0.1}

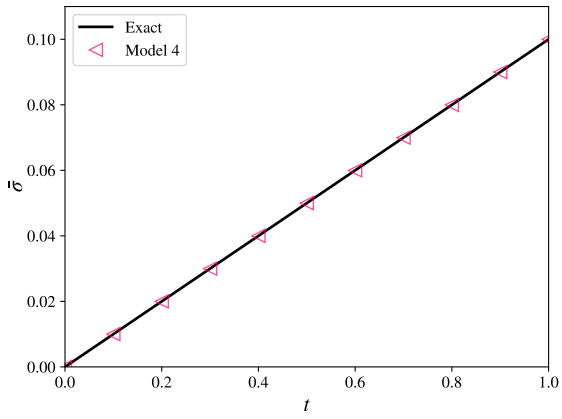

(a) Time-history plot of $\bar{\sigma}$ vs. t using $\Delta t = 0.1$.

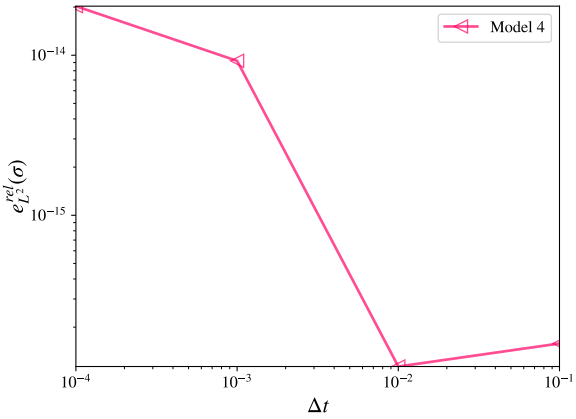

(b) Convergence plot for $e^{\text{rel}}_{L^2}(\boldsymbol{\sigma})$ errors vs. Δt.

Figure 9: Temperature-dependent isotropic thermal expansion test for model 4.

Table 14: Computed errors for the temperature-dependent isotropic thermal expansion test for model 4.

Model	$e^{\text{rel}}_{L^2}(\boldsymbol{\sigma})$	r	$e^{\text{rel}}_{L^2}(\varepsilon_{33})$	r	$e^{\text{abs}}_{L^2}(\bar{\varepsilon}^p)$	r	Status
4	2.026e-14	-	8.358e-14	-	0.000e+00	-	⚠

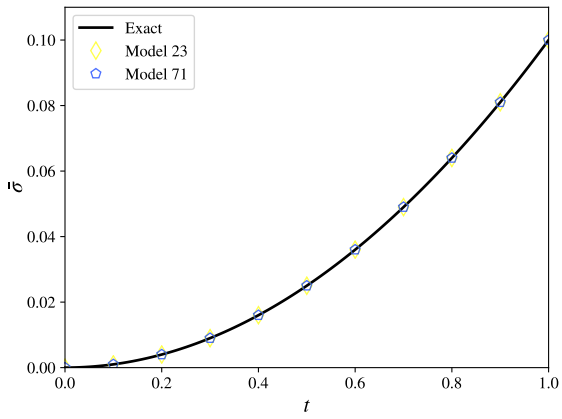

(a) Time-history plot of $\bar{\sigma}$ vs. t using $\Delta t = 0.1$.

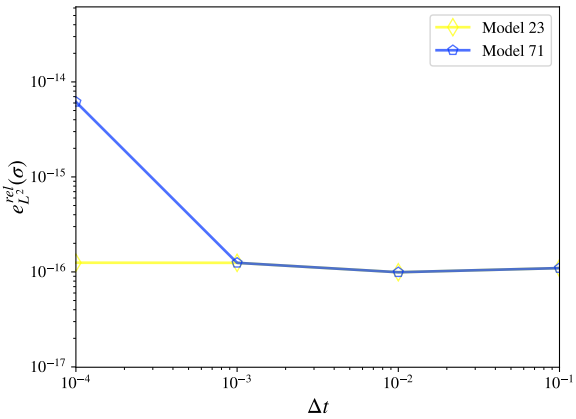

(b) Convergence plot for $e^{\text{rel}}_{L^2}(\boldsymbol{\sigma})$ errors vs. Δt.

Figure 10: Temperature-dependent isotropic thermal expansion test for models 23 and 71.

Table 15: Computed errors for the temperature-dependent isotropic thermal expansion test for models 23 and 71.

Model	$e^{\text{rel}}_{L^2}(\boldsymbol{\sigma})$	r	$e^{\text{rel}}_{L^2}(\varepsilon_{33})$	r	$e^{\text{abs}}_{L^2}(\bar{\varepsilon}^p)$	r	Status
23	1.250e-16	-	1.513e-14	-	0.000e+00	-	✓
71	6.163e-15	-	1.532e-14	-	0.000e+00	-	✓

4.2.3 Temperature-Dependent Linear Hardening Plasticity

Models 4, 15, and 71 possess various plasticity properties which depend upon temperature. Specifically, model 4 possesses linear isotropic hardening plasticity parameters (σ_y and E_p) which may be varied with temperature. Models 15 possesses a temperature-dependent yield stress which is re-scaled by the following thermal softening factor:

$$1 - (T^*)^m, \qquad T^* = \frac{T - T_r}{T_m - T_r}. \tag{16}$$

Model 71 possesses a more complicated temperature-dependent flow rule (not reproduced here). Nonetheless, all three models can be reduced to represent linear hardening plasticity with variable thermal properties.

Separate temperature-sensitive material parameterizations are specified for model 4 (table 16), model 15 (table 17), and model 71 (table 18). Notwithstanding these differences, the results of all three models coincide with the exact solution for the linear hardening plasticity test described in [3] when evaluated at a constant temperature of $T = 1$, as demonstrated in table 19 and figure 11. The correct behavior of all noted thermally varying properties for each model is consequently verified.

Table 16: Material parameterization 1 for the temperature-dependent linear hardening plasticity test for model 4

Parameter	Value
Elastic modulus, E	2.25
Poisson's ratio, ν	0.125
Tabulated temperatures, T	{0.0, 1.0}
Tabulated yield stresses, σ_0	{0.6, 0.3}
Tabulated tangent moduli, E_T	{3.6, 1.8}

Table 17: Material parameterization 2 for the temperature-dependent linear hardening plasticity test for model 15

Parameter	Value
Elastic modulus, E	2.25
Poisson's ratio, ν	0.125
Yield stress, σ_0	0.6
Tangent modulus, E_T	3.6
Thermal softening exponent, m	0.5
Room temperature, T_r	0.75
Melt temperature, T_m	1.75

Table 18: Material parameterization 3 for the temperature-dependent linear hardening plasticity test for model 71

Parameter	Value
Elastic modulus, E	2.25
Poisson's ratio, ν	0.125
Yield stress, σ_0	0.6
Tangent modulus, E_T	3.6
Temperature constants, $\{t_1, \ldots, t_5\}$	$\{0.5, -0.5, 0.5, 0.0, 0.0\}$

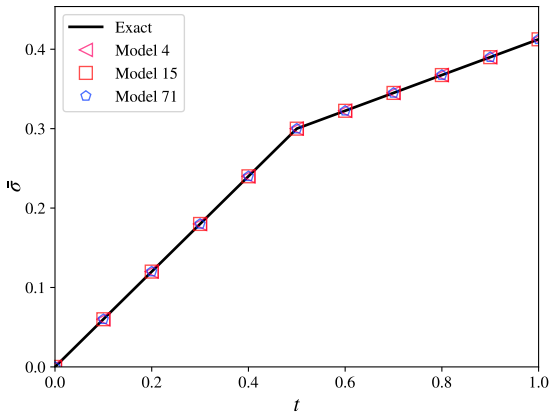

(a) Time-history plot of $\bar{\sigma}$ vs. t using $\Delta t = 0.1$.

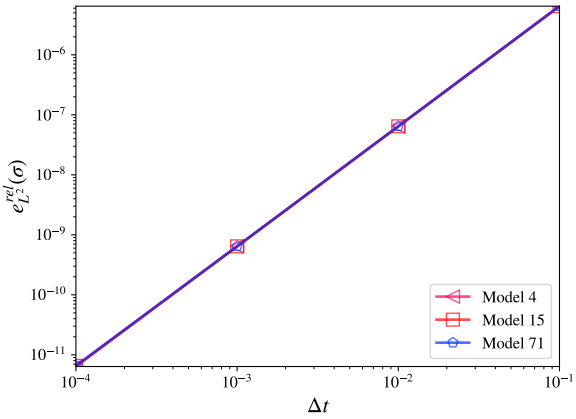

(b) Convergence plot for $e_{L^2}^{\text{rel}}(\boldsymbol{\sigma})$ errors vs. Δt.

Figure 11: Temperature-dependent linear hardening plasticity test.

Table 19: Computed errors for the temperature-dependent linear hardening plasticity test.

Model	$e_{L^2}^{\text{rel}}(\boldsymbol{\sigma})$	r	$e_{L^2}^{\text{abs}}(\varepsilon_{33})$	r	$e_{L^2}^{\text{rel}}(\bar{\varepsilon}^p)$	r	Status
4	6.383e-12	2.00	1.264e-14	1.70	1.126e-11	1.98	✓
15	6.547e-12	1.99	1.808e-15	2.00	1.160e-11	1.98	✓
71	6.559e-12	1.99	1.835e-15	2.00	1.163e-11	1.98	✓

4.2.4 Model 54 Temperature-Dependent Hardening Plasticity

Model 54 possesses a complicated temperature-dependent yield stress which can be reduced to represent variable hardening behavior, including power-law plasticity with a temperature-dependent hardening modulus as a parcular special case.

Two tests are proposed to verify the temperature-dependent behavior of model 54, both of which utilize load case 6 ($\bar{\gamma} = 0.1$). The first test results in a perfectly plastic response with a constant yield stress of $\sigma_y = C_0 + C_1 e^{-TC_2}$. The material parameterization for this test is given in table 20, with the results provided in table 21 and figure 12 confirmed the expected behavior.

The second test results in a power-law hardening response with a time-varying yield stress of $\sigma_y = C_0 + C_4\sqrt{\bar{\varepsilon}^p}e^{-TC_5}$, and the following exact solution for the equivalent plastic strain:

$$\bar{\varepsilon}^p(t) = \frac{-2\sqrt{(3\mu k)^2\dot{\bar{\varepsilon}}(t-t_0)+k^4} - (3\mu)^2\dot{\bar{\varepsilon}}(t-t_0) + 2k^2}{(3\mu)^2} \quad \forall t > t_0, \qquad k \equiv \frac{1}{2}C_4 e^{-TC_5}. \tag{17}$$

The material parameterization for this test is given in table 22, with the results provided in table 23 and figure 13 confirming the expected behavior.

Table 20: Material parameterization for model 54 temperature-dependent hardening plasticity test 1

Parameter	Value
Elastic modulus, E	2.25
Poisson's ratio, ν	0.125
Strength coefficient, C_0	0.3
Strength coefficient, C_1	0.1
Strength coefficient, C_2	1.0
Reference temperature, T_r	1.0

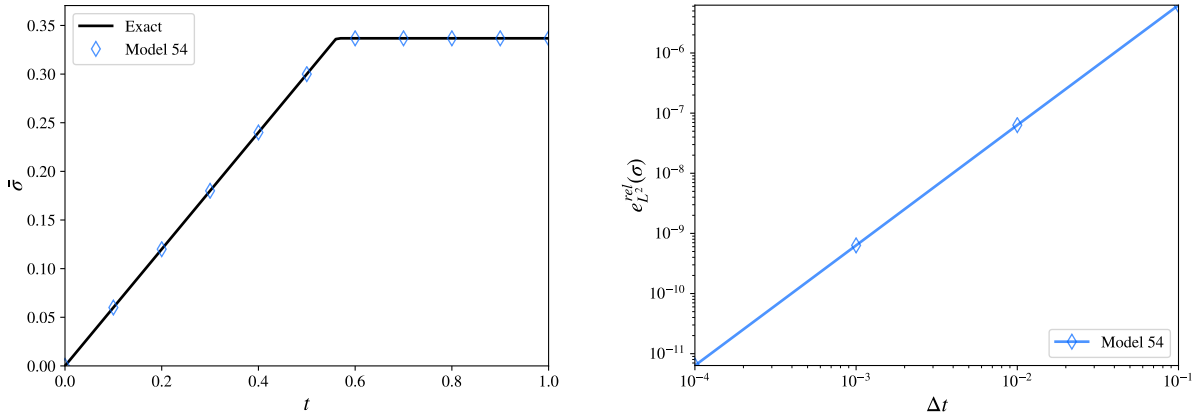

(a) Time-history plot of $\bar{\sigma}$ vs. t using $\Delta t = 0.1$.

(b) Convergence plot for $e_{L^2}^{\text{rel}}(\boldsymbol{\sigma})$ errors vs. Δt.

Figure 12: Model 54 temperature-dependent hardening plasticity test 1.

Table 21: Computed errors for model 54 temperature-dependent hardening plasticity test 1.

Model	$e_{L^2}^{\text{rel}}(\boldsymbol{\sigma})$	r	$e_{L^2}^{\text{abs}}(\varepsilon_{33})$	r	$e_{L^2}^{\text{rel}}(\bar{\varepsilon}^p)$	r	Status
54	6.352e-12	1.99	2.603e-15	2.00	1.351e-11	1.99	✓

Table 22: Material parameterization for model 54 temperature-dependent hardening plasticity test 2

Parameter	Value
Elastic modulus, E	2.25
Poisson's ratio, ν	0.125
Strength coefficient, C_0	0.3
Strength coefficient, C_4	1.0
Strength coefficient, C_5	1.0
Reference temperature, T_r	1.0

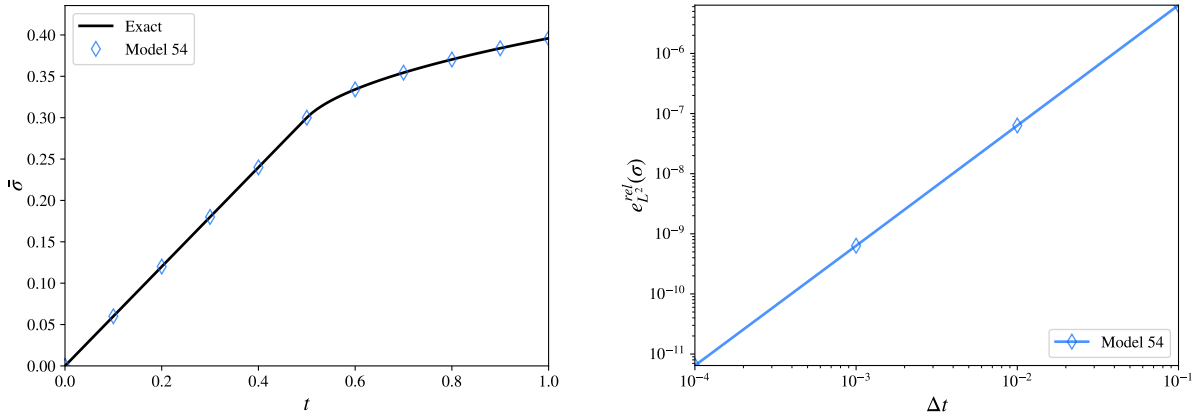

(a) Time-history plot of $\bar{\sigma}$ vs. t using $\Delta t = 0.1$.

(b) Convergence plot for $e_{L^2}^{\text{rel}}(\boldsymbol{\sigma})$ errors vs. Δt.

Figure 13: Model 54 temperature-dependent hardening plasticity test 2.

Table 23: Computed errors for model 54 temperature-dependent hardening plasticity test 2.

Model	$e_{L^2}^{\text{rel}}(\boldsymbol{\sigma})$	r	$e_{L^2}^{\text{abs}}(\varepsilon_{33})$	r	$e_{L^2}^{\text{rel}}(\bar{\varepsilon}^p)$	r	Status
54	6.445e-12	1.99	1.771e-15	2.00	1.375e-11	1.97	✓

4.2.5 Model 71 Temperature-Dependent Hardening Plasticity

Model 71 possesses a complicated set of material coefficients which can be reduced to represent perfect plasticity with a temperature-dependent yield stress. The chosen parameterization given in table 24 results in a perfectly plastic response with a constant yield stress of $\sigma_y = \sigma_0(t_3 e^{t_4/(T+t_5)})$. The ensuing test utilizes load case 6 ($\bar{\gamma} = 0.1$), with the results presented in table 25 and figure 14, confirming the expected behavior.

Table 24: Material parameterization for the model 71 temperature-dependent hardening plasticity test

Parameter	Value
Elastic modulus, E	2.25
Poisson's ratio, ν	0.125
Isothermal yield stress, σ_0	0.3
Temperature coefficient, t_3	1.0
Temperature coefficient, t_4	2.0
Temperature coefficient, t_5	3.0
Reference temperature, T_{ref}	1.0

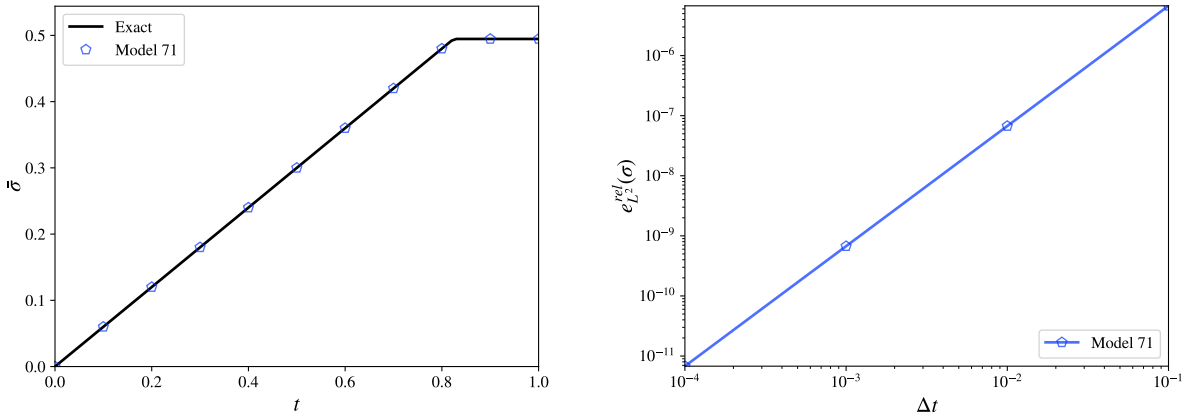

(a) Time-history plot of $\bar{\sigma}$ vs. t using $\Delta t = 0.1$.

(b) Convergence plot for $e^{\text{rel}}_{L^2}(\boldsymbol{\sigma})$ errors vs. Δt.

Figure 14: Model 71 temperature-dependent hardening plasticity test.

Table 25: Computed errors for the model 71 temperature-dependent hardening plasticity test.

Model	$e^{\text{rel}}_{L^2}(\boldsymbol{\sigma})$	r	$e^{\text{abs}}_{L^2}(\varepsilon_{33})$	r	$e^{\text{rel}}_{L^2}(\bar{\varepsilon}^p)$	r	Status
71	6.778e-12	2.00	2.564e-15	2.00	3.903e-11	1.94	✓

4.2.6 Heat Generation and Thermal Softening

Models 15, 38, 39, 52, 54, and 71 incorporate adiabatic heat generation due to plastic work. Specifically, the localized temperature T in the material evolves according to

$$T = T_0 + \frac{\phi\omega}{\rho C_v}, \tag{18}$$

where T_0 is the initial/ambient temperture, ρ is the material density, C_v is the effective specific heat, and ϕ is the fraction of plastic work converted to heat.

For models 38, 39, 52, 54, and 71, $\omega = \omega^p$ represents the total plastic work computed via

$$\omega^p = \int_0^t \bar{\sigma}\dot{\bar{\varepsilon}}^p \, \mathrm{d}t. \tag{19}$$

For model 15, $\omega = \omega^m$ instead corresponds to the total mechanical work, computed via

$$\omega^m = \int_0^t \boldsymbol{\sigma} : \dot{\boldsymbol{\varepsilon}} \, \mathrm{d}t. \tag{20}$$

This discrepancy implies that the temperature in model 15 may decrease during mechanical unloading processes, resulting in an apparent thermodynamic inconsistency which warrants re-evaluation. Nonetheless, this is consistent with what is described in the DYNA3D manual, and is therefore taken as the intended behavior of the present model implementation.

Under proportional loading conditions with a constant rate of loading (e.g. load case 6), the effective stress $\bar{\sigma}$ may be expressed as

$$\bar{\sigma}(t) = 3\mu(\dot{\bar{\varepsilon}}t - \bar{\varepsilon}^p), \tag{21}$$

such that the time-rate of the plastic work is expressible in terms of the equivalent plastic strain and its rate:

$$\dot{\omega}^p = 3\mu(\dot{\bar{\varepsilon}}t - \bar{\varepsilon}^p)\dot{\bar{\varepsilon}}^p, \tag{22}$$

whereas the time-rate of the mechanical work is expressible as:

$$\dot{\omega}^m = 3\mu(\dot{\bar{\varepsilon}}t - \bar{\varepsilon}^p)\dot{\bar{\varepsilon}}. \tag{23}$$

For models 15, 52, and 71, select material parameterizations allow for the yield stress to be expressed in terms of a linear softening model with respect to temperature, i.e.

$$\sigma_y(T) = \sigma_0 - k_T T, \tag{24}$$

such that the plastic consistency condition $f_y = \dot{\bar{\sigma}} - \dot{\sigma}_y = 0$ constitutes a differential equation in terms of the equivalent plastic strain and its rate, for models 52 and 71:

$$3\mu(\dot{\bar{\varepsilon}} - \dot{\bar{\varepsilon}}^p) + k_T\frac{\phi}{\rho C_v}3\mu(\dot{\bar{\varepsilon}}t - \bar{\varepsilon}^p)\dot{\bar{\varepsilon}}^p = 0, \qquad \bar{\varepsilon}^p(t_0) = 0, \tag{25}$$

where $t_0 = \frac{\sigma_0}{3\mu\dot{\bar{\varepsilon}}}$ denotes the time of initial yielding. An exact solution to the above is obtained for model 52 and 71 as

$$\bar{\varepsilon}^p(t) = \dot{\bar{\varepsilon}}t + \frac{\rho C_v}{\phi k_T} W\left(-\frac{\phi k_T}{\rho C_v}\frac{\sigma_0}{3\mu}e^{-\frac{\phi k_T}{\rho C_v}\dot{\bar{\varepsilon}}t}\right) \quad \forall t > t_0, \tag{26}$$

where $W(\cdot)$ is the Lambert W function.

For model 15, the plastic consistency condition is expressed as:

$$3\mu(\dot{\bar{\varepsilon}} - \dot{\bar{\varepsilon}}^p) + k_T\frac{\phi}{\rho C_v}3\mu(\dot{\bar{\varepsilon}}t - \bar{\varepsilon}^p)\dot{\bar{\varepsilon}} = 0, \qquad \bar{\varepsilon}^p(t_0) = 0, \tag{27}$$

where t_0 must satisfy

$$t_0 = \frac{\sigma_0\left[1 - \frac{\phi\omega^m(t_0)}{\rho C_v}\right]}{3\mu\dot{\bar{\varepsilon}}}, \qquad \omega^m(t_0) = \int_0^{t_0} 3\mu\dot{\bar{\varepsilon}}^2 t \, \mathrm{d}t = \frac{3}{2}\mu(\dot{\bar{\varepsilon}}t_0)^2, \tag{28}$$

such that

$$t_0 = \frac{\sqrt{9 + 6\frac{\phi}{\rho C_v}\frac{\sigma_0^2}{\mu}} - 3}{3\frac{\phi}{\rho C_v}\sigma_0\dot{\bar{\varepsilon}}}. \tag{29}$$

An exact solution to the above is obtained for model 15 as

$$\bar{\varepsilon}^p(t) = \dot{\bar{\varepsilon}}\left(t - t_0 e^{-\frac{\phi k_T}{\rho C_v}\dot{\bar{\varepsilon}}(t-t_0)}\right) \quad \forall t > t_0. \tag{30}$$

The heat generation tests for models 15, 52, and 71 utilize load case 6 ($\bar{\gamma} = 0.1$) and the material parameterization given in table 26. Separate exact solutions are used to verify the implementations of model 15 vs. models 52 and 71, as discussed above. The results are presented respectively in tables 27, 28 and figures 15, 16.

Table 26: Material parameterization for the heat generation tests for models 15, 52, and 71.

Parameter	Value
Elastic modulus, E	2.4
Poisson's ratio, ν	0.2
Yield stress, σ_0	0.3
Thermal softening modulus, k_T	0.3
Mass density, ρ	1.0
Fraction of plastic work converted to heat, ϕ	0.5
Effective specific heat, C_v	0.025

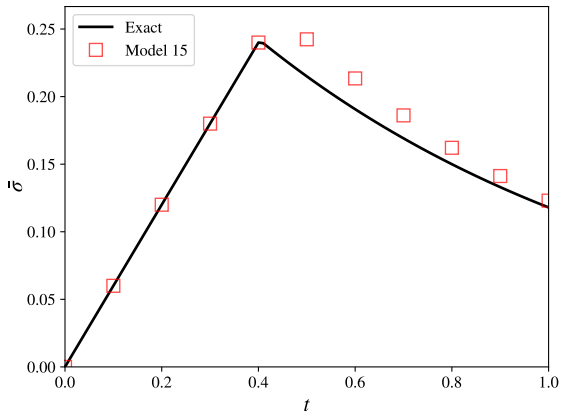

(a) Time-history plot of $\bar{\sigma}$ vs. t using $\Delta t = 0.1$.

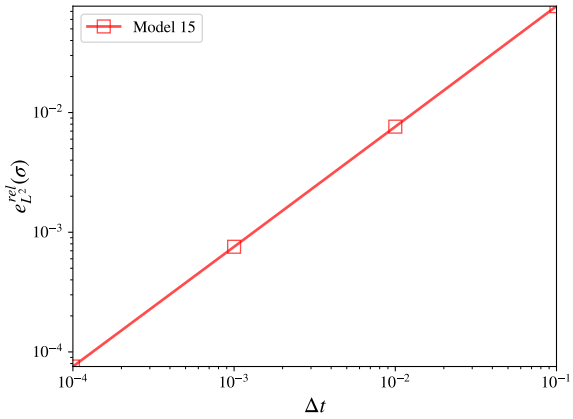

(b) Convergence plot for $e^{\text{rel}}_{L^2}(\boldsymbol{\sigma})$ errors vs. Δt.

Figure 15: Heat generation test for model 15.

Table 27: Computed errors for heat generation test 1 for model 15.

Model	$e^{\text{rel}}_{L^2}(\boldsymbol{\sigma})$	r	$e^{\text{abs}}_{L^2}(\varepsilon_{33})$	r	$e^{\text{rel}}_{L^2}(\bar{\varepsilon}^p)$	r	Status
15	7.552e-05	1.00	6.907e-15	2.00	5.576e-05	1.00	✓

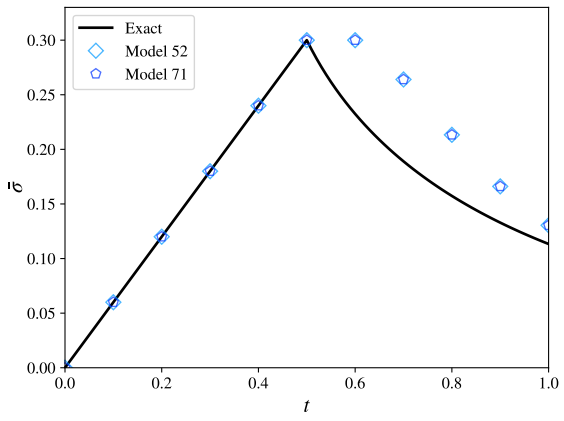

(a) Time-history plot of $\bar{\sigma}$ vs. t using $\Delta t = 0.1$.

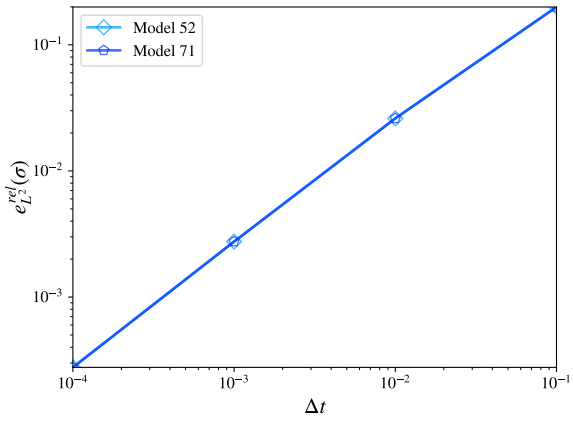

(b) Convergence plot for $e^{\text{rel}}_{L^2}(\boldsymbol{\sigma})$ errors vs. Δt.

Figure 16: Heat generation test for models 52 and 71.

Table 28: Computed errors for heat generation test 1 for models 52 and 71.

Model	$e^{\text{rel}}_{L^2}(\boldsymbol{\sigma})$	r	$e^{\text{abs}}_{L^2}(\varepsilon_{33})$	r	$e^{\text{rel}}_{L^2}(\bar{\varepsilon}^p)$	r	Status
52	2.770e-04	0.88	1.336e-14	1.90	2.366e-04	0.88	✓
71	2.770e-04	0.88	8.211e-15	1.99	2.366e-04	0.88	✓

For models 38 and 39, the yield stress can be expressed in terms of an inverse exponential softening model with respect to temperature, i.e.

$$\sigma_y(T) = C_3 + C_1 e^{-\frac{C_2}{T}} \sinh^{-1}\left[\frac{\dot{\bar{\varepsilon}}}{C_5}\right], \tag{31}$$

and adiabatic heating is driven by an equivalent "heat generation coefficient" $HC = \frac{\phi}{\rho C_v}$, which is defined directly as an input parameter.

Although the above does not admit an exact solution for arbitrary parameterizations of the noted coefficients, it suffices to examine the behavior of σ_y in the limit as $T \to +\infty$, i.e.

$$\lim_{T\to+\infty} \sigma_y(T) = C_3 + C_1 \sinh^{-1}\left[\frac{\dot{\bar{\varepsilon}}}{C_5}\right], \tag{32}$$

thus approaching perfectly plastic behavior with a constant yield stress for sufficiently large values of T. Equivalently, the above asymptoptic condition can be obtained by considering $HC \to +\infty$, thereby yielding a rapid increase in temperature soon after the initiation of plastic loading. As such, the exact solution for sufficiently large values of HC should produce perfectly plastic behavior with the constant yield stress given in equation (32), and any arbitrary choice of the remaining parameters (C_1, C_2, C_3, C_5).

The heat generation test for models 38 and 39 utilizes load case 6 ($\bar{\gamma} = 0.1$) and the material parameterization given in table 29. The results are presented in table 30 and figure 17.

Table 29: Material parameterization for the heat generation test for models 38 and 39.

Parameter	Value
Elastic modulus, E	2.4
Poisson's ratio, ν	0.2
C_1	0.15
C_2	1.0
C_3	0.15
C_5	0.2
Initial temperature, T_0	1.0e-14
Heat generation coefficient, HC	1.0e+12

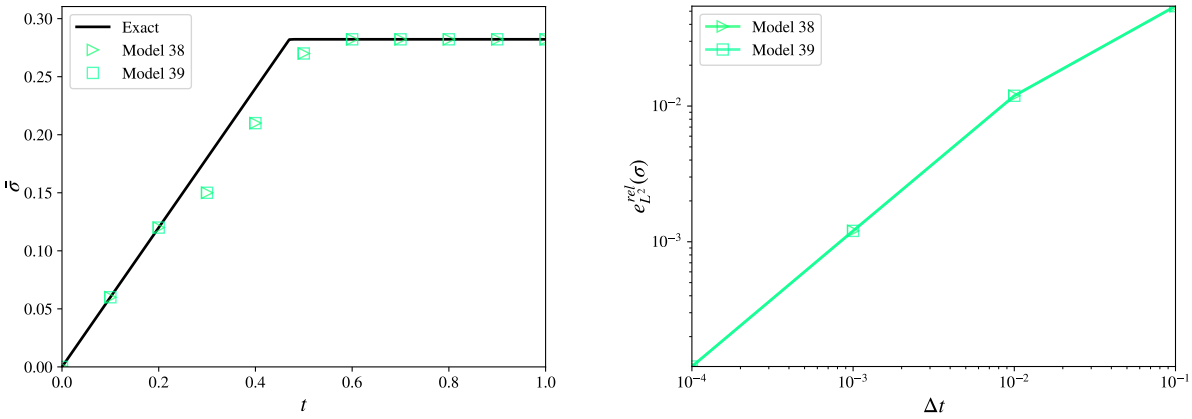

(a) Time-history plot of $\bar{\sigma}$ vs. t using $\Delta t = 0.1$.

(b) Convergence plot for $e_{L^2}^{\text{rel}}(\boldsymbol{\sigma})$ errors vs. Δt.

Figure 17: Heat generation test for models 38 and 39.

Table 30: Computed errors for the heat generation test for model 38 and 39.

Model	$e_{L^2}^{\text{rel}}(\boldsymbol{\sigma})$	r	$e_{L^2}^{\text{abs}}(\varepsilon_{33})$	r	$e_{L^2}^{\text{rel}}(\bar{\varepsilon}^p)$	r	Status
38	1.204e-04	0.66	1.074e-14	1.85	2.109e-04	0.66	✓
39	1.204e-04	0.66	1.078e-14	1.85	2.109e-04	0.66	✓

For model 54, a reduced parameterization allows for the yield stress to be expressed in terms of an exponential softening model with respect to temperature, i.e.

$$\sigma_y(T) = \sigma_0 e^{-k_T T}, \tag{33}$$

such that

$$3\mu(\dot{\bar{\varepsilon}} - \dot{\bar{\varepsilon}}^p) - k_T \sigma_0 e^{-k_T T} \frac{\phi}{\rho C_v} 3\mu(\dot{\bar{\varepsilon}} t - \bar{\varepsilon}^p)\dot{\bar{\varepsilon}}^p = 0, \qquad \bar{\varepsilon}^p(t_0) = 0. \tag{34}$$

An exact solution for the evolving temperature as a function of time is given by

$$T(t) = \frac{1}{k_T} \log\left(\frac{\sqrt{f(t)^2 - 12\mu \frac{\phi k_T}{\rho C_v}\sigma_0^2} + f(t)}{6\mu} \right) \quad \forall t > t_0, \tag{35}$$

$$f(t) = 3\mu \frac{\phi k_T}{\rho C_v} \sigma_0 \dot{\bar{\varepsilon}}(t - t_0) + \frac{\phi k_T}{\rho C_v}\sigma_0^2 + 3\mu, \qquad t_0 = \frac{\sigma_0}{3\mu\dot{\bar{\varepsilon}}}, \tag{36}$$

such that the equivalent plastic strain may be expressed as a function of time:

$$\bar{\varepsilon}^p(t) = \dot{\bar{\varepsilon}} t - \frac{\sigma_0}{3\mu} e^{-k_T T(t)} \quad \forall t > t_0. \tag{37}$$

The ensuing heat generation test for model 54 utilizes load case 6 ($\bar{\gamma} = 0.1$) and the material parameterization given in table 31. The results are presented in table 32 and figure 18.

Table 31: Material parameterization for the model 54 heat generation test.

Parameter	Value
Elastic modulus, E	2.4
Poisson's ratio, ν	0.2
Yield stress, σ_0	0.3
Thermal softening modulus, k_T	0.3
Mass density, ρ	1.0
Fraction of plastic work converted to heat, ϕ	0.5
Effective specific heat, C_v	0.025

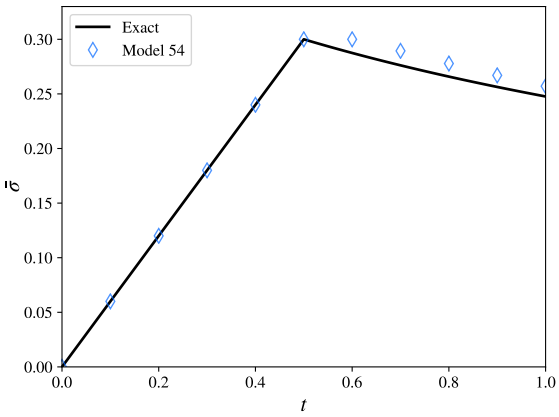

(a) Time-history plot of $\bar{\sigma}$ vs. t using $\Delta t = 0.1$.

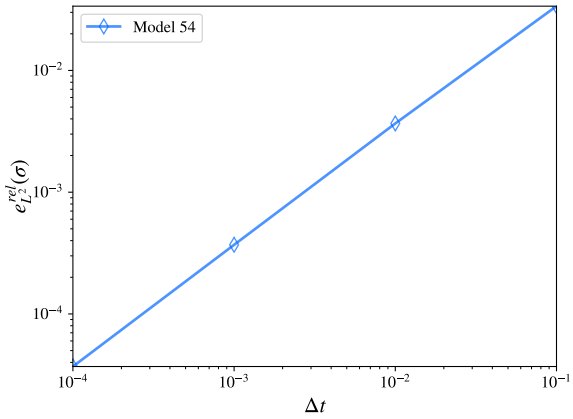

(b) Convergence plot for $e_{L^2}^{\text{rel}}(\boldsymbol{\sigma})$ errors vs. Δt.

Figure 18: Heat generation test for model 54.

Table 32: Computed errors for the heat generation test for model 54.

Model	$e_{L^2}^{\text{rel}}(\boldsymbol{\sigma})$	r	$e_{L^2}^{\text{abs}}(\varepsilon_{33})$	r	$e_{L^2}^{\text{rel}}(\bar{\varepsilon}^p)$	r	Status
54	3.700e-05	0.96	5.308e-15	2.00	5.822e-05	0.96	✓

4.3 Rate-Dependent Plasticity

Models 15, 19, 24, 35, 38, 39, 52, and 54 possess rate-dependent material properties, most of which pertain to variable behavior under different rates of plastic loading. The following sub-sections provide coverage for these features through a series of model-specific tests.

4.3.1 Strain Rate-Dependent Hardening Plasticity

Collectively, the following models possess a number of similar (total) strain rate-dependent material properties:

- Model 19 possesses a strain-rate dependent yield stress and tangent modulus (linear hardening)
- Model 35 possesses a yield stress which may be optionally re-scaled (according to a user-defined load curve) by a factor which depends upon the total effective strain rate. If the rate-independent portion of the model is consistent with linear hardening plasticity, then the rate-dependent behavior of the model can be verified using the linear hardening plasticity test(s).
- Model 52 possesses a yield stress which may optionally vary with respect to the total effective strain rate.

The strain-rate dependent plasticity test utilizes load case 1 ($\bar{\gamma} = 0.3$) and the effective material parameterization given in table 33 at a fixed total strain rate, albeit with variable strain rate-dependent properties for each model. As such, all rate-sensitive properties for models 19, 35, and 52 are covered by virtue of the proposed test, with all models yielding identical behavior, as verified by the quantitative results presented in table 34 and figure 19.

Table 33: Material parameterization for the strain rate-dependent hardening plasticity test

Parameter	Value
Elastic modulus, E	1.8
Poisson's ratio, ν	0.0
Yield stress, σ_0	0.3
Tangent modulus, E_T	1.2

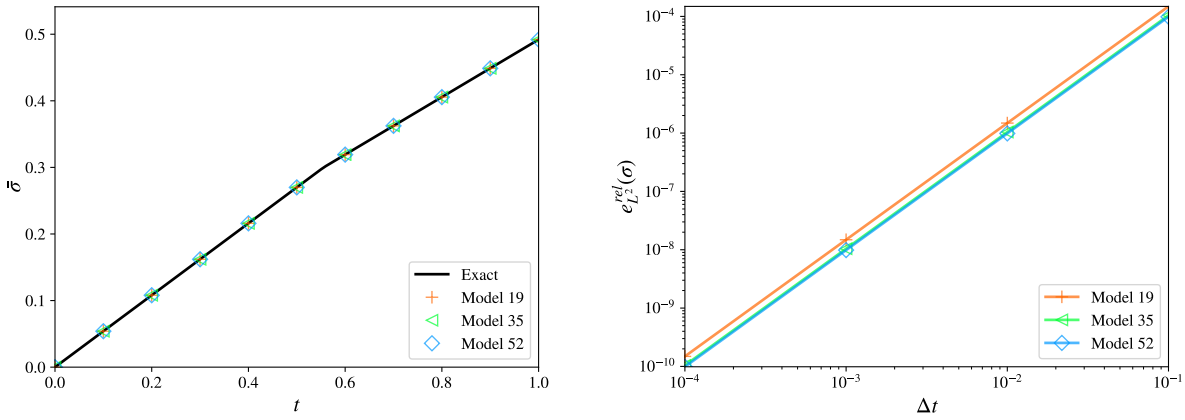

(a) Time-history plot of $\bar{\sigma}$ vs. t using $\Delta t = 0.1$.

(b) Convergence plot for $e_{L^2}^{\text{rel}}(\boldsymbol{\sigma})$ errors vs. Δt.

Figure 19: Strain rate-dependent hardening plasticity test.

Table 34: Computed errors for the strain rate-dependent hardening plasticity test.

Model	$e_{L^2}^{\text{rel}}(\boldsymbol{\sigma})$	r	$e_{L^2}^{\text{rel}}(\varepsilon_{33})$	r	$e_{L^2}^{\text{rel}}(\bar{\varepsilon}^p)$	r	Status
19	1.486e-10	2.00	1.329e-10	2.00	3.332e-10	2.00	✓
35	1.042e-10	2.00	2.098e-10	1.93	1.803e-10	1.99	✓
52	9.863e-11	2.00	2.819e-10	2.00	2.819e-10	2.00	✓

4.3.2 Model 15 Strain-Rate Dependent Plasticity

In the absence of work-hardening or temperature-softening effects, model 15 possesses a strain-rate dependent yield stress of the following form (more thoroughly described in the DYNA3D manual [5]):

$$\sigma_y = A\left(1 + C\log(\max\{\dot{\varepsilon}^*, 0.002\}) + D\log(\max\{\dot{\varepsilon}^*, 1\})^{n_2}\right), \qquad \dot{\varepsilon}^* = \frac{\dot{\bar{\varepsilon}}}{\dot{\varepsilon}_0}. \tag{38}$$

To provide test coverage for all of the relevant rate-dependent plasticity parameters appearing in equation (38), a series of tests are proposed which utilize load case 6 ($\bar{\gamma} = 0.1$), the generic material parameterization given in table 35, and the test-specific parameterizations enumerated in table 36. The quantitative results of these rate-dependent plasticity tests 1-4 for model 15 are provided in tables 37-40 and figures 20-23, confirming the expected behavior of all tested features.

Table 35: Material parameterization for the model 15 strain rate-dependent plasticity tests

Parameter	Value
Elastic modulus, E	2.25
Poisson's ratio, ν	0.125
Yield stress, A	0.1
Hardening modulus, B	0.0

Table 36: Model 15 strain rate-dependent plasticity tests

Test	C	D	n_2	$\dot{\varepsilon}_0$	t_0
1	0.1	0	0	5.0e-10	≈ 0.496783
2	0	2.0	0	0.1	0.5
3	0	2.4	0.5	0.1	≈ 0.499689
4	0	1.0	1.0	0.027	≈ 0.500413

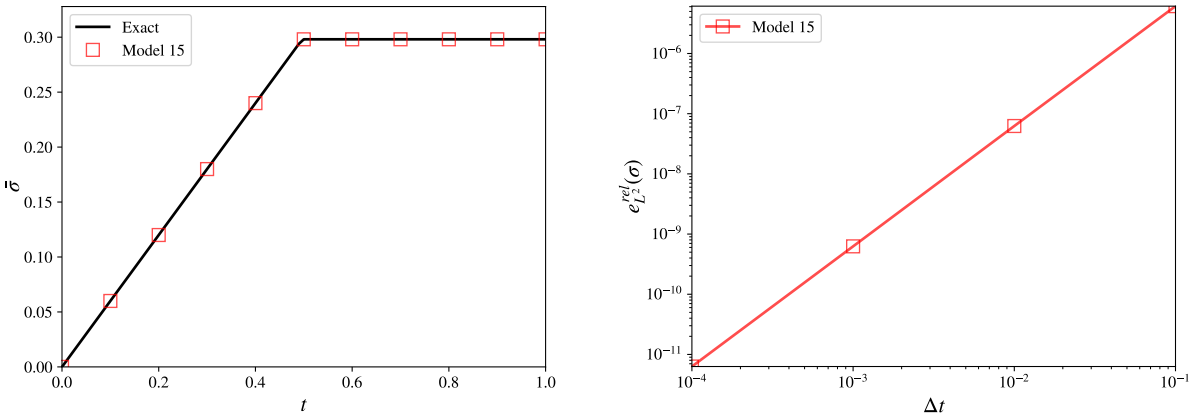

(a) Time-history plot of $\bar{\sigma}$ vs. t using $\Delta t = 0.1$.

(b) Convergence plot for $e_{L^2}^{\text{rel}}(\boldsymbol{\sigma})$ errors vs. Δt.

Figure 20: Model 15 strain rate-dependent plasticity test 1.

Table 37: Computed errors for model 15 rate-dependent plasticity test 1.

Model	$e_{L^2}^{\text{rel}}(\boldsymbol{\sigma})$	r	$e_{L^2}^{\text{abs}}(\varepsilon_{33})$	r	$e_{L^2}^{\text{rel}}(\bar{\varepsilon}^p)$	r	Status
15	6.299e-12	1.99	2.418e-15	2.00	1.078e-11	1.99	✓

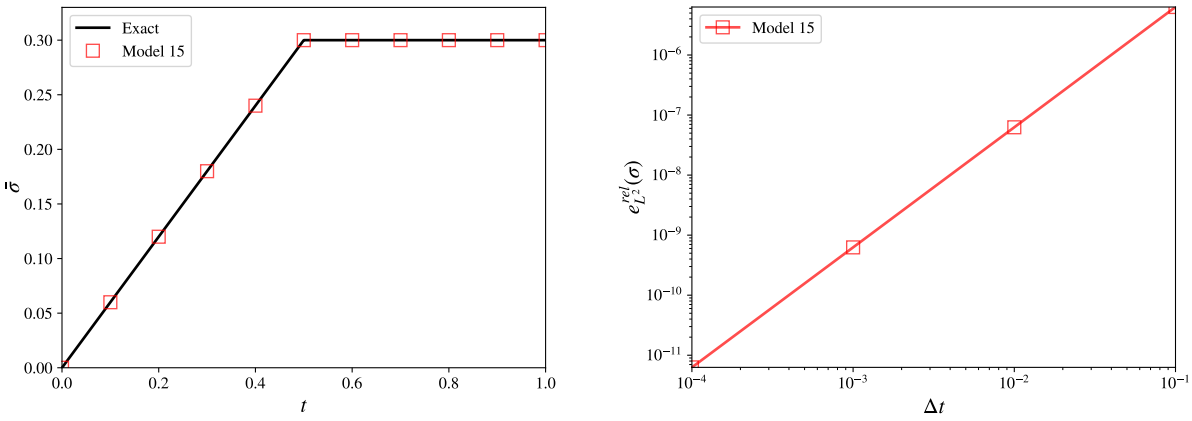

(a) Time-history plot of $\bar{\sigma}$ vs. t using $\Delta t = 0.1$.

(b) Convergence plot for $e_{L^2}^{\text{rel}}(\boldsymbol{\sigma})$ errors vs. Δt.

Figure 21: Model 15 strain rate-dependent plasticity test 2.

Table 38: Computed errors for model 15 rate-dependent plasticity test 2.

Model	$e_{L^2}^{\text{rel}}(\boldsymbol{\sigma})$	r	$e_{L^2}^{\text{abs}}(\varepsilon_{33})$	r	$e_{L^2}^{\text{rel}}(\bar{\varepsilon}^p)$	r	Status
15	6.278e-12	2.00	2.294e-15	2.00	1.163e-11	1.98	✓

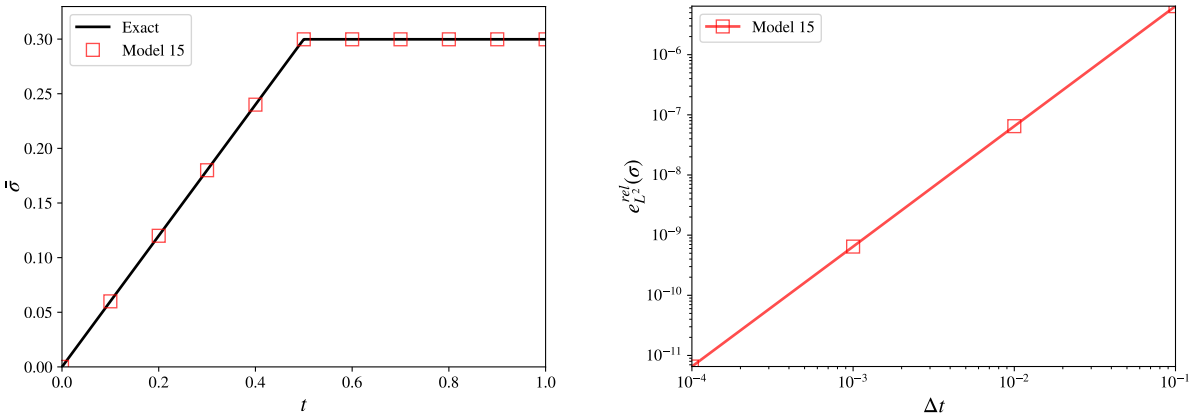

(a) Time-history plot of $\bar{\sigma}$ vs. t using $\Delta t = 0.1$.

(b) Convergence plot for $e_{L^2}^{\text{rel}}(\boldsymbol{\sigma})$ errors vs. Δt.

Figure 22: Model 15 strain rate-dependent plasticity test 3.

Table 39: Computed errors for model 15 rate-dependent plasticity test 3.

Model	$e_{L^2}^{\text{rel}}(\boldsymbol{\sigma})$	r	$e_{L^2}^{\text{abs}}(\varepsilon_{33})$	r	$e_{L^2}^{\text{rel}}(\bar{\varepsilon}^p)$	r	Status
15	6.550e-12	1.99	2.534e-15	2.00	8.116e-12	1.99	✓

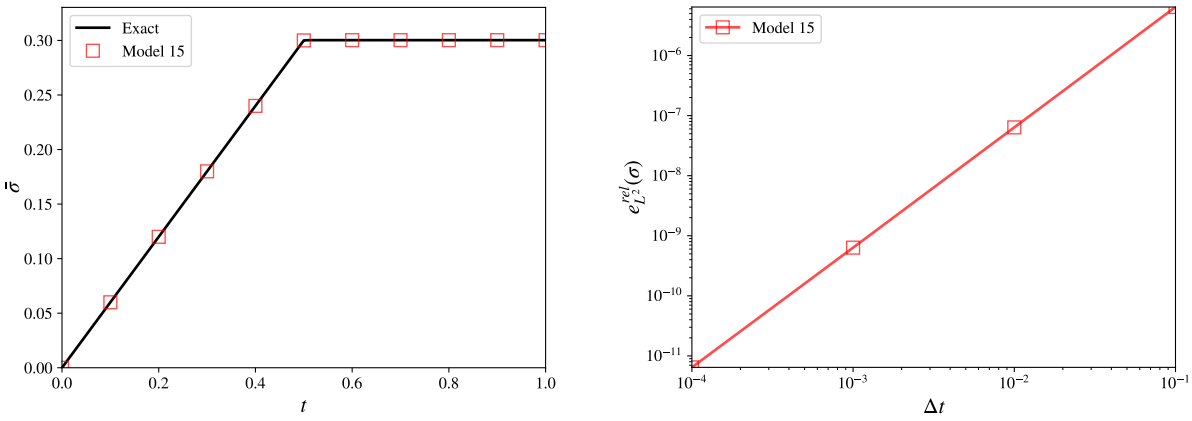

(a) Time-history plot of $\bar{\sigma}$ vs. t using $\Delta t = 0.1$.

(b) Convergence plot for $e_{L^2}^{\text{rel}}(\boldsymbol{\sigma})$ errors vs. Δt.

Figure 23: Model 15 strain rate-dependent plasticity test 4.

Table 40: Computed errors for model 15 rate-dependent plasticity test 4.

Model	$e_{L^2}^{\text{rel}}(\boldsymbol{\sigma})$	r	$e_{L^2}^{\text{abs}}(\varepsilon_{33})$	r	$e_{L^2}^{\text{rel}}(\bar{\varepsilon}^p)$	r	Status
15	6.446e-12	1.99	2.404e-15	2.00	9.456e-12	1.98	✓

4.3.3 Model 54 Strain-Rate Dependent Plasticity

Model 54 possesses a threshhold plastic strain rate which is used to cap the plastic strain rate-dependence of the yield surface.

The yield stress reccommended for use in representing FCC metals is expressed as:

$$\sigma_y = C_0 + C_4\sqrt{\bar{\varepsilon}^p}e^{-T(C_5 - C_6\log(\max\left\{\dot{\bar{\varepsilon}}^p, \dot{\bar{\varepsilon}}^p_{thres}\right\}))}, \tag{39}$$

where $\dot{\bar{\varepsilon}}^p_{thres}$ indicates the threshold (minimum) plastic strain rate. Under isothermal conditions with $T = 1.0$ and $C_5 = 0$:

$$\sigma_y = C_0 + C_4 \max\left\{\dot{\bar{\varepsilon}}^p, \dot{\bar{\varepsilon}}^p_{thres}\right\})^{C_6}\sqrt{\bar{\varepsilon}^p}, \tag{40}$$

which for sufficiently large values of $\dot{\bar{\varepsilon}}^p_{thres}$ (sufficiently low plastic strain rates) reduces further to

$$\sigma_y = C_0 + C_4(\dot{\bar{\varepsilon}}^p_{thres})^{C_6}\sqrt{\bar{\varepsilon}^p} \quad \forall \dot{\bar{\varepsilon}}^p \leq \dot{\bar{\varepsilon}}^p_{thres}, \tag{41}$$

thereby reproducing the behavior of a power-law hardening material with initial yield stress $\sigma_0 = C_0$ and power-law hardening modulus $E_p = C_4(\dot{\bar{\varepsilon}}^p_{thres})^{C_6}$.

The model 54 rate-dependent plasticity test reproduces the results of the power-law hardening plasticity test presented in [3], utilizing load case 6 ($\bar{\gamma} = 0.1$) with a constant temperature time history of $T = 1.0$ and the material parameterization given in table 41. The results of this test are presented in table 42 and figure 24, verifying the behavior of the thresholded plastic strain rate, and several of the strength constant parameters available in model 54.

Table 41: Material parameterization for the model 54 strain rate-dependent plasticity test

Parameter	Value
Elastic modulus, E	2.25
Poisson's ratio, ν	0.125
Strength coefficient, C_0	0.0
Strength coefficient, C_4	3.6
Strength coefficient, C_6	0.5
Threshold plastic strain rate, $\dot{\bar{\varepsilon}}^p_{thres}$	0.25

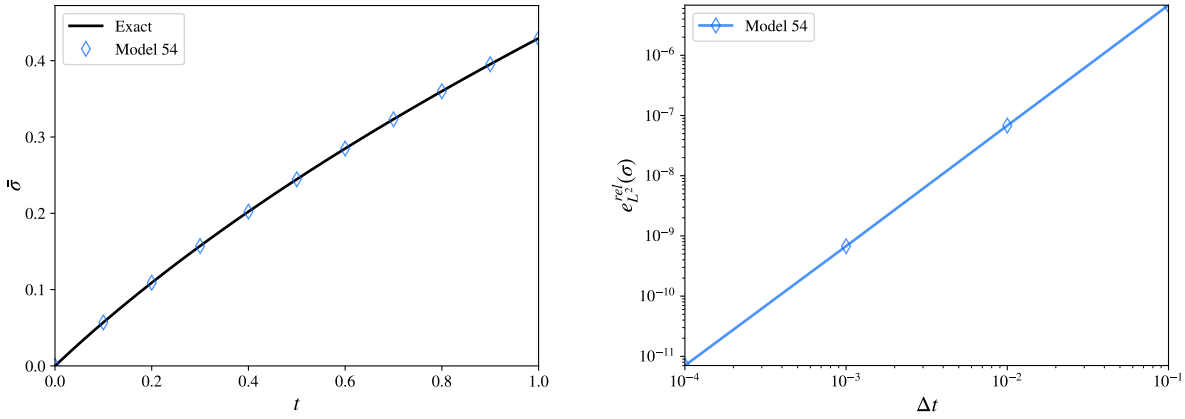

(a) Time-history plot of $\bar{\sigma}$ vs. t using $\Delta t = 0.1$.

(b) Convergence plot for $e^{\text{rel}}_{L^2}(\boldsymbol{\sigma})$ errors vs. Δt.

Figure 24: Model 54 strain rate-dependent plasticity test.

Table 42: Computed errors for the model 54 rate-dependent plasticity test.

Model	$e^{\text{rel}}_{L^2}(\boldsymbol{\sigma})$	r	$e^{\text{abs}}_{L^2}(\varepsilon_{33})$	r	$e^{\text{rel}}_{L^2}(\bar{\varepsilon}^p)$	r	Status
54	7.040e-12	1.98	2.318e-15	2.00	7.722e-12	1.95	✓

4.4 Bammann Plasticity (Models 38 & 39)

The Bammann plasticity model discussed in [1] serves as the basis for both models 38 and 39. The theoretical behavior of the Bammann plasticity model is consistent with the concept of a viscoplastic overstress function, wherein the rate of plastic strain is driven by the following flow rule when $\bar{\sigma} > Y(T) + \kappa$:

$$\dot{\boldsymbol{\varepsilon}}^p = \dot{\bar{\varepsilon}}^p \mathbf{n}, \qquad \dot{\bar{\varepsilon}}^p = F(T) \sinh\left[\frac{\bar{\sigma} - \kappa - Y(T)}{V(T)}\right], \tag{42}$$

and the following terms are defined:

$$\mathbf{n} = \frac{3}{2\bar{\sigma}}\boldsymbol{\eta}, \qquad \bar{\sigma} = \sqrt{\frac{3}{2}\boldsymbol{\eta} : \boldsymbol{\eta}}, \qquad \boldsymbol{\eta} = \mathbf{s} - \frac{2}{3}\boldsymbol{\alpha}, \qquad \mathbf{s} = \boldsymbol{\sigma} - \frac{1}{3}\mathrm{tr}(\boldsymbol{\sigma}). \tag{43}$$

The above flow rule may be inverted to obtain an effective rate-dependent yield condition:

$$f_y = \bar{\sigma} - \sigma_y(T, \bar{\varepsilon}^p, \dot{\bar{\varepsilon}}^p) \leq 0, \qquad \sigma_y(T, \bar{\varepsilon}^p, \dot{\bar{\varepsilon}}^p) = Y(T) + \kappa + V(T) \sinh^{-1}\left[\frac{\dot{\bar{\varepsilon}}^p}{F(T)}\right], \qquad \dot{\bar{\varepsilon}}^p = \sqrt{\frac{2}{3}\dot{\boldsymbol{\varepsilon}}^p : \dot{\boldsymbol{\varepsilon}}^p}, \tag{44}$$

whose time-rate $\dot{f}_y = 0$ establishes the consistency condition during plastic loading.

As implemented, the common behavior of models 38 and 39 (as described in [1]) is actually consistent with the following modified yield condition which depends upon the (trial) effective total strain rate $\dot{\bar{\varepsilon}}$ (including the volumetric part) in place of the equivalent plastic strain rate:

$$f_y = \bar{\sigma} - \sigma_y(T, \bar{\varepsilon}^p, \dot{\bar{\varepsilon}}) \leq 0, \qquad \dot{\bar{\varepsilon}} = \sqrt{\frac{2}{3}\dot{\boldsymbol{\varepsilon}} : \dot{\boldsymbol{\varepsilon}}}. \tag{45}$$

Consequently, the model does not behave in a viscoplastic manner consistent with an overstress concept. Rather, the yield stress varies directly with the rate of external loading, such that the model will exhibit no plastic flow at sufficiently high strain rates, even if $\bar{\sigma} > Y(T) + \kappa$.

If the following conditions are satisfied: the material exhibits no hardening behavior ($\kappa \equiv 0$ and $\boldsymbol{\alpha} \equiv \mathbf{0}$); the temperature remains constant ($\dot{T} = 0$); and the total strain rate remains constant, then one recovers perfectly plastic behavior with a constant flow stress of σ_0 given by:

$$\sigma_0 = Y(T) + V(T) \sinh^{-1}\left[\frac{\dot{\bar{\varepsilon}}}{F(T)}\right]. \tag{46}$$

The Bammann rate-dependent plasticity test utilizes load case 6 ($\bar{\gamma} = 0.5$) and the material parameterization in table 43. The results are presented in figure 25 and table 44, confirming the expected behavior for both models 38 and 39.

Table 43: Material parameterization for the Bammann rate-dependent plasticity test.

Parameter	Value
Elastic modulus, E	2.0
Poisson's ratio, ν	0.0
Rate-independent yield stress, $Y(T)$	0.1
Rate-dependence factor, $F(T)$	1.0
Rate-dependence factor, $V(T)$	1.0

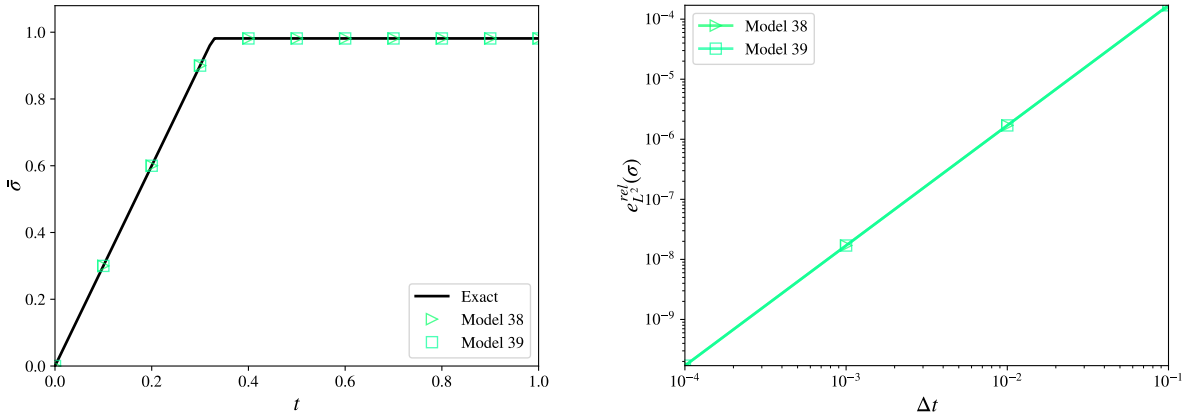

(a) Time-history plot of $\bar{\sigma}$ vs. t using $\Delta t = 0.1$.

(b) Convergence plot for $e^{\text{rel}}_{L^2}(\boldsymbol{\sigma})$ errors vs. Δt.

Figure 25: Bammann rate-dependent plasticity test.

Table 44: Computed errors for the Bammann rate-dependent plasticity test.

Model	$e^{\text{rel}}_{L^2}(\boldsymbol{\sigma})$	r	$e^{\text{abs}}_{L^2}(\varepsilon_{33})$	r	$e^{\text{rel}}_{L^2}(\bar{\varepsilon}^p)$	r	Status
38	1.702e-10	2.00	2.634e-12	2.00	1.262e-10	2.00	✓
39	1.702e-10	2.00	2.634e-12	2.00	1.262e-10	2.00	✓

Models 38 and 39 also incorporate dynamic and static recovery effects for both isotropic and kinematic hardening plasticity. The recovery of the isotropic and kinematic hardening variables (κ and $\boldsymbol{\alpha}$, respectively) are governed by the following evolution equations according to reference [1]:

$$\dot{\kappa} = H(T)|\dot{\boldsymbol{\varepsilon}}^p| - [R_d(T)\dot{\bar{\varepsilon}}^p + R_s(T)]\,\kappa^2, \tag{47}$$

$$\dot{\boldsymbol{\alpha}} = h(T)\dot{\boldsymbol{\varepsilon}}^p - [r_d(T)\dot{\bar{\varepsilon}}^p + r_s(T)]\,\bar{\alpha}\boldsymbol{\alpha}. \tag{48}$$

The actual implementation of the model in DYNA3D replaces the effective plastic strain rate $\dot{\bar{\varepsilon}}^p$ with the total effective strain rate $\dot{\bar{\varepsilon}}$ (including the volumetric strain rate) appearing in the dynamic recovery terms, such that:

$$\dot{\kappa} = H(T)|\dot{\boldsymbol{\varepsilon}}^p| - [R_d(T)\dot{\bar{\varepsilon}} + R_s(T)]\,\kappa^2, \tag{49}$$

$$\dot{\boldsymbol{\alpha}} = h(T)\dot{\boldsymbol{\varepsilon}}^p - [r_d(T)\dot{\bar{\varepsilon}} + r_s(T)]\,\bar{\alpha}\boldsymbol{\alpha}. \tag{50}$$

An important note regarding the behavior of the above terms concerns the fact that the hardening variables will continue to evolve even if the material is not being loaded plastically. The physicality and thermodynamic consistency of this behavior is questionable, and likely warrants re-investigation of the underlying theory. However, a rigorous analysis is deemed beyond the scope of the present work. Present efforts are instead focused on verifying the resulting behavior of the model consistent with the above.

In the abscence of linear hardening effects ($H(T) \equiv 0$, $h(T) \equiv 0$), and assuming that the plastic loading direction $\mathbf{n}$ remains fixed such that

$$\boldsymbol{\alpha}(t) = \bar{\alpha}(t)\,\mathbf{n}, \tag{51}$$

one may show that

$$\dot{\kappa} = -\,[R_d(T)\dot{\bar{\varepsilon}} + R_s(T)]\,\kappa^2, \tag{52}$$

$$\dot{\bar{\alpha}} = -\,[r_d(T)\dot{\bar{\varepsilon}} + r_s(T)]\,\bar{\alpha}^2. \tag{53}$$

If $\dot{\bar{\varepsilon}}$ remains constant, then the independent time-evolution of $\kappa(t)$ and $\bar{\alpha}(t)$ with prescribed initial values $\kappa(0) = \kappa_0$ and $\bar{\alpha}(0) = \bar{\alpha}_0$ is exactly characterized by the following expressions:

$$\kappa(t) = \frac{\kappa_0}{\kappa_0\,[R_d(T)\dot{\bar{\varepsilon}} + R_s(T)]\,t + 1}, \tag{54}$$

$$\bar{\alpha}(t) = \frac{\bar{\alpha}_0}{\bar{\alpha}_0\,[r_d(T)\dot{\bar{\varepsilon}} + r_s(T)]\,t + 1}. \tag{55}$$

Assuming no rate- or temperature-dependent plasticity effects are active, the yield condition under proportional loading reduces to

$$f_y = |\bar{\sigma} - \bar{\alpha}(t)| - Y(T) - \kappa(t) \leq 0. \tag{56}$$

If $\bar{\sigma} - \bar{\alpha}(t) > 0$ during plastic loading, one obtains a direct expression for the effective plastic strain as a function of time:

$$\bar{\varepsilon}^p(t) = \left\langle \dot{\bar{\varepsilon}}t - \frac{Y(T) + \kappa(t) + \bar{\alpha}(t)}{3\mu} \right\rangle, \tag{57}$$

and the time of initial yielding t_0 is determined as the solution to the condition:

$$3\mu\dot{\bar{\varepsilon}}t_0 = Y(T) + \kappa(t_0) + \bar{\alpha}(t_0). \tag{58}$$

To adequately verify all of the aforementioned hardening recovery function parameters, a sequence of four tests are devised employing load case 6 ($\bar{\gamma} = 0.5$), and the separate material parameterizations given in tables 45, 47, 49, 51. The results are presented respectively in tables 46, 48, 50, 52 and figures 26-29, confirming the correct behavior of all relevant parameters.

Table 45: Material parameterization for the Bammann hardening plasticity test 1.

Parameter	Value
Elastic modulus, E	2.0
Poisson's ratio, ν	0.0
Rate-independent yield stress, $Y(T)$	0.1
Dynamic isotropic hardening recovery factor, $R_d(T)$	10.0
Initial isotropic hardening variable, κ_0	0.1

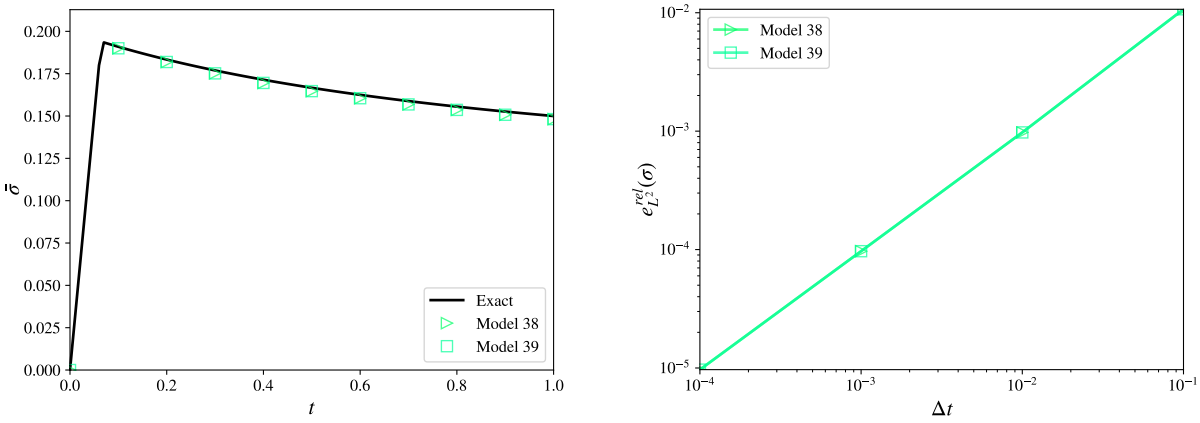

(a) Time-history plot of $\bar{\sigma}$ vs. t using $\Delta t = 0.1$.

(b) Convergence plot for $e^{\text{rel}}_{L^2}(\boldsymbol{\sigma})$ errors vs. Δt.

Figure 26: Bammann hardening plasticity test 1.

Table 46: Computed errors for the Bammann hardening plasticity test 1.

Model	$e^{\text{rel}}_{L^2}(\boldsymbol{\sigma})$	r	$e^{\text{abs}}_{L^2}(\varepsilon_{33})$	r	$e^{\text{rel}}_{L^2}(\bar{\varepsilon}^p)$	r	Status
38	9.683e-06	1.00	8.148e-12	2.00	1.001e-06	0.99	✓
39	9.683e-06	1.00	8.147e-12	2.00	1.001e-06	0.99	✓

Table 47: Material parameterization for the Bammann hardening plasticity test 2.

Parameter	Value
Elastic modulus, E	2.0
Poisson's ratio, ν	0.0
Rate-independent yield stress, $Y(T)$	0.1
Dynamic isotropic hardening recovery factor, $r_d(T)$	10.0
Initial kinematic hardening variable, α_{xx}	0.05
Initial kinematic hardening variable, α_{yy}	-0.05
Initial kinematic hardening variable, α_{xy}	0.0
Initial kinematic hardening variable, α_{yz}	0.05
Initial kinematic hardening variable, α_{zx}	0.05

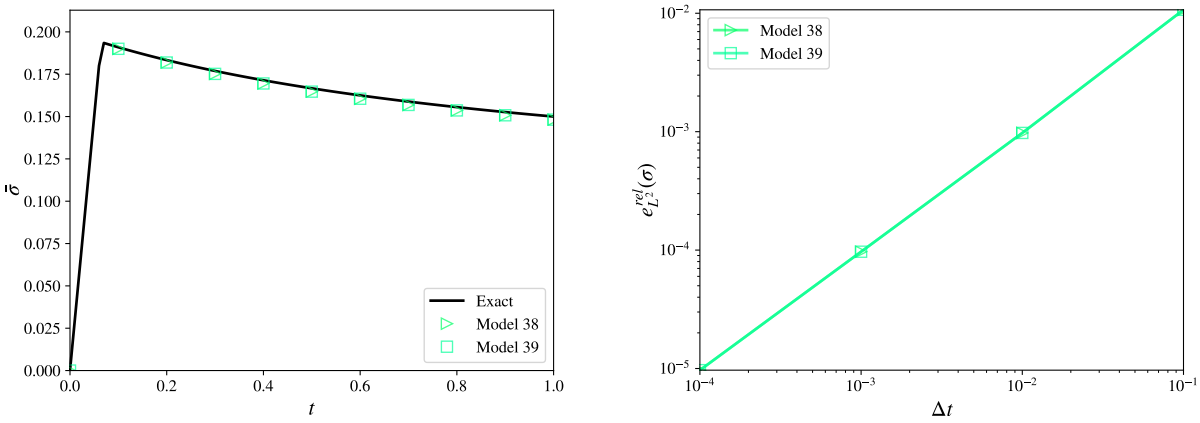

(a) Time-history plot of $\bar{\sigma}$ vs. t using $\Delta t = 0.1$.

(b) Convergence plot for $e_{L^2}^{\text{rel}}(\boldsymbol{\sigma})$ errors vs. Δt.

Figure 27: Bammann hardening plasticity test 2.

Table 48: Computed errors for the Bammann hardening plasticity test 2.

Model	$e_{L^2}^{\text{rel}}(\boldsymbol{\sigma})$	r	$e_{L^2}^{\text{abs}}(\varepsilon_{33})$	r	$e_{L^2}^{\text{rel}}(\bar{\varepsilon}^p)$	r	Status
38	9.683e-06	1.00	9.288e-12	2.00	1.001e-06	0.99	✓
39	9.683e-06	1.00	9.287e-12	2.00	1.001e-06	0.99	✓

Table 49: Material parameterization for the Bammann hardening plasticity test 3.

Parameter	Value
Elastic modulus, E	2.0
Poisson's ratio, ν	0.0
Rate-independent yield stress, $Y(T)$	0.1
Dynamic isotropic hardening recovery factor, $R_s(T)$	10.0
Initial isotropic hardening variable, κ_0	0.1

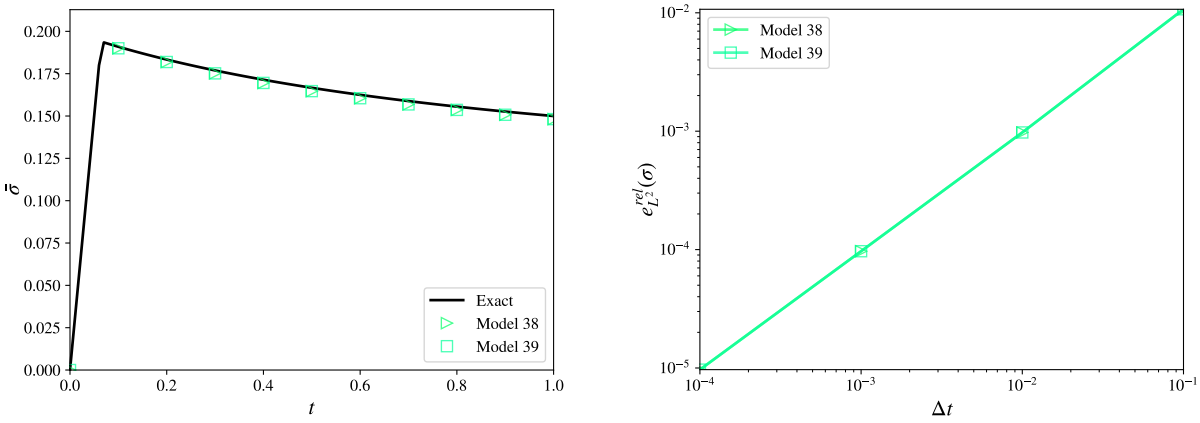

(a) Time-history plot of $\bar{\sigma}$ vs. t using $\Delta t = 0.1$.

(b) Convergence plot for $e^{\text{rel}}_{L^2}(\boldsymbol{\sigma})$ errors vs. Δt.

Figure 28: Bammann hardening plasticity test 3.

Table 50: Computed errors for the Bammann hardening plasticity test 3.

Model	$e^{\text{rel}}_{L^2}(\boldsymbol{\sigma})$	r	$e^{\text{abs}}_{L^2}(\varepsilon_{33})$	r	$e^{\text{rel}}_{L^2}(\bar{\varepsilon}^p)$	r	Status
38	9.683e-06	1.00	8.148e-12	2.00	1.001e-06	0.99	✓
39	9.683e-06	1.00	8.147e-12	2.00	1.001e-06	0.99	✓

Table 51: Material parameterization for the Bammann hardening plasticity test 4.

Parameter	Value
Elastic modulus, E	2.0
Poisson's ratio, ν	0.0
Rate-independent yield stress, $Y(T)$	0.1
Dynamic isotropic hardening recovery factor, $r_s(T)$	10.0
Initial kinematic hardening variable, α_{xx}	0.05
Initial kinematic hardening variable, α_{yy}	-0.05
Initial kinematic hardening variable, α_{xy}	0.0
Initial kinematic hardening variable, α_{yz}	0.05
Initial kinematic hardening variable, α_{zx}	0.05

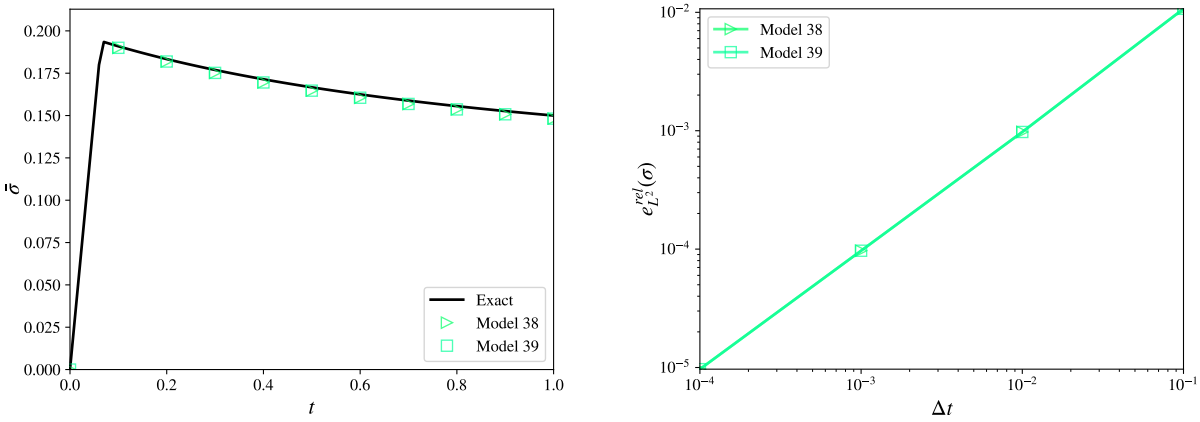

(a) Time-history plot of $\bar{\sigma}$ vs. t using $\Delta t = 0.1$.

(b) Convergence plot for $e_{L^2}^{\text{rel}}(\boldsymbol{\sigma})$ errors vs. Δt.

Figure 29: Bammann hardening plasticity test 4.

Table 52: Computed errors for the Bammann hardening plasticity test 4.

Model	$e_{L^2}^{\text{rel}}(\boldsymbol{\sigma})$	r	$e_{L^2}^{\text{abs}}(\varepsilon_{33})$	r	$e_{L^2}^{\text{rel}}(\bar{\varepsilon}^p)$	r	Status
38	9.683e-06	1.00	9.288e-12	2.00	1.001e-06	0.99	✓
39	9.683e-06	1.00	9.287e-12	2.00	1.001e-06	0.99	✓

4.5 Damage and Failure

Material models 15, 18, 19, 22, 24, 35, 39, 41, 50, 52, 54, 71, and 74 incorporate a variety of differing damage and failure modeling freatures. Because of the significant differences in the way that failure is handled for each of these models, altogether different tests are constructed for each material model in most cases, as described in the following sub-sections.

4.5.1 Minimum Time Step Deletion

Models 15, 19, 22, 24, 41, 50, 52, 54 allow for automatic element deletion to be triggered if an element's critical time step drops below a user-specified value of Δt_{crit}.

For a shell element material model with isotropic elastic properties E and ν, the critical sound speed $c = \sqrt{\frac{E}{\rho_0(1-\nu^2)}}$ is computed using the initial mass density ρ_0, and the maximum diagonal entry of the plane stress stiffness tensor, i.e. $E/(1-\nu^2)$.

For shell elements, the default method ($isdo = 0$) of computing the element's characteristic length scale (herein denoted by ℓ) is by dividing the shell's total area by its longest side. For load case 1 (parameterized by the isotropic strain rate $\bar{\gamma}$) using the single-element test setup described in [3], this implies $\ell(t) = 2\exp(\bar{\gamma}t)$.

The resulting stable time step Δt_{stab} for an element with sound speed c and characteristic length ℓ is computed via $\Delta t_{\text{stab}} = tssfac\,(\ell/c)$, where $tssfac$ is the time-step scale factor with a default value of $tssfac = 0.9$. Element deletion triggered by the condition $\Delta t_{\text{stab}} < \Delta t_{\text{crit}}$ therefore implies the following condition on the element's characteristic length prior to deletion: $\ell \geq c\,\Delta t_{\text{crit}}/tssfac$.

Assuming $\bar{\gamma} < 0$ (such that $\dot{\ell} < 0$) and $\Delta t_{\text{stab}} < \Delta t_{\text{crit}}$ initially at $t = 0$, the critical time $t_{\text{crit}} > 0$ at which the element will be deleted is determined as

$$t_{\text{crit}} = \frac{1}{\bar{\gamma}} \log\left(\frac{c\,\Delta t_{\text{crit}}}{2\,tssfac}\right). \tag{59}$$

For load case 1 ($\bar{\gamma} = -0.01$) and the material parameterization presented in table 53, the time of failure is approximately computed as $t_{\text{crit}} \approx 0.535$. This indicated time of deletion for all relevant models is confirmed by the results presented in table 54 and figure 30.

Table 53: Material parameterization for the minimum time step deletion test

Parameter	Value
Elastic modulus, E	7.5
Poisson's ratio, ν	0.25
Mass density, ρ_0	1.0
Time-step size for element deletion, Δt_{crit}	0.633
Time-step scale factor, $tssfac$	0.9 (default)

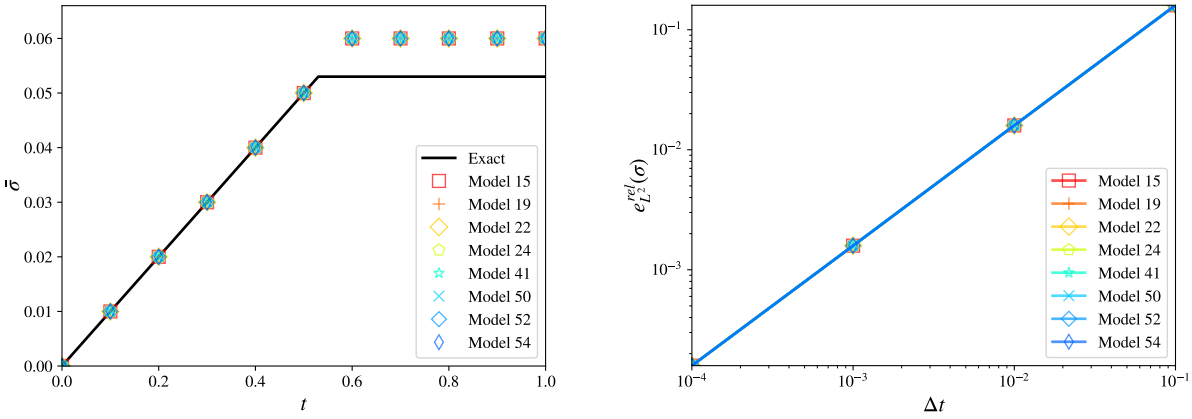

(a) Time-history plot of $\bar{\sigma}$ vs. t using $\Delta t = 0.1$.

(b) Convergence plot for $e^{\text{rel}}_{L^2}(\boldsymbol{\sigma})$ errors vs. Δt.

Figure 30: Minimum time step deletion test.

Table 54: Computed errors for the minimum time step deletion test.

Model	$e^{\text{rel}}_{L^2}(\boldsymbol{\sigma})$	r	$e^{\text{rel}}_{L^2}(\varepsilon_{33})$	r	$e^{\text{abs}}_{L^2}(\bar{\varepsilon}^p)$	r	Status
15	1.589e-04	0.98	1.589e-04	0.98	0.000e+00	-	✓
19	1.589e-04	0.98	1.589e-04	0.98	0.000e+00	-	✓
22	1.589e-04	0.98	1.589e-04	0.98	0.000e+00	-	✓
24	1.589e-04	0.98	1.589e-04	0.98	0.000e+00	-	✓
41	1.589e-04	0.98	1.589e-04	0.98	0.000e+00	-	✓
50	1.589e-04	0.98	1.589e-04	0.98	0.000e+00	-	✓
52	1.589e-04	0.98	1.589e-04	0.98	0.000e+00	-	✓
54	1.589e-04	0.98	1.589e-04	0.98	0.000e+00	-	✓

4.5.2 Plastic Strain Failure/Deletion

For shell elements, models 18, 24, and 71 provide a maximum equivalent plastic strain-based failure criterion, such that all stresses in the material are instantaneously reduced to zero when this criterion is exceeded. Additionally, models 18, 24, 35, 52, 54, and 71 support a maximum plastic strain deletion criterion. Shell elements are deleted once all of their integration points have met the deletion criterion.

Note that while model 4 allows for a maximum plastic strain failure criterion to be specified via the `eps_failure` keyword, this feature is not available for shell elements. Model 28 also provides a maximum plastic strain deactivation flag *pstrain*, but this feature is only available for Belytschko-Schwer beam elements.

As a supplementary note: model 35's maximum plastic strain deletion criterion also requires that failure also be detected by the specified forming limit diagram (FLD) prior to removal.

Considering an adaptation of the linear hardening plane stress plasticity test described in [3] using load case 2 ($\bar{\gamma} = 0.1$) and the (perfectly plastic) material parameterization presented in table 55, the time of failure due to the plastic strain deletion criterion is determined via

$$t_f = \frac{\sigma_0 + (3\mu + E_p)\bar{\varepsilon}_f^p}{3\mu\dot{\bar{\varepsilon}}} \approx 0.635, \tag{60}$$

where $\dot{\bar{\varepsilon}} = \frac{2}{\sqrt{3}}\bar{\gamma}$ for load case 2. The correct time of deletion for the ensuing plastic strain failure test is demonstrated in figure 31 and table 56.

Table 55: Material parameterization for the plastic strain failure/deletion test

Parameter	Value
Elastic modulus, E	2.25
Poisson's ratio, ν	0.125
Yield stress, σ_0	0.1
Tangent modulus, E_p	0.0
Maximum plastic strain, $\bar{\varepsilon}_f^p$	0.06

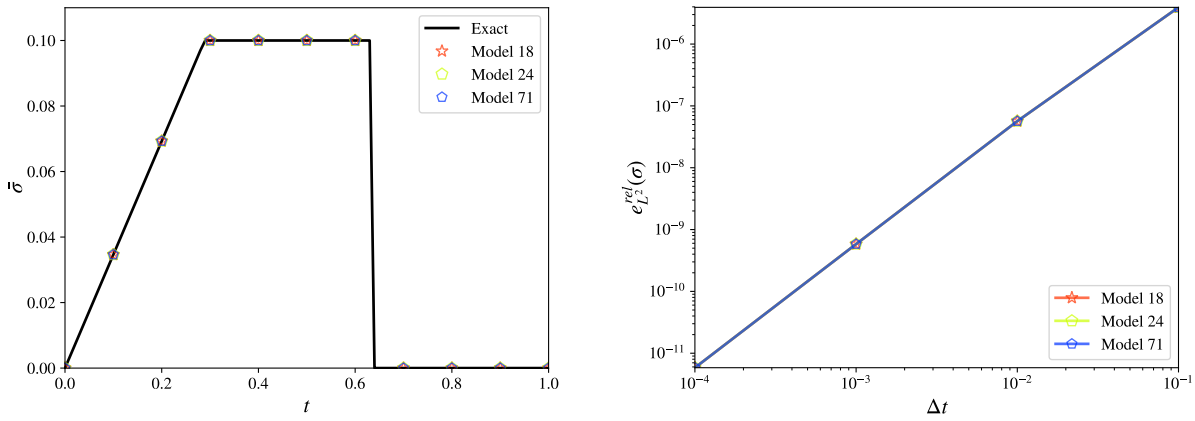

(a) Time-history plot of $\bar{\sigma}$ vs. t using $\Delta t = 0.1$.

(b) Convergence plot for $e_{L^2}^{\text{rel}}(\boldsymbol{\sigma})$ errors vs. Δt.

Figure 31: Plastic strain failure test.

Table 56: Computed errors for the plastic strain failure test.

Model	$e_{L^2}^{\text{rel}}(\boldsymbol{\sigma})$	r	$e_{L^2}^{\text{abs}}(\varepsilon_{33})$	r	$e_{L^2}^{\text{rel}}(\bar{\varepsilon}^p)$	r	Status
18	5.831e-12	1.83	3.943e-15	2.01	2.517e-04	0.98	✓
24	5.832e-12	1.83	5.270e-15	1.97	2.517e-04	0.98	✓
71	5.832e-12	1.83	5.430e-15	1.96	2.517e-04	0.98	✓

Retaining the same material parameterization as in table 55 while turning on the plastic strain-based element deletion flag, one obtains a similar test which ultimately results in the deletion of the element at time t_f. The results of the plastic strain deletion test presented in figure 32 and table 57 similarly confirm the expected time of deletion – coincident with the time of failure.

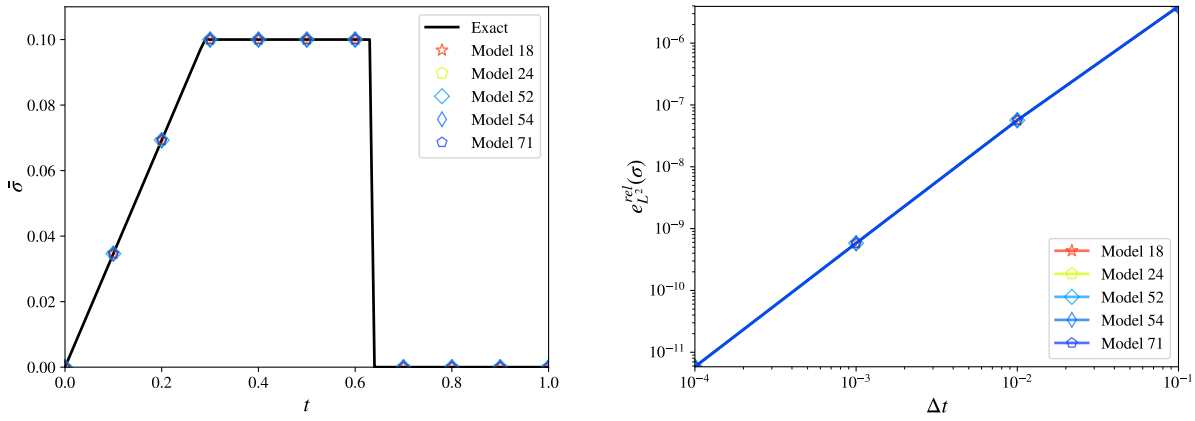

(a) Time-history plot of $\bar{\sigma}$ vs. t using $\Delta t = 0.1$.

(b) Convergence plot for $e^{\text{rel}}_{L^2}(\boldsymbol{\sigma})$ errors vs. Δt.

Figure 32: Plastic strain deletion test.

Table 57: Computed errors for the plastic strain deletion test.

Model	$e^{\text{rel}}_{L^2}(\boldsymbol{\sigma})$	r	$e^{\text{abs}}_{L^2}(\varepsilon_{33})$	r	$e^{\text{rel}}_{L^2}(\bar{\varepsilon}^p)$	r	Status
18	5.831e-12	1.83	2.987e-15	2.01	2.517e-04	0.98	✓
24	5.832e-12	1.83	5.270e-15	1.97	2.517e-04	0.98	✓
52	5.828e-12	1.83	9.874e-15	1.78	2.517e-04	0.98	✓
54	5.831e-12	1.83	4.821e-15	1.92	2.517e-04	0.98	✓
71	5.835e-12	1.83	4.221e-15	1.97	2.517e-04	0.98	✓

A separate reference solution was created specifically for model 35 to accomodate the fact that the stress components are not driven to zero in the aftermath of failure/deletion, although the loading and material parameters remain identical to those of the plastic strain deletion test for all other models. The results are presented in figure 33 and table 58. Nonetheless, while the implementation of the model is consistent with what is described in [5], it is recommended that the model be revised such that it produces consistent results with the other models.

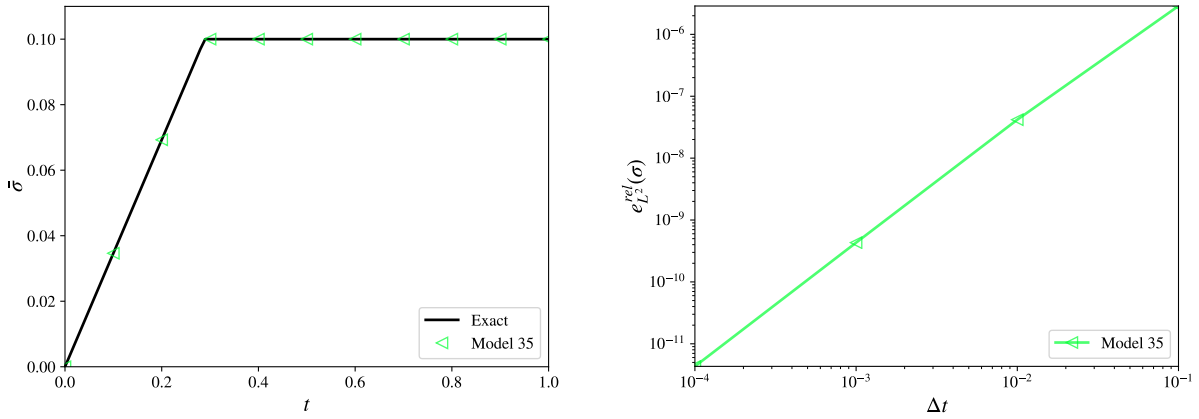

(a) Time-history plot of $\bar{\sigma}$ vs. t using $\Delta t = 0.1$.

(b) Convergence plot for $e^{\text{rel}}_{L^2}(\boldsymbol{\sigma})$ errors vs. Δt.

Figure 33: Plastic strain deletion test for model 35.

Table 58: Computed errors for the plastic strain deletion test using model 35.

Model	$e^{\text{rel}}_{L^2}(\boldsymbol{\sigma})$	r	$e^{\text{abs}}_{L^2}(\varepsilon_{33})$	r	$e^{\text{rel}}_{L^2}(\bar{\varepsilon}^p)$	r	Status
35	4.319e-12	1.84	1.712e-15	1.99	2.517e-04	0.98	⚠

4.5.3 Model 15 Damage & Spall

Model 15 includes an evolution condition for an internal damage variable which depends implicitly upon temperature, the total effective strain rate, and stress triaxiality (the ratio of pressure to effective stress). Progressive damage does not affect the strength of the material until the damage parameter achieves a threshold value of 1, at which point all stresses in the material are reduced to zero.

The Johnson-Cook failure criterion is satisfied when the accumulated damage parameter $D \geq 1$, where

$$D(t) = \int_0^t \frac{\dot{\bar{\varepsilon}}^p}{\varepsilon_f}\, dt, \tag{61}$$

and ε_f denotes the instantaneous strain at fracture, i.e.

$$\varepsilon_f = \left[D_1 + D_2 e^{D_3 \sigma^*}\right] \left[1 + D_4 \log(\dot{\varepsilon}^*)\right] \left[1 + D_5 T^*\right], \tag{62}$$

$$\sigma^* = \frac{p}{\bar{\sigma}}, \qquad p = -\frac{1}{3}\mathrm{tr}(\boldsymbol{\sigma}), \qquad \bar{\sigma} = \left(\frac{3}{2}\mathbf{s} : \mathbf{s}\right)^{\frac{1}{2}}, \qquad \dot{\varepsilon}^* = \frac{\dot{\bar{\varepsilon}}}{\dot{\varepsilon}_0}, \qquad T^* = \frac{T - T_r}{T_m - T_r}. \tag{63}$$

To fully verify the damage features included in model 15, it suffices to repeat the same failure test using a different specification of the damage parameters D_1 through D_5, thereby isolating and separately testing the effects of stress triaxiality, strain rate, and temperature. To this end, the following set of tests (based upon the pressure-dependent plasticity test setup proposed in [3]) are proposed in table 59:

Table 59: Model 15 damage tests

Test	D_1	D_2	D_3	D_4	D_5	ε_f	t_f
1	0.02	0	0	0	0	0.02	0.7
2	0	0.02	0	0	0	0.02	0.7
3	0	1	5.86	0	0	≈ 0.0201074	≈ 0.701074
4	1	0	0	0.306	0	≈ 0.0206388	≈ 0.706388
5	1	0	0	0	−1.96	0.02	0.7

For all of the above tests, the temperature of the material is held constant at $T = 0.5$ for the duration of the analysis, with $T_r = 0$ and $T_m = 1$ such that $T^* = 0.5\,\forall t$. Further, let $\dot{\varepsilon}_0 = 1$ such that $\dot{\varepsilon}^* = \dot{\bar{\varepsilon}}$. Because of the choice of loading in the pressure-dependent plasticity test, it follows that $\sigma^* = -\frac{2}{3}$ and $\dot{\bar{\varepsilon}}$ remain constant during plastic loading ($t \geq t_0$). These conditions imply that ε_f also remains constant during plastic loading. For all tests, the damage function may therefore be expressed directly as

$$D(t) = \frac{\bar{\varepsilon}^p(t)}{\varepsilon_f}, \qquad \bar{\varepsilon}^p(t) = 2\bar{\epsilon}\langle t - t_0\rangle, \qquad \varepsilon_f = \left[D_1 + D_2 e^{-D_3 \frac{2}{3}}\right] \left[1 + D_4 \log(\dot{\bar{\varepsilon}})\right] \left[1 + 0.5 D_5\right], \tag{64}$$

and the same specification of material and loading parameters ($E = 24$, $\nu = 0.1$, $\bar{\epsilon} = 0.05$, $\sigma_0 = 2.0$, $k_p = 1.0$, $t_0 = 0.5$) as for the pressure-dependent plasticity test is maintained. The time of failure of the material $t_f = t_0 + \frac{\varepsilon_f}{2\bar{\epsilon}}$ for the chosen damage parameters summarized in table 59 occurs when $\bar{\varepsilon}^p(t_f) = \varepsilon_f$ (when $D = 1$). The results for each model 15 damage test are presented in tables 60-64, and figures 34-38.

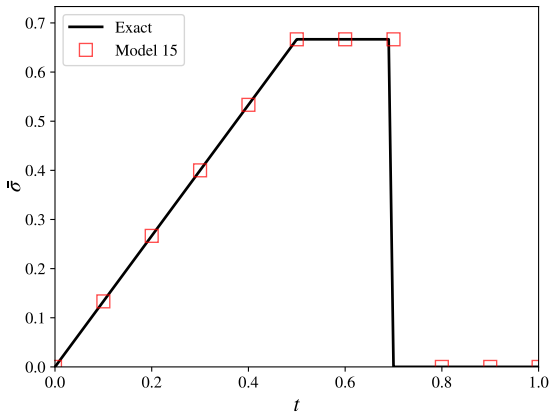

(a) Time-history plot of $\bar{\sigma}$ vs. t using $\Delta t = 0.1$.

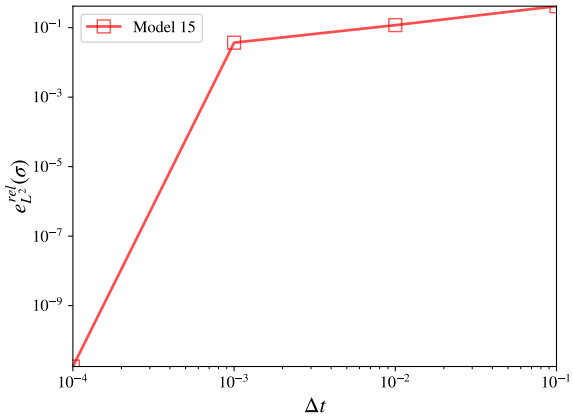

(b) Convergence plot for $e^{\text{rel}}_{L^2}(\boldsymbol{\sigma})$ errors vs. Δt.

Figure 34: Model 15 damage test 1.

Table 60: Computed errors for the model 15 damage test 1.

Model	$e^{\text{rel}}_{L^2}(\boldsymbol{\sigma})$	r	$e^{\text{rel}}_{L^2}(\varepsilon_{33})$	r	$e^{\text{rel}}_{L^2}(\bar{\varepsilon}^p)$	r	Status
15	1.771e-11	0.50	3.481e-11	0.94	5.623e-11	0.94	✓

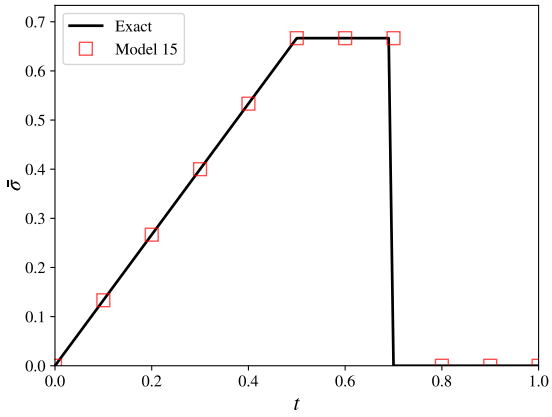

(a) Time-history plot of $\bar{\sigma}$ vs. t using $\Delta t = 0.1$.

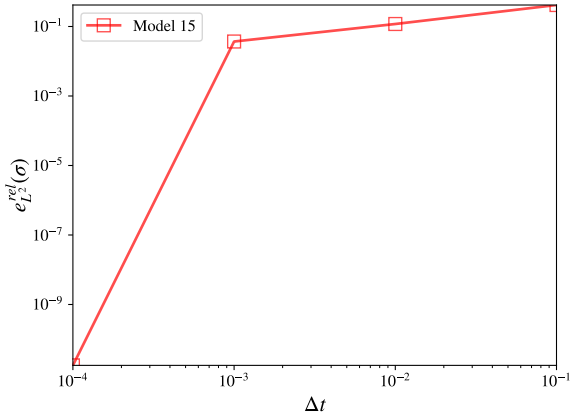

(b) Convergence plot for $e^{\text{rel}}_{L^2}(\boldsymbol{\sigma})$ errors vs. Δt.

Figure 35: Model 15 damage test 2.

Table 61: Computed errors for the model 15 damage test 2.

Model	$e^{\text{rel}}_{L^2}(\boldsymbol{\sigma})$	r	$e^{\text{rel}}_{L^2}(\varepsilon_{33})$	r	$e^{\text{rel}}_{L^2}(\bar{\varepsilon}^p)$	r	Status
15	1.771e-11	0.50	3.481e-11	0.94	5.623e-11	0.94	✓

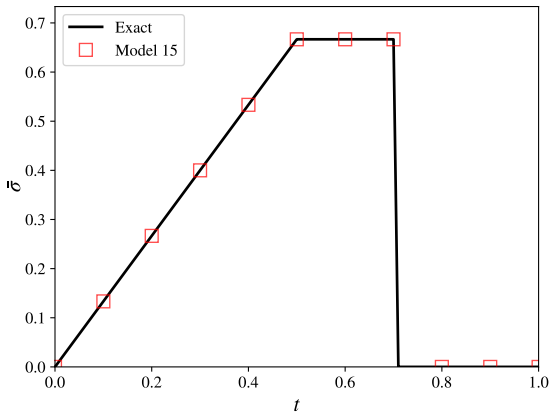

(a) Time-history plot of $\bar{\sigma}$ vs. t using $\Delta t = 0.1$.

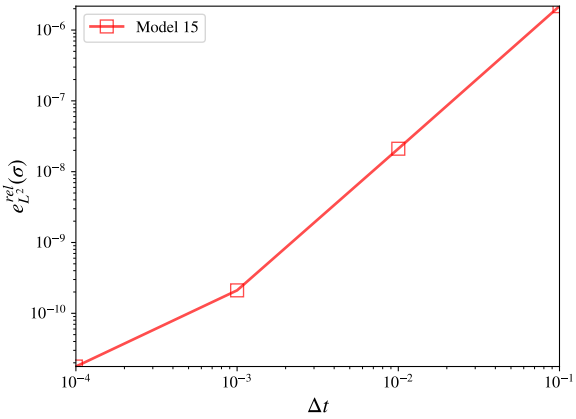

(b) Convergence plot for $e^{\text{rel}}_{L^2}(\boldsymbol{\sigma})$ errors vs. Δt.

Figure 36: Model 15 damage test 3.

Table 62: Computed errors for the model 15 damage test 3.

Model	$e^{\text{rel}}_{L^2}(\boldsymbol{\sigma})$	r	$e^{\text{rel}}_{L^2}(\varepsilon_{33})$	r	$e^{\text{rel}}_{L^2}(\bar{\varepsilon}^p)$	r	Status
15	1.773e-11	1.08	7.452e-05	0.98	1.162e-04	0.98	✓

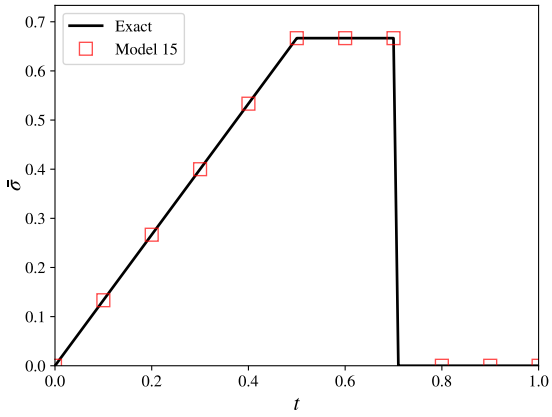

(a) Time-history plot of $\bar{\sigma}$ vs. t using $\Delta t = 0.1$.

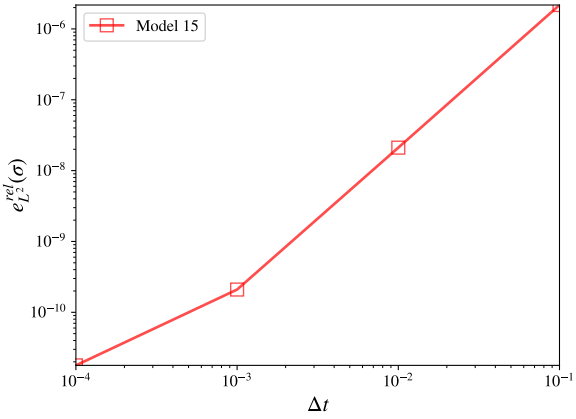

(b) Convergence plot for $e^{\text{rel}}_{L^2}(\boldsymbol{\sigma})$ errors vs. Δt.

Figure 37: Model 15 damage test 4.

Table 63: Computed errors for the model 15 damage test 4.

Model	$e^{\text{rel}}_{L^2}(\boldsymbol{\sigma})$	r	$e^{\text{rel}}_{L^2}(\varepsilon_{33})$	r	$e^{\text{rel}}_{L^2}(\bar{\varepsilon}^p)$	r	Status
15	1.783e-11	1.07	3.286e-05	0.77	5.085e-05	0.77	✓

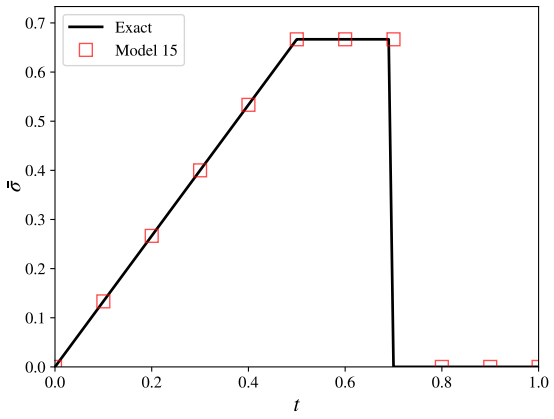

(a) Time-history plot of $\bar{\sigma}$ vs. t using $\Delta t = 0.1$.

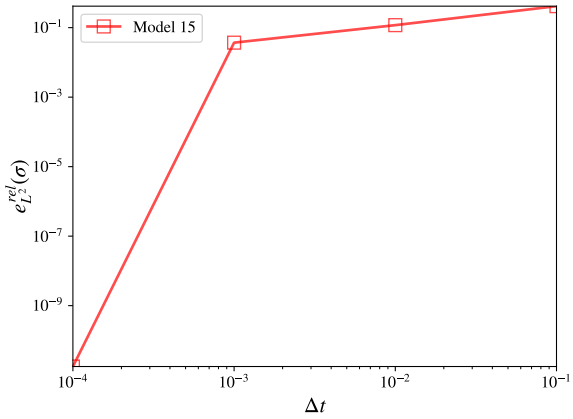

(b) Convergence plot for $e_{L^2}^{\text{rel}}(\boldsymbol{\sigma})$ errors vs. Δt.

Figure 38: Model 15 damage test 5.

Table 64: Computed errors for the model 15 damage test 5.

Model	$e_{L^2}^{\text{rel}}(\boldsymbol{\sigma})$	r	$e_{L^2}^{\text{rel}}(\varepsilon_{33})$	r	$e_{L^2}^{\text{rel}}(\bar{\varepsilon}^p)$	r	Status
15	1.771e-11	0.50	3.481e-11	0.94	5.623e-11	0.94	✓

Additionally, if the flag for the modified ε_f vs. σ^* curve is set to active, then the rate- and temperature-invariant fracture strain (prior to being multiplied by the rate- and temperature-dependent scaling factors) will instead be computed as

$$\varepsilon_f(\sigma^*) = \begin{cases} \varepsilon_f^{min}, & \sigma^* < \sigma_{spall}^* \\ \varepsilon_f^{min} + \frac{\sigma^* - \sigma_{spall}^*}{\sigma_{tran}^* - \sigma_{spall}^*}\left(D_1 + D_2 e^{D_3 \sigma_{tran}^*} - \varepsilon_f^{min}\right), & \sigma_{spall}^* \leq \sigma^* < \sigma_{tran}^* \\ D_1 + D_2 e^{D_3 \sigma^*}, & \sigma^* \geq \sigma_{tran}^* \end{cases} . \tag{65}$$

Assuming no rate- or temperature dependence ($D_4 = D_4 = 0$), the constant fracture strain $\varepsilon_f\left(\sigma^* = -\frac{2}{3}\right)$ determined from the preceeding derivations is obtained using the same material and loading parameters as for damage tests 1-5. The results for each "modified" damage test 1-3 for model 15 are presented in tables 66-68, and figures 39-41.

Table 65: Model 15 modified damage tests

Test	D_1	D_2	D_3	σ_{spall}^*	σ_{tran}^*	ε_f^{min}	ε_f	t_f
1	0.02	0.02	5.0	-0.5	-0.25	0.02	0.02	0.7
2	0.02	0.02	5.0	-1.0	-0.25	0.016	≈ 0.0203245	≈ 0.703245
3	0.02	0.02	5.0	-1.0	-0.5	0.018	≈ 0.0204278	≈ 0.704278

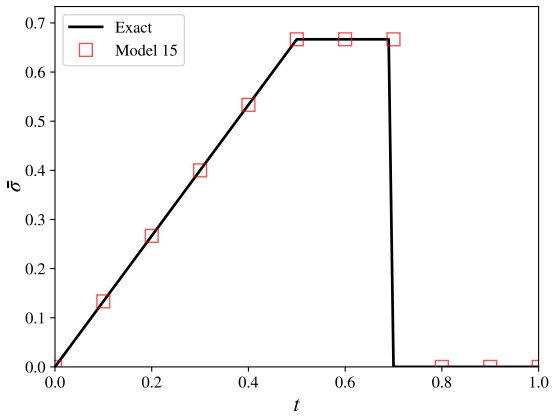

(a) Time-history plot of $\bar{\sigma}$ vs. t using $\Delta t = 0.1$.

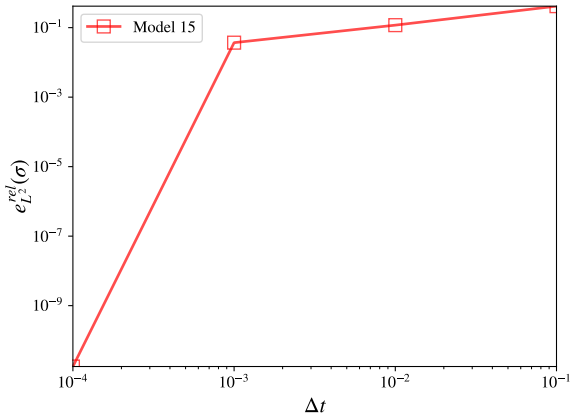

(b) Convergence plot for $e^{\text{rel}}_{L^2}(\boldsymbol{\sigma})$ errors vs. Δt.

Figure 39: Model 15 modified damage test 1.

Table 66: Computed errors for the model 15 modified damage test 1.

Model	$e^{\text{rel}}_{L^2}(\boldsymbol{\sigma})$	r	$e^{\text{rel}}_{L^2}(\varepsilon_{33})$	r	$e^{\text{rel}}_{L^2}(\bar{\varepsilon}^p)$	r	Status
15	1.771e-11	0.50	3.481e-11	0.94	5.623e-11	0.94	✓

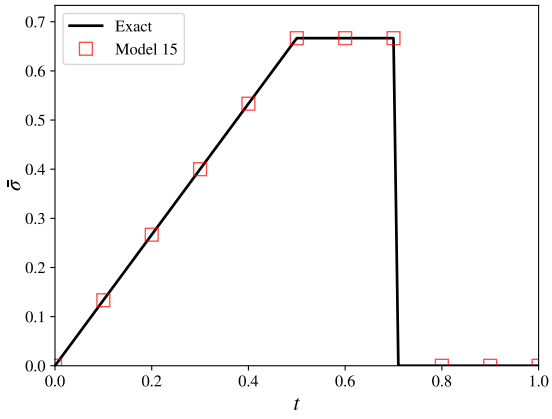

(a) Time-history plot of $\bar{\sigma}$ vs. t using $\Delta t = 0.1$.

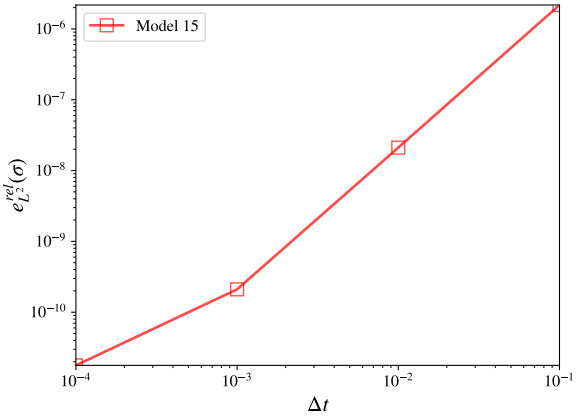

(b) Convergence plot for $e^{\text{rel}}_{L^2}(\boldsymbol{\sigma})$ errors vs. Δt.

Figure 40: Model 15 modified damage test 2.

Table 67: Computed errors for the model 15 modified damage test 2.

Model	$e^{\text{rel}}_{L^2}(\boldsymbol{\sigma})$	r	$e^{\text{rel}}_{L^2}(\varepsilon_{33})$	r	$e^{\text{rel}}_{L^2}(\bar{\varepsilon}^p)$	r	Status
15	1.777e-11	1.07	1.574e-04	0.95	2.447e-04	0.95	✓

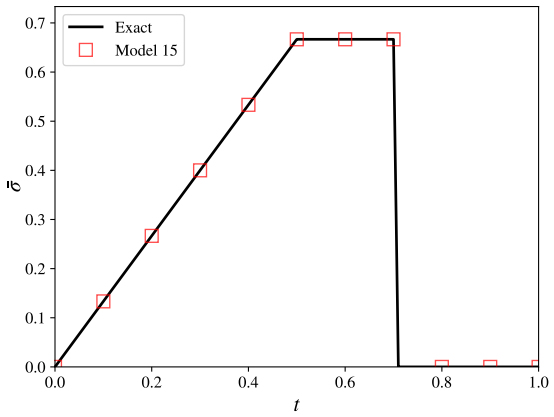

(a) Time-history plot of $\bar{\sigma}$ vs. t using $\Delta t = 0.1$.

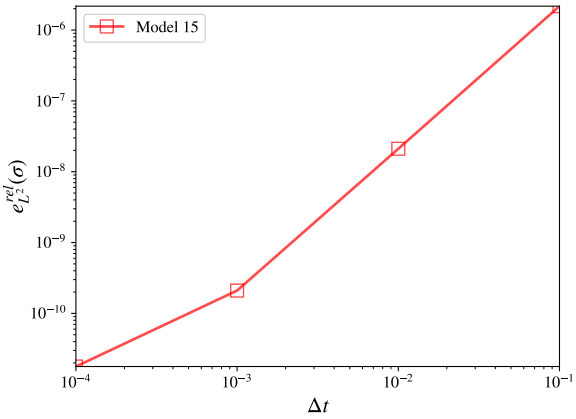

(b) Convergence plot for $e^{\text{rel}}_{L^2}(\boldsymbol{\sigma})$ errors vs. Δt.

Figure 41: Model 15 modified damage test 3.

Table 68: Computed errors for the model 15 modified damage test 3.

Model	$e^{\text{rel}}_{L^2}(\boldsymbol{\sigma})$	r	$e^{\text{rel}}_{L^2}(\varepsilon_{33})$	r	$e^{\text{rel}}_{L^2}(\bar{\varepsilon}^p)$	r	Status
15	1.779e-11	1.07	6.255e-05	0.90	9.710e-05	0.90	✓

Additional spall features applicable to shell elements allow for material model 15 to fail according to a maximum pressure/principal stress criterion, at which point all stresses in the material are reduced to zero.

The isotropic elastic properties $E = 2.4$ and $\nu = 0.2$ are utilized, and the other relevant parameters used for each test are given in table 69. The results for each model 15 spall test are presented in tables 70-72, and figures 42-44.

Table 69: Model 15 spall tests

Test	load case	$\bar{\gamma}$	$ISPALL$	p_{cut}/σ_m	t_f
1	2	-0.05	2	+0.05	0.5
2	1	+0.05	3	-0.05	0.5
3	2	-0.05	4	+0.05	0.5

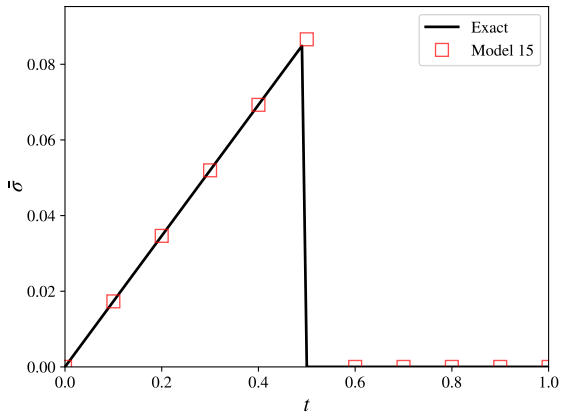

(a) Time-history plot of $\bar{\sigma}$ vs. t using $\Delta t = 0.1$.

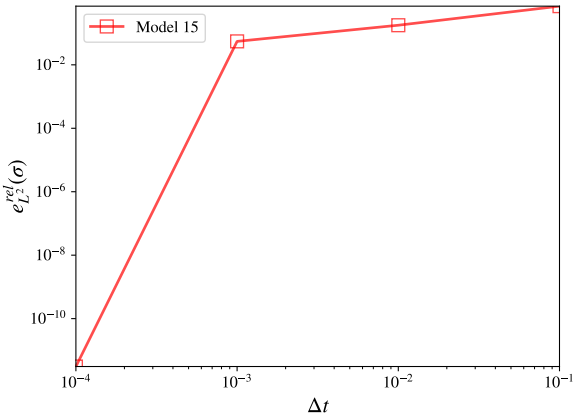

(b) Convergence plot for $e^{\text{rel}}_{L^2}(\boldsymbol{\sigma})$ errors vs. Δt.

Figure 42: Model 15 spall test 1.

Table 70: Computed errors for the model 15 spall test 1.

Model	$e^{\text{rel}}_{L^2}(\boldsymbol{\sigma})$	r	$e^{\text{abs}}_{L^2}(\varepsilon_{33})$	r	$e^{\text{abs}}_{L^2}(\bar{\varepsilon}^p)$	r	Status
15	3.092e-12	0.50	2.939e-16	2.00	0.000e+00	-	✓

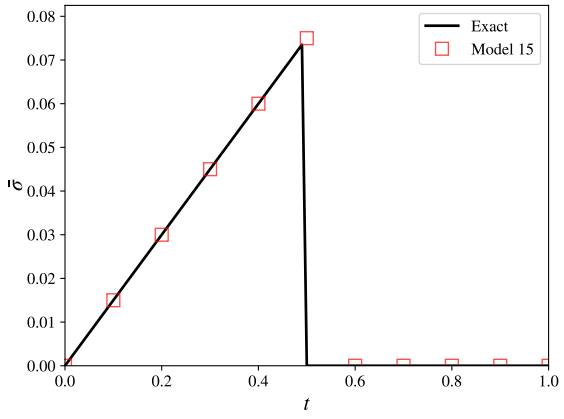

(a) Time-history plot of $\bar{\sigma}$ vs. t using $\Delta t = 0.1$.

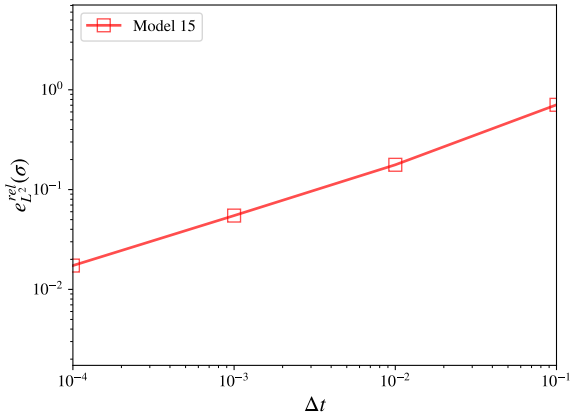

(b) Convergence plot for $e^{\text{rel}}_{L^2}(\boldsymbol{\sigma})$ errors vs. Δt.

Figure 43: Model 15 spall test 2.

Table 71: Computed errors for the model 15 spall test 2.

Model	$e^{\text{rel}}_{L^2}(\boldsymbol{\sigma})$	r	$e^{\text{rel}}_{L^2}(\varepsilon_{33})$	r	$e^{\text{abs}}_{L^2}(\bar{\varepsilon}^p)$	r	Status
15	1.732e-02	0.50	3.055e-12	2.00	0.000e+00	-	✓

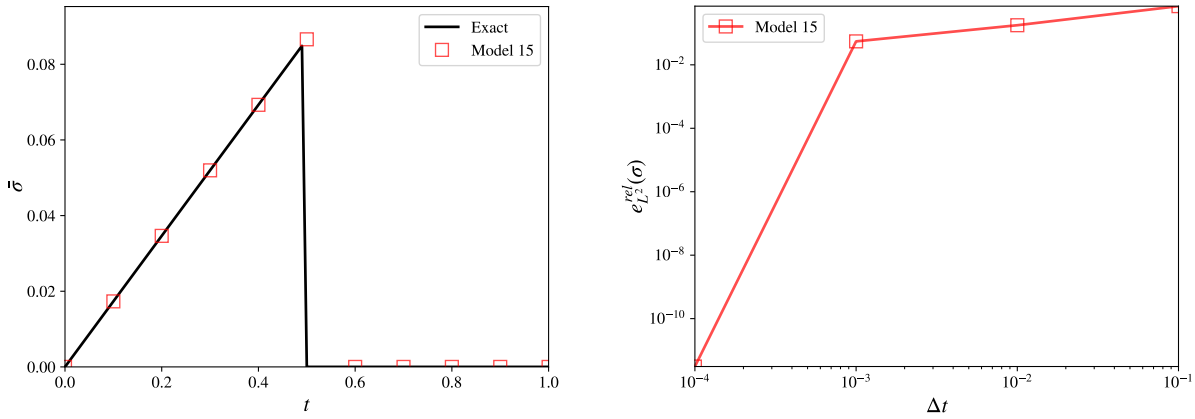

(a) Time-history plot of $\bar{\sigma}$ vs. t using $\Delta t = 0.1$.

(b) Convergence plot for $e_{L^2}^{\text{rel}}(\boldsymbol{\sigma})$ errors vs. Δt.

Figure 44: Model 15 spall test 3.

Table 72: Computed errors for the model 15 spall test 3.

Model	$e_{L^2}^{\text{rel}}(\boldsymbol{\sigma})$	r	$e_{L^2}^{\text{abs}}(\varepsilon_{33})$	r	$e_{L^2}^{\text{abs}}(\bar{\varepsilon}^p)$	r	Status
15	3.092e-12	0.50	2.939e-16	2.00	0.000e+00	-	✓

4.5.4 Model 19 Failure

Model 19 possesses a strain-rate dependent effective failure stress. For the accompanying model 19 failure test, load case 2 ($\bar{\gamma} = 0.05$) is utilized with the material parameterization given in table 73. The results are presented in table 74 and figure 45, confirming the anticipated failure of the material when $\bar{\sigma} > \bar{\sigma}_f$.

Table 73: Material parameterization for the model 19 failure test

Parameter	Value
Elastic modulus, E	2.4
Poisson's ratio, ν	0.2
Effective failure stress, $\bar{\sigma}_f$	0.1

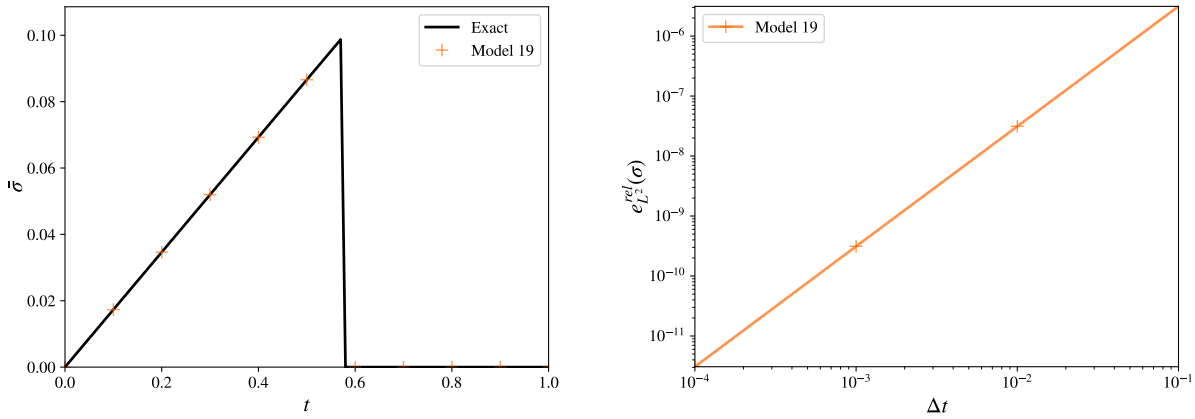

(a) Time-history plot of $\bar{\sigma}$ vs. t using $\Delta t = 0.1$.

(b) Convergence plot for $e_{L^2}^{\text{rel}}(\boldsymbol{\sigma})$ errors vs. Δt.

Figure 45: Model 19 failure test.

Table 74: Computed errors for the model 19 failure test.

Model	$e_{L^2}^{\text{rel}}(\boldsymbol{\sigma})$	r	$e_{L^2}^{\text{abs}}(\varepsilon_{33})$	r	$e_{L^2}^{\text{abs}}(\bar{\varepsilon}^p)$	r	Status
19	3.075e-12	1.94	1.572e-16	2.00	0.000e+00	-	✓

4.5.5 Model 22 & 41 Failure

Models 22 and 41 include multiple failure criteria for a fiber-reinforced laminated composite material, consisting of the following failure modes for shell elements:

- Rupture of the fibers: the in-plane shear stress and the normal stress in the fiber direction are reduced to zero over 100 time steps.
- Cracking of the matrix: the in-plane shear stress and the normal stress in the tranvserse direction are reduced to zero over 100 time steps.
- Crushing of the matrix: the in-plane shear stress and the normal stress in the transverse direction are reduced to zero over 100 time steps.

Model 41 is defined similarly to model 22 with regard to its variety of failure modes, but differs in that model 41 includes a bi-linear elastic response to account for slackness in the fiber weave. If the bi-linear elastic response of model 41 is deprecated such that its response is purely linear, then a unified set of failure tests may be devised for both models 22 and 41.

It is worth noting that for models which incorporate orthotropic elasticity, the preferred directions of the material do not rotate relative to the lamina coordinate system of the shell element. Consequently, given a chosen in-plane orientation of the fiber direction with angle β measured counter-clockwise from the X_1 axis, we may establish the following definitions for the in-plane strains defined in the element's material coordinate system:

$$\begin{bmatrix} \varepsilon_{aa} & \varepsilon_{ab} \\ \varepsilon_{ab} & \varepsilon_{bb} \end{bmatrix} = \mathbf{Q} \begin{bmatrix} \varepsilon_{11} & \varepsilon_{12} \\ \varepsilon_{12} & \varepsilon_{22} \end{bmatrix} \mathbf{Q}^T, \qquad \mathbf{Q} = \begin{bmatrix} \cos(\beta) & \sin(\beta) \\ -\sin(\beta) & \cos(\beta) \end{bmatrix}, \tag{66}$$

and thus

$$\varepsilon_{aa} = \varepsilon_{11} \cos^2(\beta) + \varepsilon_{22} \sin^2(\beta) + \varepsilon_{12} \sin(2\beta), \tag{67}$$

$$\varepsilon_{bb} = \varepsilon_{11} \sin^2(\beta) + \varepsilon_{22} \cos^2(\beta) - \varepsilon_{12} \sin(2\beta), \tag{68}$$

$$\varepsilon_{ab} = \frac{\varepsilon_{22} - \varepsilon_{11}}{2} \sin(2\beta) + \varepsilon_{12} \left[\cos^2(\beta) - \sin^2(\beta)\right]. \tag{69}$$

In particular, if $\beta = 0$:

$$\varepsilon_{aa} = \varepsilon_{11}, \qquad \varepsilon_{bb} = \varepsilon_{22}, \qquad \varepsilon_{ab} = \varepsilon_{12}. \tag{70}$$

For simplicity, the material properties are selected such that $\nu_{ba} = \nu_{ca} = \nu_{cb} = 0$, and thus it suffices to express the in-plane stresses in the material coordinate system as:

$$\sigma_{aa}(t) = E_a \, \varepsilon_{aa}(t), \qquad \sigma_{bb}(t) = E_b \, \varepsilon_{bb}(t), \qquad \sigma_{ab}(t) = 2\mu_{ab} \, \varepsilon_{ab}(t). \tag{71}$$

The stress-based failure criteria for fiber breakage, matrix cracking, and matrix crushing are expressed respectively as:

$$e_f = \left(\frac{\langle \sigma_{aa} \rangle}{X_t} \right)^2 + \frac{\frac{\sigma_{ab}^2}{2\mu_{ab}} + \frac{3}{4}\alpha\sigma_{ab}^4}{\frac{S_c^2}{2\mu_{ab}} + \frac{3}{4}\alpha S_c^4} \leq 1, \tag{72}$$

$$e_m = \left(\frac{\langle \sigma_{bb} \rangle}{Y_t} \right)^2 + \frac{\frac{\sigma_{ab}^2}{2\mu_{ab}} + \frac{3}{4}\alpha\sigma_{ab}^4}{\frac{S_c^2}{2\mu_{ab}} + \frac{3}{4}\alpha S_c^4} \leq 1, \tag{73}$$

$$e_d = \left(\frac{\langle -\sigma_{bb} \rangle}{2S_c} \right)^2 + \left(\frac{Y_c^2}{4S_c^2} - 1 \right) \frac{\sigma_{bb}}{Y_c} + \frac{\frac{\sigma_{ab}^2}{2\mu_{ab}} + \frac{3}{4}\alpha\sigma_{ab}^4}{\frac{S_c^2}{2\mu_{ab}} + \frac{3}{4}\alpha S_c^4} \leq 1. \tag{74}$$

For load case 2 with $\bar{\gamma} > 0$ and $\beta = 0$, the failure criteria reduce to:

$$e_f = \left(\frac{\sigma_{aa}}{X_t} \right)^2 \leq 1, \qquad e_m = 0, \qquad e_d = \left(\frac{\sigma_{bb}}{2S_c} \right)^2 + \left(\frac{Y_c^2}{4S_c^2} - 1 \right) \frac{\sigma_{bb}}{Y_c} \leq 1, \tag{75}$$

such that fiber breakage occurs when $\sigma_{aa} > X_t$ and matrix crushing occurs when $\sigma_{bb} < -Y_c$. Conversely, if load case 2 is specified with $\bar{\gamma} < 0$ and $\beta = 0$:

$$e_f = 0, \qquad e_m = \left(\frac{\sigma_{bb}}{Y_t}\right)^2 \leq 1, \qquad e_d = 0, \tag{76}$$

then matrix cracking occurs when $\sigma_{bb} > Y_t$. Matrix crushing is assumed to be precluded for $\sigma_{bb} > 0$.

For load case 3 with $\beta = 0$, all three criteria coincide:

$$e_f = e_m = e_d = \frac{\frac{\sigma_{ab}^2}{2\mu_{ab}} + \frac{3}{4}\alpha\sigma_{ab}^4}{\frac{S_c^2}{2\mu_{ab}} + \frac{3}{4}\alpha S_c^4} \leq 1, \tag{77}$$

such that simultaneous failure due to fiber breakage, matrix cracking, and matrix crushing occurs when $|\sigma_{ab}| > S_c$. Finally, for load case 2 with the specialized parameters $\beta = \pi/6$, $\bar{\gamma} = -1$, $S_c = 1$, $Y_t = -1$, $X_t = Y_c = 2$, it may be shown that failure is initiated via matrix cracking at time $t_0 = 0.5$.

Table 75: Material parameterization for the model 22 & 41 failure tests

Parameter	Value
Elastic modulus, E	1.0
Poisson's ratio, ν	0.0
Nonlinear shear stress parameter, α	0.0

Failure at a time of $t = 0.5$ may be obtained using the generic material parameterization given in table 75 and the following prescribed values for X_t (the tensile strength of the fibers), Y_t (the tensile strength of the matrix), Y_c (the compressive strength of the matrix), and S_c (the shear strength of the matrix), enumerated in table 76:

Table 76: Failure Tests for Models 22 and 41

Test	load case	$\bar{\gamma}$	X_t	Y_t	Y_c	S_c	Failure Mode
1	2	+0.1	0.05	1	1	1	Fiber rupture
2	2	+0.1	1	1	0.05	1	Matrix crushing
3	2	-0.1	1	0.05	1	1	Matrix cracking
4	2	+0.1	1	1	-0.05	1	Matrix crushing
5	3	+0.1	1	1	1	0.05	(All)
6	2	-0.1	1	-0.05	1	1	Matrix cracking

The results for each the tests identified in table 76 are summarized in tables 77-86 and figures 46-55. In most cases, the resulting behaviors of models 22 and 41 differ slightly, and separate reference solutions are used to verify each model separately. The relevant differences under the prescribed loading conditions are noted qualitatively in such cases.

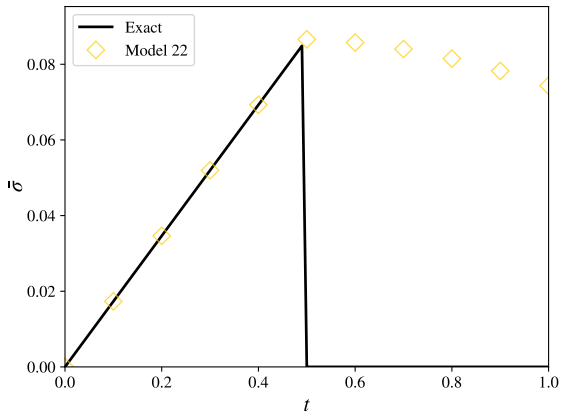

(a) Time-history plot of $\bar{\sigma}$ vs. t using $\Delta t = 0.1$.

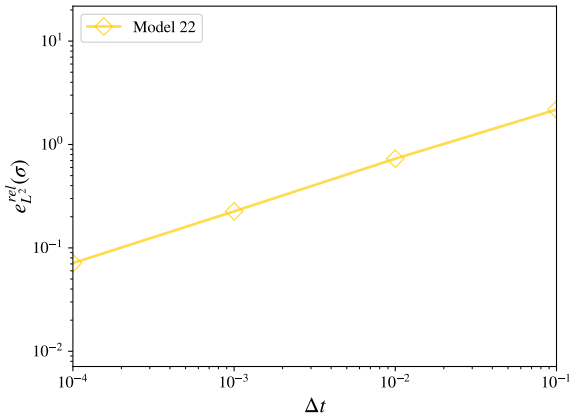

(b) Convergence plot for $e^{\text{rel}}_{L^2}(\boldsymbol{\sigma})$ errors vs. Δt.

Figure 46: Model 22 failure test 1.

Table 77: Computed errors for model 22 failure test 1.

Model	$e^{\text{rel}}_{L^2}(\boldsymbol{\sigma})$	r	$e^{\text{abs}}_{L^2}(\varepsilon_{33})$	r	$e^{\text{abs}}_{L^2}(\bar{\varepsilon}^p)$	r	Status
22	7.124e-02	0.37	0.000e+00	-	0.000e+00	-	✓

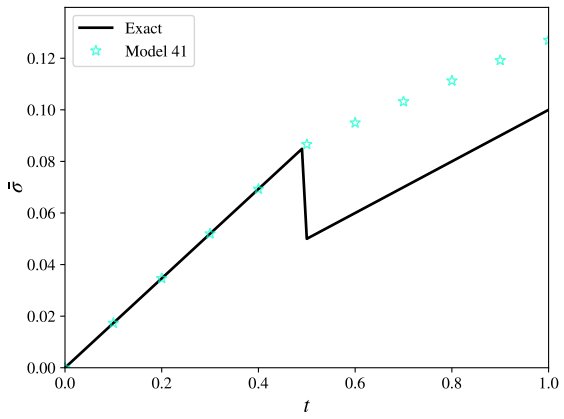

(a) Time-history plot of $\bar{\sigma}$ vs. t using $\Delta t = 0.1$.

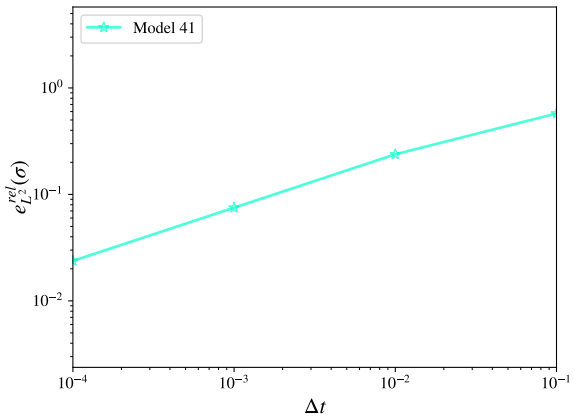

(b) Convergence plot for $e^{\text{rel}}_{L^2}(\boldsymbol{\sigma})$ errors vs. Δt.

Figure 47: Model 41 failure test 1.

Table 78: Computed errors for model 41 failure test 1.

Model	$e^{\text{rel}}_{L^2}(\boldsymbol{\sigma})$	r	$e^{\text{abs}}_{L^2}(\varepsilon_{33})$	r	$e^{\text{abs}}_{L^2}(\bar{\varepsilon}^p)$	r	Status
41	2.374e-02	0.37	0.000e+00	-	0.000e+00	-	✓

In failure test 1: following the initiation of fiber rupture for model 41, σ_{aa} and σ_{ab} are reduced to zero while σ_{aa} continues to evolve. In contrast, model 22 reduces all in-plane stress components to zero following the initiation of fiber rupture, and the element is ultimately deleted.

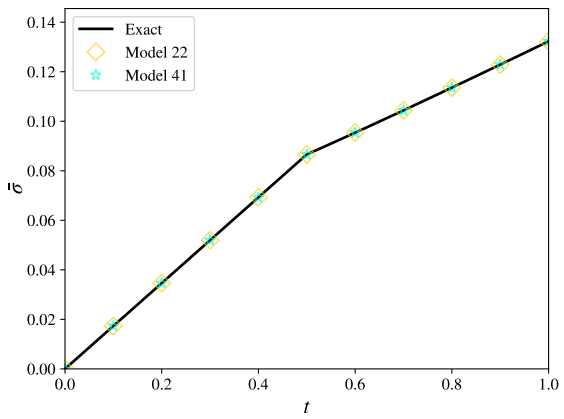

(a) Time-history plot of $\bar{\sigma}$ vs. t using $\Delta t = 0.1$.

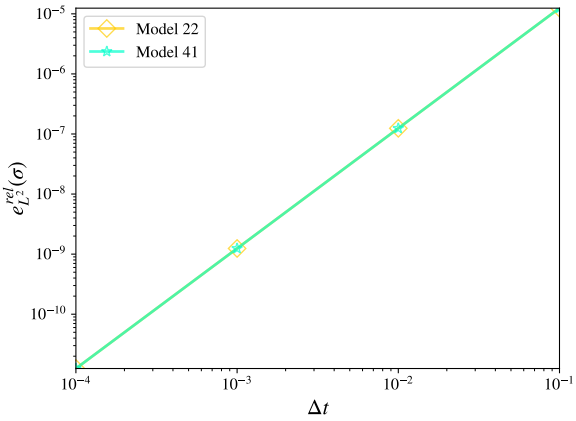

(b) Convergence plot for $e_{L^2}^{\text{rel}}(\boldsymbol{\sigma})$ errors vs. Δt.

Figure 48: Model 22 and 41 failure test 2.

Table 79: Computed errors for model 22 and 41 failure test 2.

Model	$e_{L^2}^{\text{rel}}(\boldsymbol{\sigma})$	r	$e_{L^2}^{\text{abs}}(\varepsilon_{33})$	r	$e_{L^2}^{\text{abs}}(\bar{\varepsilon}^p)$	r	Status
22	1.247e-11	2.00	0.000e+00	-	0.000e+00	-	✓
41	1.247e-11	2.00	0.000e+00	-	0.000e+00	-	✓

In failure test 2: following the initiation of matrix crushing with $Y_c > 0$, σ_{bb} and σ_{ab} are frozen while σ_{aa} continues to evolve. Both models 22 and 41 yield identical results.

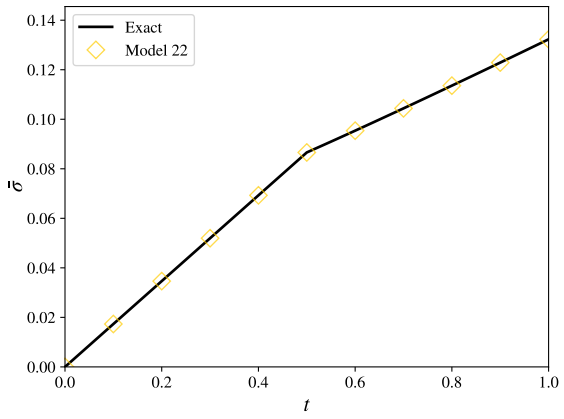

(a) Time-history plot of $\bar{\sigma}$ vs. t using $\Delta t = 0.1$.

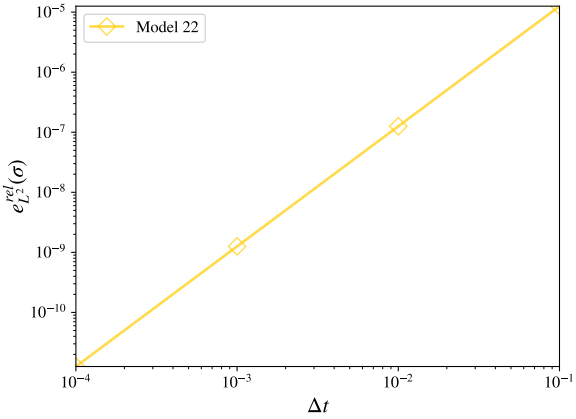

(b) Convergence plot for $e^{\text{rel}}_{L^2}(\boldsymbol{\sigma})$ errors vs. Δt.

Figure 49: Model 22 failure test 3.

Table 80: Computed errors for model 22 failure test 3.

Model	$e^{\text{rel}}_{L^2}(\boldsymbol{\sigma})$	r	$e^{\text{abs}}_{L^2}(\varepsilon_{33})$	r	$e^{\text{abs}}_{L^2}(\bar{\varepsilon}^p)$	r	Status
22	1.257e-11	2.00	0.000e+00	-	0.000e+00	-	✓

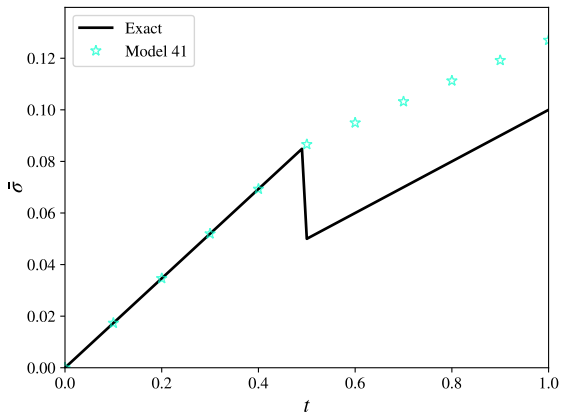

(a) Time-history plot of $\bar{\sigma}$ vs. t using $\Delta t = 0.1$.

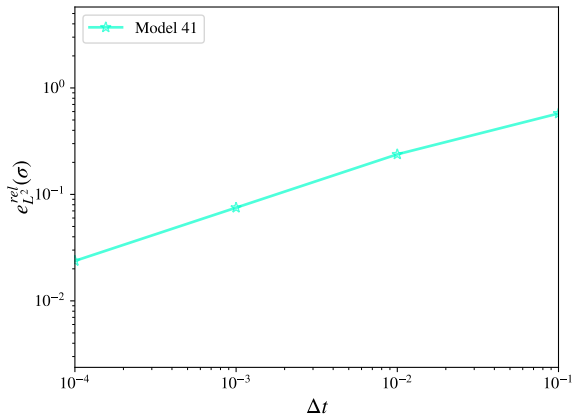

(b) Convergence plot for $e^{\text{rel}}_{L^2}(\boldsymbol{\sigma})$ errors vs. Δt.

Figure 50: Model 41 failure test 3.

Table 81: Computed errors for model 41 failure test 3.

Model	$e^{\text{rel}}_{L^2}(\boldsymbol{\sigma})$	r	$e^{\text{abs}}_{L^2}(\varepsilon_{33})$	r	$e^{\text{abs}}_{L^2}(\bar{\varepsilon}^p)$	r	Status
41	2.374e-02	0.37	0.000e+00	-	0.000e+00	-	✓

In failure test 3: following the initiation of matrix cracking with $Y_t > 0$, σ_{bb} and σ_{ab} are frozen by model 22, or reduced to zero by model 41. In either model, σ_{aa} continues to evolve.

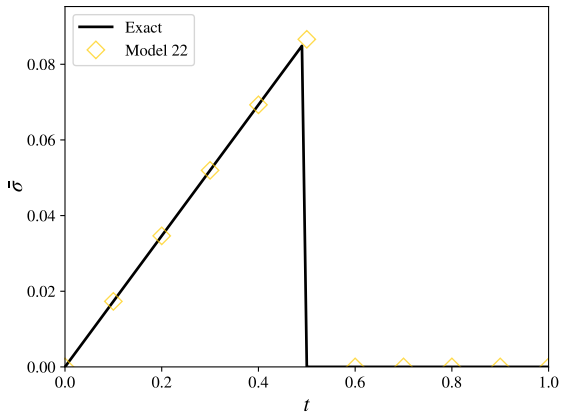

(a) Time-history plot of $\bar{\sigma}$ vs. t using $\Delta t = 0.1$.

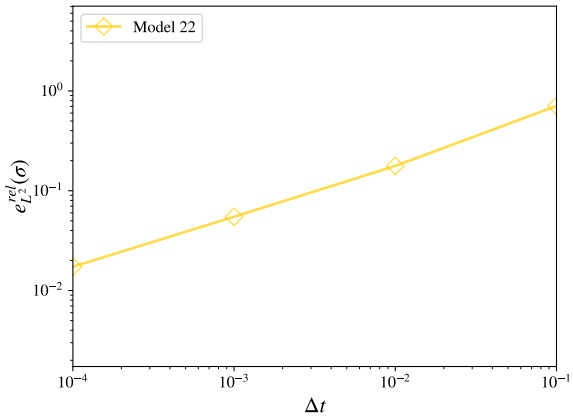

(b) Convergence plot for $e^{\text{rel}}_{L^2}(\boldsymbol{\sigma})$ errors vs. Δt.

Figure 51: Model 22 failure test 4.

Table 82: Computed errors for model 22 failure test 4.

Model	$e^{\text{rel}}_{L^2}(\boldsymbol{\sigma})$	r	$e^{\text{abs}}_{L^2}(\varepsilon_{33})$	r	$e^{\text{abs}}_{L^2}(\bar{\varepsilon}^p)$	r	Status
22	1.732e-02	0.50	0.000e+00	-	0.000e+00	-	✓

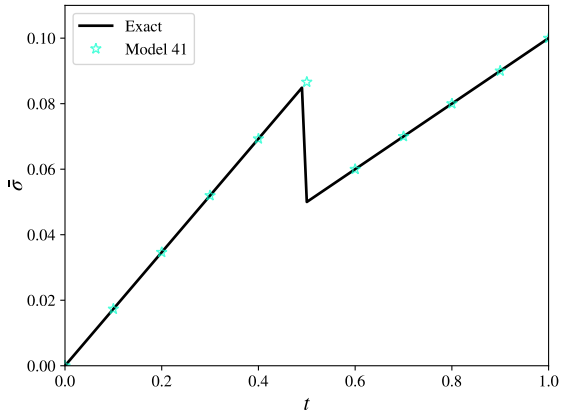

(a) Time-history plot of $\bar{\sigma}$ vs. t using $\Delta t = 0.1$.

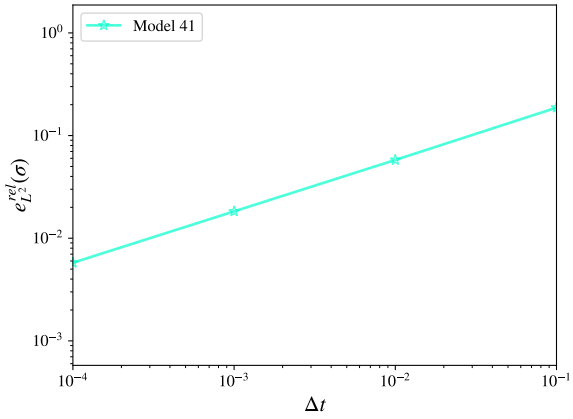

(b) Convergence plot for $e^{\text{rel}}_{L^2}(\boldsymbol{\sigma})$ errors vs. Δt.

Figure 52: Model 41 failure test 4.

Table 83: Computed errors for model 41 failure test 4.

Model	$e^{\text{rel}}_{L^2}(\boldsymbol{\sigma})$	r	$e^{\text{abs}}_{L^2}(\varepsilon_{33})$	r	$e^{\text{abs}}_{L^2}(\bar{\varepsilon}^p)$	r	Status
41	5.774e-03	0.50	0.000e+00	-	0.000e+00	-	✓

In failure test 4: following the initiation of matrix crushing for model 41 with $Y_c < 0$, σ_{aa} and σ_{ab} are reduced to zero while σ_{aa} continues to evolve. In contrast, model 22 reduces all in-plane stress components to zero following the initiation of matrix crushing if $Y_c < 0$, and the element is ultimately deleted.

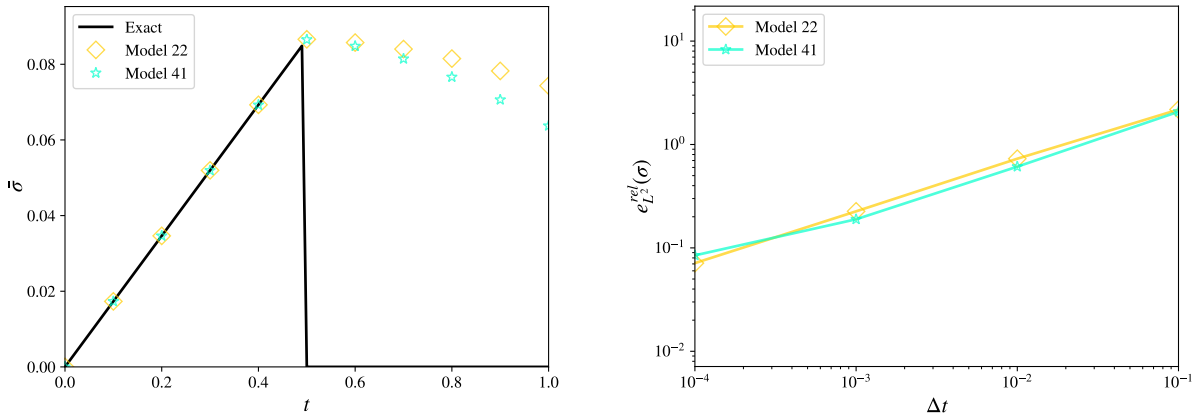

(a) Time-history plot of $\bar{\sigma}$ vs. t using $\Delta t = 0.1$.

(b) Convergence plot for $e_{L^2}^{\text{rel}}(\boldsymbol{\sigma})$ errors vs. Δt.

Figure 53: Model 22 and 41 failure test 5.

Table 84: Computed errors for model 22 and 41 failure test 5.

Model	$e_{L^2}^{\text{rel}}(\boldsymbol{\sigma})$	r	$e_{L^2}^{\text{abs}}(\varepsilon_{33})$	r	$e_{L^2}^{\text{abs}}(\bar{\varepsilon}^p)$	r	Status
22	7.124e-02	0.37	0.000e+00	-	0.000e+00	-	✓
41	8.466e-02	0.35	0.000e+00	-	0.000e+00	-	✓

In failure test 5: when fiber rupture is detected by model 22, all in-plane stress components are reduced to zero and the element is deleted, regardless of whether matrix cracking/crushing occurs. For model 41, it is only when both fiber rupture and matrix cracking are detected that all in-plane stress components are reduced to zero and the element is ultimately deleted.

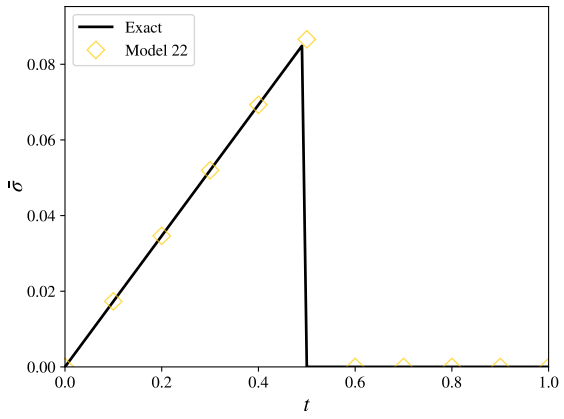

(a) Time-history plot of $\bar{\sigma}$ vs. t using $\Delta t = 0.1$.

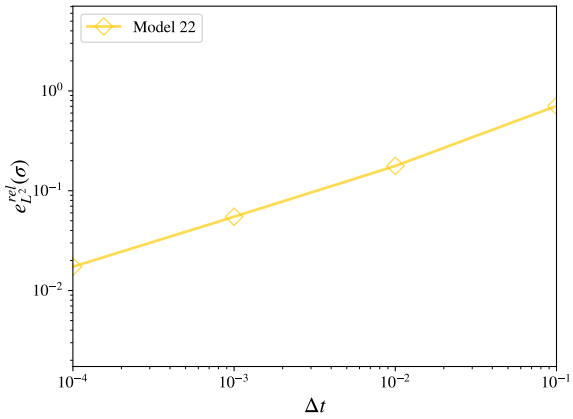

(b) Convergence plot for $e^{\text{rel}}_{L^2}(\boldsymbol{\sigma})$ errors vs. Δt.

Figure 54: Model 22 failure test 6.

Table 85: Computed errors for model 22 failure test 6.

Model	$e^{\text{rel}}_{L^2}(\boldsymbol{\sigma})$	r	$e^{\text{abs}}_{L^2}(\varepsilon_{33})$	r	$e^{\text{abs}}_{L^2}(\bar{\varepsilon}^p)$	r	Status
22	1.732e-02	0.50	0.000e+00	-	0.000e+00	-	✓

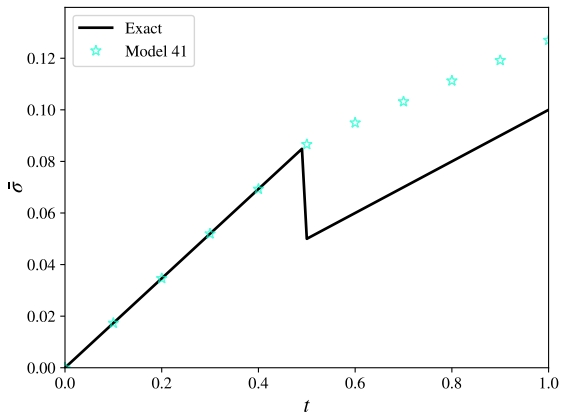

(a) Time-history plot of $\bar{\sigma}$ vs. t using $\Delta t = 0.1$.

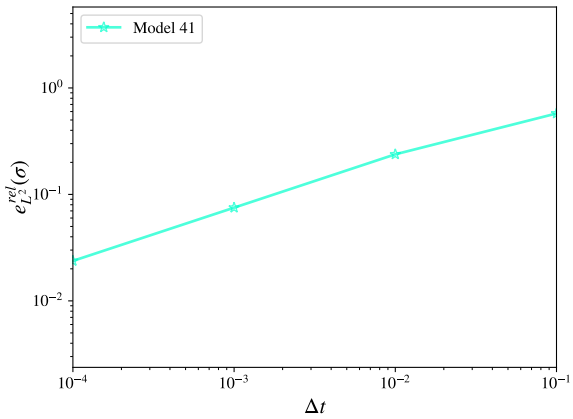

(b) Convergence plot for $e^{\text{rel}}_{L^2}(\boldsymbol{\sigma})$ errors vs. Δt.

Figure 55: Model 41 failure test 6.

Table 86: Computed errors for model 41 failure test 6.

Model	$e^{\text{rel}}_{L^2}(\boldsymbol{\sigma})$	r	$e^{\text{abs}}_{L^2}(\varepsilon_{33})$	r	$e^{\text{abs}}_{L^2}(\bar{\varepsilon}^p)$	r	Status
41	2.374e-02	0.37	0.000e+00	-	0.000e+00	-	✓

In failure test 6: following the initiation of matrix cracking with $Y_t < 0$, σ_{bb} and σ_{ab} are reduced to zero in both models. Additionally, model 22 degrades σ_{aa} to zero, and the element is ultimately deleted. In comparison, model 41 allows σ_{aa} to continue evolving.

4.5.6 Model 35 Forming Limit Diagram

Model 35 incorporates a pressure- and total effective strain rate-dependent forming limit diagram to determine failure of the material. At failure, both the yield stress and the hardening slope of the material are instantaneously reduced by a pre-defined scaling factor $SCLDEV$.

As an aside regarding the behavior of the pressure-dependent portion of the model: the value of normalized pressure $\hat{p}$ is defined such that

$$\hat{p} = \frac{p}{\sigma_y}, \qquad p = -\frac{1}{3}\mathrm{tr}(\boldsymbol{\sigma}). \tag{78}$$

Under the conditions of plane stress (as is the case for shell elements), and during plastic loading (i.e. $\sigma_y = \bar{\sigma}$), one may express $\hat{p}$ directly in terms of the in-plane principal stresses σ_1 and σ_2:

$$\hat{p} = -\frac{1}{3}\frac{\sigma_1 + \sigma_2}{\sqrt{\sigma_1^2 - \sigma_1\sigma_2 + \sigma_2^2}}. \tag{79}$$

Moreover, under the conditions of proportional loading, the in-plane principal plastic strains may be expressed as

$$\varepsilon_1^p = \frac{2\sigma_1 - \sigma_2}{2\bar{\sigma}}\bar{\varepsilon}^p, \qquad \varepsilon_2^p = \frac{2\sigma_2 - \sigma_1}{2\bar{\sigma}}\bar{\varepsilon}^p, \tag{80}$$

which may be used to construct a set of implicit relationships between the in-plane principal strains and the in-plane principal stresses using the isotropic elastic constitutitve relation:

$$\sigma_1 = \frac{E}{1-\nu^2}\left[\varepsilon_1 + \nu\varepsilon_2 - \frac{(2-\nu)\sigma_1 + (2\nu-1)\sigma_2}{2\bar{\sigma}}\bar{\varepsilon}^p\right], \tag{81}$$

$$\sigma_2 = \frac{E}{1-\nu^2}\left[\varepsilon_2 + \nu\varepsilon_1 - \frac{(2-\nu)\sigma_2 + (2\nu-1)\sigma_1}{2\bar{\sigma}}\bar{\varepsilon}^p\right]. \tag{82}$$

On a fixed strain path with $\varepsilon_2 = R\,\varepsilon_1$ for some constant strain ratio $R \in \left[-\frac{1}{2}, +1\right]$, and under the assumption of incompressible elasticity with $\nu = \frac{1}{2}$ (a reasonable simplification if the plastic strains are large in relation to the total strains), it can be deduced from the above that

$$\hat{p}(R) = \frac{-1}{\sqrt{3}}\frac{1+R}{\sqrt{1+R+R^2}}. \tag{83}$$

From the preceeding expression, it follows that $\hat{p}(-\frac{1}{2}) = -\frac{1}{3}$ (for uniaxial tension), $\hat{p}(+1) = -\frac{2}{3}$ (for bi-axial tension), and $\hat{p}(0) = -\frac{1}{\sqrt{3}}$ (for uniaxial extension).

The implementation of model 35 in DYNA3D employs a representation for the baseline pressure $\hat{p}_{\mathrm{off}}(R)$ under plane stress conditions which takes the following (quadratic) form:

$$\hat{p}_{\mathrm{off}}(R) = \frac{1}{9}\left[(6\sqrt{3}-8)R^2 - (3\sqrt{3}-2)R - 3\sqrt{3}\right], \tag{84}$$

where the excess pressure $\Delta\hat{p}$ contributing to a pressure-dependent re-scaling of the FLD envelope is computed as $\Delta\hat{p} = \hat{p} - \hat{p}_{\mathrm{off}}(R)$. It may be noted from the above that that $\hat{p}_{\mathrm{off}}(-\frac{1}{2}) = -\frac{1}{3}$, $\hat{p}_{\mathrm{off}}(+1) = -\frac{2}{3}$, and $\hat{p}_{\mathrm{off}}(0) = -\frac{1}{\sqrt{3}}$. It is herein assumed that the implemented quadratic expression in equation (84) is intended as an approximation to the expression given by equation (83).

For shell elements utilizing the parameterized load cases discussed in section 3.1, it may be shown that the smallest possible value of R_{mm} that can be theoretically attained under elastic loading conditions occurs when

$$\frac{\bar{\gamma}}{\bar{\epsilon}} = \frac{1+\nu}{1-\nu}, \tag{85}$$

which yields $R_{mm} = -\nu$. For the particular case where $\nu = 0.2$, $R_{mm} = -0.2$ is obtained when $\bar{\gamma} = 1.5\bar{\epsilon}$, and $R_{mm} = +1.0$ is obtained when $\bar{\gamma} = 0$, where it is assumed that $\bar{\epsilon} > 0$ under monotonic elastic loading conditions. These conditions are exploited to test failure via the left- and right-hand sides of the FLD envelope, respectively.

For all subsequently defined tests, the generic material parameterization given in table 87 is employed, with all supplementary loading and material parameters defined in tables 88, 89, and 90.

Table 87: Material parameterization for the model 35 failure tests

Parameter	Value
Elastic modulus, E	2.4
Poisson's ratio, ν	0.2
Yield stress, σ_0	1.0
Failure scale factor for deviatoric stresses, $SCLDEV$	0.5
Tangent modulus, E_T	0.8
Load curve for left-hand side of FLD, $LCLH$	$\{(-0.5, 0.1), (0.0, 0.11)\}$
Load curve for right-hand side of FLD, $LCRH$	$\{(0.0, 0.11), (1.0, 0.055)\}$

Table 88: Additional material parameters for the model 35 failure test 5

Parameter	Value
Load curve giving rate dependence of FLD, $LCEDF$	$\{(0.0, 0.0), (1.0, 0.5)\}$

Table 89: Additional material parameters for the model 35 failure test 6

Parameter	Value
Load curve giving pressure dependence of FLD, $LCPX$	$\{(-1.0, -0.5), (1.0, 0.5)\}$

Table 90: Failure Tests for Model 35

Test	σ_0	$IFLD$	$EMODE$	$\bar{\epsilon}$	$\bar{\gamma}$	$\varepsilon_{maj}(t_f)$	t_f
1	1.0	1	1	0.2	0.3	0.55/5.2	1.1/5.2
2	1.0	1	1	0.2	0.0	0.055	0.275
3	0.05	2	0	0.2	0.0	0.055	0.275
4	0.05	3	0	0.2	0.0	0.055	3.47/6
5	1.0	1	1	0.2	0.2	0.11	≈ 0.65688
6	1.0	1	1	0.2	0.2	0.11	≈ 0.66446

The quantitative results of each test are summarized in tables 91-96 and figures 56-61, verifying the correct behavior of all available FLD features.

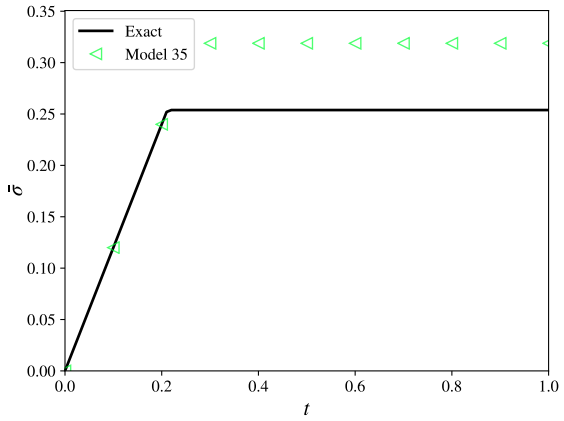

(a) Time-history plot of $\bar{\sigma}$ vs. t using $\Delta t = 0.1$.

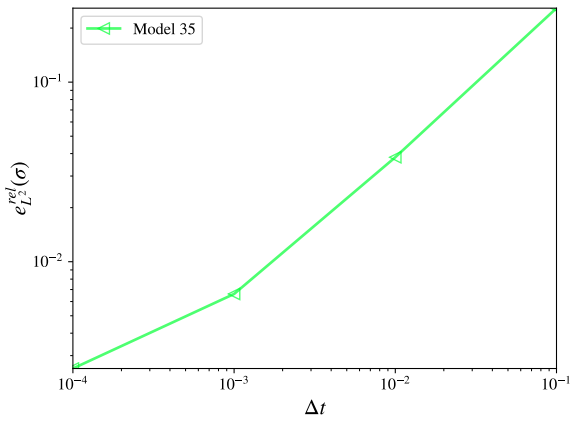

(b) Convergence plot for $e^{\text{rel}}_{L^2}(\boldsymbol{\sigma})$ errors vs. Δt.

Figure 56: Model 35 failure test 1.

Table 91: Computed errors for model 35 failure test 1.

Model	$e^{\text{rel}}_{L^2}(\boldsymbol{\sigma})$	r	$e^{\text{rel}}_{L^2}(\varepsilon_{33})$	r	$e^{\text{abs}}_{L^2}(\bar{\varepsilon}^p)$	r	Status
35	2.543e-03	0.42	2.543e-03	0.42	0.000e+00	-	✓

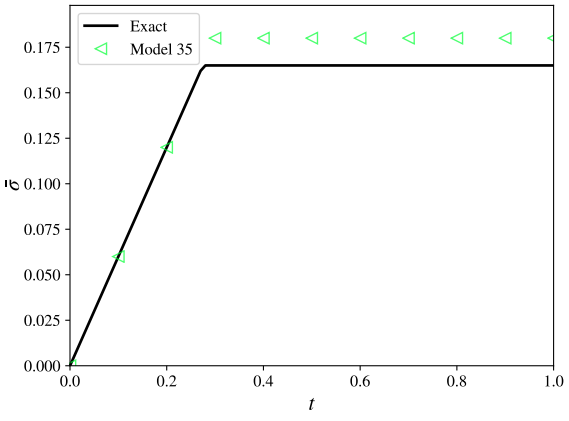

(a) Time-history plot of $\bar{\sigma}$ vs. t using $\Delta t = 0.1$.

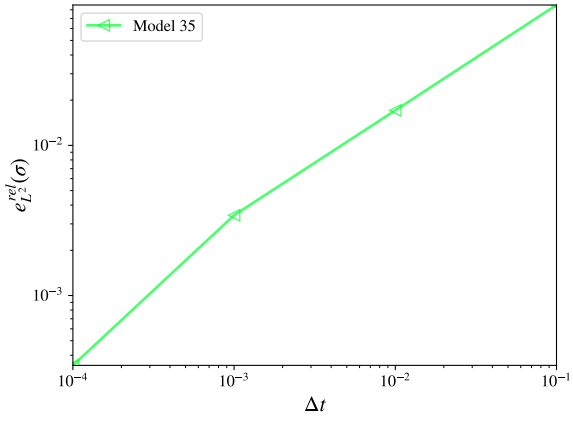

(b) Convergence plot for $e^{\text{rel}}_{L^2}(\boldsymbol{\sigma})$ errors vs. Δt.

Figure 57: Model 35 failure test 2.

Table 92: Computed errors for model 35 failure test 2.

Model	$e^{\text{rel}}_{L^2}(\boldsymbol{\sigma})$	r	$e^{\text{rel}}_{L^2}(\varepsilon_{33})$	r	$e^{\text{abs}}_{L^2}(\bar{\varepsilon}^p)$	r	Status
35	3.426e-04	0.70	3.426e-04	0.70	0.000e+00	-	✓

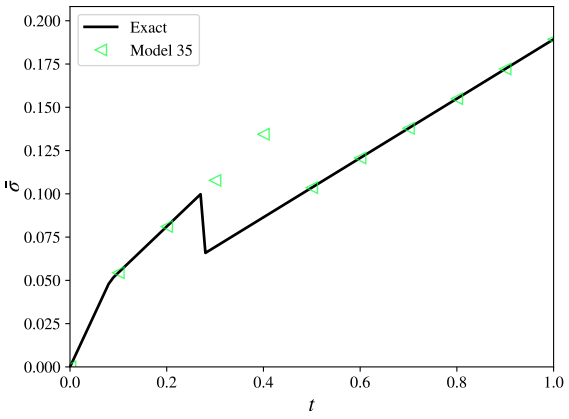

(a) Time-history plot of $\bar{\sigma}$ vs. t using $\Delta t = 0.1$.

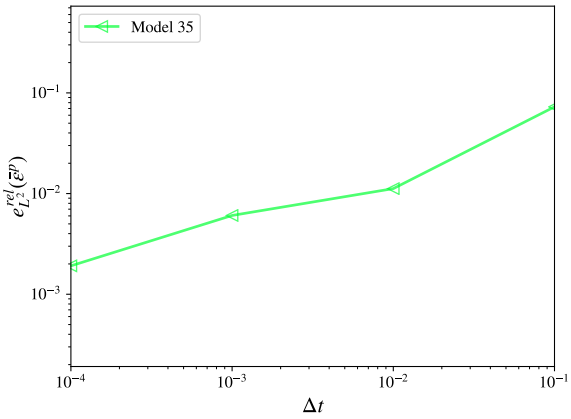

(b) Convergence plot for $e^{\text{rel}}_{L^2}(\boldsymbol{\sigma})$ errors vs. Δt.

Figure 58: Model 35 failure test 3.

Table 93: Computed errors for model 35 failure test 3.

Model	$e^{\text{rel}}_{L^2}(\boldsymbol{\sigma})$	r	$e^{\text{rel}}_{L^2}(\varepsilon_{33})$	r	$e^{\text{rel}}_{L^2}(\bar{\varepsilon}^p)$	r	Status
35	3.757e-03	0.27	1.278e-03	0.27	1.915e-03	0.27	✓

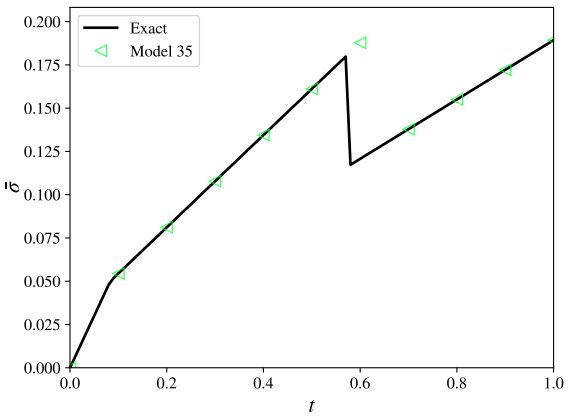

(a) Time-history plot of $\bar{\sigma}$ vs. t using $\Delta t = 0.1$.

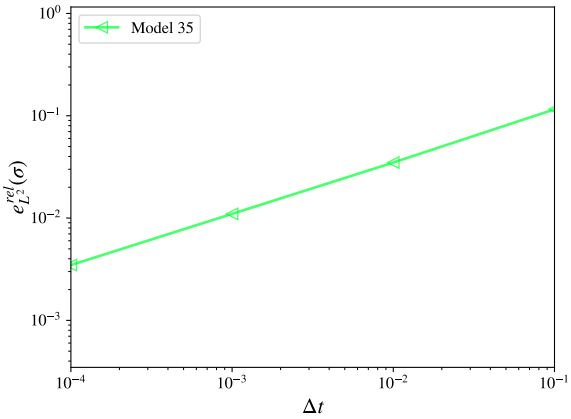

(b) Convergence plot for $e^{\text{rel}}_{L^2}(\boldsymbol{\sigma})$ errors vs. Δt.

Figure 59: Model 35 failure test 4.

Table 94: Computed errors for model 35 failure test 4.

Model	$e^{\text{rel}}_{L^2}(\boldsymbol{\sigma})$	r	$e^{\text{rel}}_{L^2}(\varepsilon_{33})$	r	$e^{\text{rel}}_{L^2}(\bar{\varepsilon}^p)$	r	Status
35	3.473e-03	0.50	1.369e-03	0.50	2.078e-03	0.50	✓

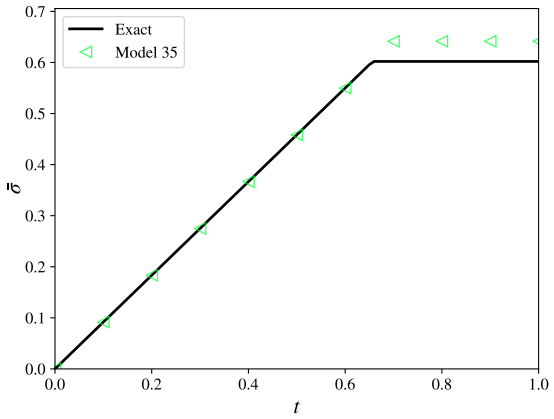

(a) Time-history plot of $\bar{\sigma}$ vs. t using $\Delta t = 0.1$.

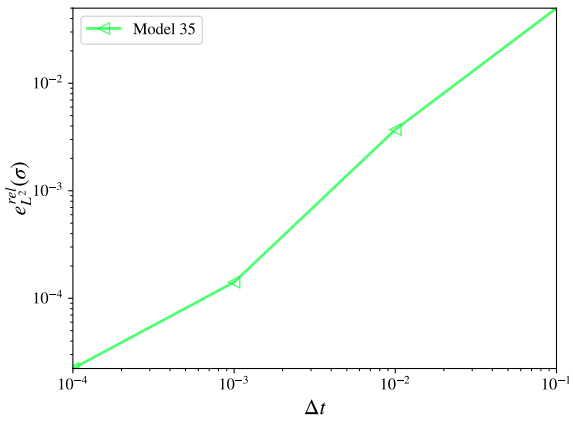

(b) Convergence plot for $e^{\text{rel}}_{L^2}(\boldsymbol{\sigma})$ errors vs. Δt.

Figure 60: Model 35 failure test 5.

Table 95: Computed errors for model 35 failure test 5.

Model	$e^{\text{rel}}_{L^2}(\boldsymbol{\sigma})$	r	$e^{\text{rel}}_{L^2}(\varepsilon_{33})$	r	$e^{\text{abs}}_{L^2}(\bar{\varepsilon}^p)$	r	Status
35	2.223e-05	0.80	2.223e-05	0.80	0.000e+00	-	✓

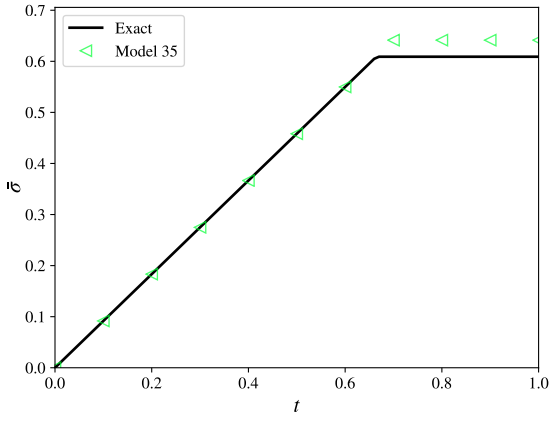

(a) Time-history plot of $\bar{\sigma}$ vs. t using $\Delta t = 0.1$.

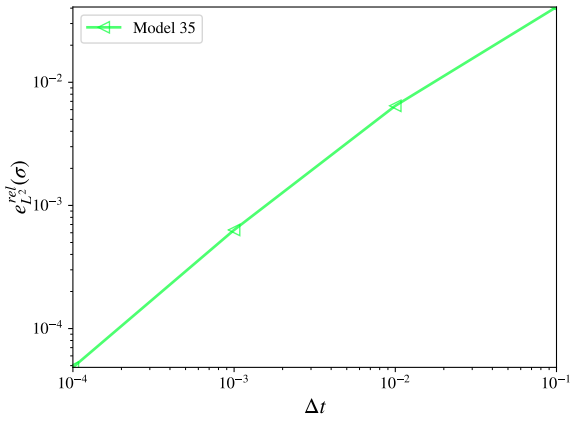

(b) Convergence plot for $e^{\text{rel}}_{L^2}(\boldsymbol{\sigma})$ errors vs. Δt.

Figure 61: Model 35 failure test 6.

Table 96: Computed errors for model 35 failure test 6.

Model	$e^{\text{rel}}_{L^2}(\boldsymbol{\sigma})$	r	$e^{\text{rel}}_{L^2}(\varepsilon_{33})$	r	$e^{\text{abs}}_{L^2}(\bar{\varepsilon}^p)$	r	Status
35	4.841e-05	0.80	4.841e-05	0.80	0.000e+00	-	✓

As an aside regarding the implicit assumptions made by model 35: according to [4], only the in-plane strains are considered when computing the value of R_{mm} for shell elements, such that the thickness strain and transverse shear strains do not bear upon the computation of the strain ratio. This ultimately leads to different ranges for R_{mm} as lying between -1 and $+1$, rather than between -0.5 and $+1.0$ (as is truly the case for solid elements). Consequently, the strain ratio ranges should potentially be reconsidered for shell elements.

Additionally: $IFLD = 2$ (incremental FLD) and $IFLD = 3$ (damage FLD) utilize the deviatoric/plastic strain increment to determine the in-plane strain ratio. Moreover, $IFLD = 3$ only accumulates "damage" during plastic loading. Given the inconsistent behavior which may result from this particular choice, it is advised that only the total FLD option ($IFLD = 1$) be utilized in practice; the remaining options should be deprecated.

4.5.7 Model 39 Damage

In addition to the plasticity features discussed in section 4.4, the Sandia damage model 39 possesses a damage variable $D \in [0, 0.99]$ whose evolution is motivated by the Cocks-Ashby solution for the growth of a spherical void in a rate-dependent plastic material model. The resulting damage-based degradation of the yield surface arises as:

$$f_y = \bar{\sigma} - (1 - D)\,\sigma_y(T, \bar{\varepsilon}^p, \dot{\bar{\varepsilon}}) \leq 0. \tag{86}$$

It is remarked that reference [1] contains a typographical error in equation (4) presented therein: the degradation factor $(1 - D)$ should additionally be applied to the hardening term κ. The above representation of the degraded flow stress in equation (86) is consistent with the model's described implementation later on in reference [1], as well as its actual implementation in DYNA3D.

Noting that the Cauchy stress for model 39 assumes the form:

$$\boldsymbol{\sigma} = (1 - D)\,\boldsymbol{\sigma}^u, \quad \boldsymbol{\sigma}^u = \mathbb{C} : (\boldsymbol{\varepsilon} - \boldsymbol{\varepsilon}^p), \tag{87}$$

one discovers that the evolution of plastic strain is controlled entirely by the undamaged state of stress $\boldsymbol{\sigma}^u$, where the yield condition reduces to:

$$f_y = (1 - D) f_y^u \leq 0, \qquad f_y^u = \bar{\sigma}^u - \sigma_y, \qquad \bar{\sigma}^u = \frac{\bar{\sigma}}{(1 - D)}, \tag{88}$$

and the consistency condition during continuous plastic loading implies:

$$\dot{f}_y = (1 - D)\dot{f}_y^u - \dot{D} f_y^u = 0 \quad \Rightarrow \quad f_y^u = 0, \quad \dot{f}_y^u = 0. \tag{89}$$

In other words, the evolution of damage is driven by the independent evolution of isochoric plastic strain via the following one-way relationship:

$$\dot{D} = \chi\left(\frac{p}{\bar{\sigma}}\right)\left[\frac{1}{(1 - D)^{\bar{m}}} - (1 - D)\right]|\dot{\boldsymbol{\varepsilon}}^p|, \qquad \chi\left(\frac{p}{\bar{\sigma}}\right) = \sinh\left(\frac{2(2\bar{m} - 1)}{(2\bar{m} + 1)}\left\langle\frac{p}{\bar{\sigma}}\right\rangle\right), \qquad |\dot{\boldsymbol{\varepsilon}}^p| = \sqrt{\dot{\boldsymbol{\varepsilon}}^p : \dot{\boldsymbol{\varepsilon}}^p}, \tag{90}$$

where the Macaulay brackets applied to the stress triaxiality $\left\langle\frac{p}{\bar{\sigma}}\right\rangle$ ensure that $\chi = 0$ under compressive loading, such that damage may only evolve under tensile loading conditions. For the special case where both $\frac{p}{\bar{\sigma}}$ and $\dot{\bar{\varepsilon}}^p$ remain constant during plastic loading, an exact solution for $D(t)$ is obtained for the above (Bernoulli) differential equation:

$$D(t) = 1 - \sqrt[\bar{m}+1]{1 + \left([1 - D_0]^{\bar{m}+1} - 1\right)\left(e^{\chi|\dot{\boldsymbol{\varepsilon}}^p|(t - t_0)}\right)^{\bar{m}+1}}, \tag{91}$$

where D_0 is the specified initial void volume fraction, and t_0 is the time of initial yielding. If $D_0 = 0$, damage is precluded such that $D(t) \equiv 0\,\forall t$.

Consider the motion given by load case 1 such that $\varepsilon_{11}(t) = \varepsilon_{22}(t) = \bar{\gamma}\,t$, $\varepsilon_{12}(t) = 0$, $\nu = 0$, and $\bar{\gamma} > 0$. These conditions yield $\bar{\sigma}(t) = \sigma_{11}(t) = \sigma_{22}(t) = (1 - D)E\left[\bar{\gamma}\,t - \frac{1}{2}\bar{\varepsilon}^p(t)\right]$, $p(t) = \frac{2}{3}\bar{\sigma}(t)$, $\varepsilon_{33}(t) = -\bar{\varepsilon}^p(t)$, and a constant loading direction $\mathbf{n}$, specifically:

$$\mathbf{n} = \begin{bmatrix} 1/2 & 0 & 0 \\ 0 & 1/2 & 0 \\ 0 & 0 & -1 \end{bmatrix}. \tag{92}$$

Consequently, the stress triaxiality $\frac{p}{\bar{\sigma}} = \frac{2}{3}$ and the effective total strain rate $\dot{\bar{\varepsilon}} = \frac{2}{3}(\bar{\gamma} + \dot{\bar{\varepsilon}}^p)$ remain constant during plastic loading, meaning that the flow stress σ_0 and the stress triaxiality factor $\chi(\frac{p}{\bar{\sigma}})$ will remain constant. Moreover, the (constant) equivalent plastic strain rate is given by

$$\dot{\bar{\varepsilon}}^p = \frac{E\,\bar{\gamma}}{E_p + \mu}, \tag{93}$$

assuming a constant linear hardening modulus of E_p. If $E_p = 0$, then $\dot{\bar{\varepsilon}} = \dot{\bar{\varepsilon}}^p = 2\bar{\gamma}$, and $\bar{\sigma} = \sigma_0$ during plastic flow. It follows that

$$\bar{\varepsilon}^p(t) = 2\bar{\gamma}\langle t - t_0 \rangle, \qquad t_0 = \frac{\sigma_0}{E\bar{\gamma}}. \tag{94}$$

The model 39 damage test utilizes load case 1 ($\bar{\gamma} = 0.5$) as described above, and the material parameterization in table 97. The results are presented in figure 62 and table 98, confirming the expected behavior of the model as described above.

Table 97: Material parameterization for the model 39 damage test.

Parameter	Value
Elastic modulus, E	2.0
Poisson's ratio, ν	0.0
Rate-independent yield stress, $Y(T)$	0.1
Damage exponent, $\bar{m}$	1.0
Initial void volume fraction, D_0	0.2

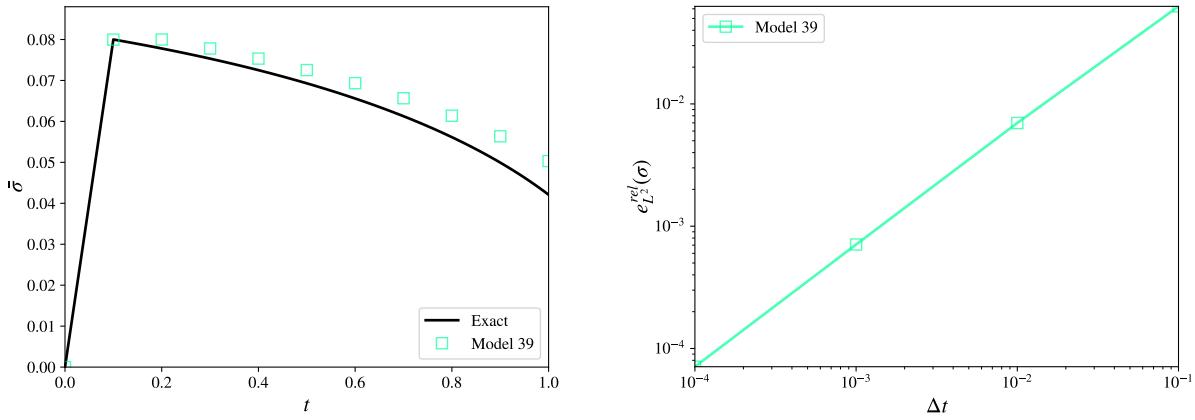

(a) Time-history plot of $\bar{\sigma}$ vs. t using $\Delta t = 0.1$.

(b) Convergence plot for $e^{\text{rel}}_{L^2}(\boldsymbol{\sigma})$ errors vs. Δt.

Figure 62: Model 39 damage test.

Table 98: Computed errors for the Sandia damage test.

Model	$e^{\text{rel}}_{L^2}(\boldsymbol{\sigma})$	r	$e^{\text{rel}}_{L^2}(\varepsilon_{33})$	r	$e^{\text{rel}}_{L^2}(\bar{\varepsilon}^p)$	r	Status
39	7.095e-05	0.95	8.062e-06	0.88	8.062e-06	0.88	✓

4.5.8 Model 50 Damage

Model 50 defines a fiber-reinforced laminated composite material with progressive damage, such that the compliance of the material is degraded according to tensile damage envelopes independently defined in the fiber and transverse directions. An additional compressive failure criterion is used to model compressive damage in the form of plastic flow.

The material possesses two orthotropic directions: a fiber direction (henceforth assumed to be aligned with the X_1 axis unless otherwise noted), and a transverse direction (aligned with the X_2 and X_3 axes – at 90° from the X_1 axis). In each such direction, the material is presumed to exhibit tension/compression asymmetry with differing failure behavior/criteria in each loading direction.

The undamaged orthotropic compliance matrix (denoted $\mathbf{C}_0^{-1}$) is expressible in terms of the specified elastic constants as:

$$\mathbf{C}_0^{-1} = \begin{bmatrix} \frac{1}{E_1} & -\frac{\nu_{12}}{E_1} & 0 & 0 & 0 & 0 \\ -\frac{\nu_{12}}{E_1} & \frac{1}{E_2} & 0 & 0 & 0 & 0 \\ 0 & 0 & \frac{1}{E_2} & 0 & 0 & 0 \\ 0 & 0 & 0 & \frac{1}{\mu_{12}} & 0 & 0 \\ 0 & 0 & 0 & 0 & \frac{1}{\mu_{23}} & 0 \\ 0 & 0 & 0 & 0 & 0 & \frac{1}{\mu_{13}} \end{bmatrix}, \tag{95}$$

where model 50 implicitly assumes that $\nu_{13} = \nu_{23} = 0$ for the purpose of decoupling the transverse thickness strain from the in-plane behavior during the stress update procedure, but otherwise assumes $\nu_{13} = \nu_{23} = \nu_{12}$ to compute the thickness strain after the in-plane stresses have been determined. This constitutes a minor discrepancy that should be addressed at a later time; for the time being, this behavior is regarded as an intentional simplification of the model, and yields the following reduced 5×5 plane stress compliance matrix (herein denoted $\bar{\mathbf{C}}_0^{-1}$):

$$\bar{\mathbf{C}}_0^{-1} = \begin{bmatrix} \frac{1}{E_1} & -\frac{\nu_{12}}{E_1} & 0 & 0 & 0 \\ -\frac{\nu_{12}}{E_1} & \frac{1}{E_2} & 0 & 0 & 0 \\ 0 & 0 & \frac{1}{\mu_{12}} & 0 & 0 \\ 0 & 0 & 0 & \frac{1}{\mu_{23}} & 0 \\ 0 & 0 & 0 & 0 & \frac{1}{\mu_{13}} \end{bmatrix}. \tag{96}$$

Tensile damage in the fiber direction is assumed to give rise to an enhanced compliance term (denoted $\bar{\mathbf{C}}_1^{-1}$) of the form:

$$\bar{\mathbf{C}}_1^{-1} = C_f \begin{bmatrix} \langle \mathrm{sign}(\varepsilon_{11}) \rangle & 0 & 0 & 0 & 0 \\ 0 & 0 & 0 & 0 & 0 \\ 0 & 0 & z & 0 & 0 \\ 0 & 0 & 0 & 0 & 0 \\ 0 & 0 & 0 & 0 & 0 \end{bmatrix}, \tag{97}$$

$$C_f = \left(d_{fib}^{ten} - 1\right) \frac{d_{o,fib}^{ten}}{E_1 \varepsilon_{fTen}}, \qquad d_{o,fib}^{ten} = \frac{2\Omega_{Ten}}{(E_1 \varepsilon_{fTen}) l_f}, \tag{98}$$

where the tensile fiber damage variable $d_{fib}^{ten} = 1$ prior to the onset of tensile damage, and is thereafter subject to the following maximum fiber-strain failure evolution condition:

$$\varepsilon_{11} \leq \left[1 + E_1 C_f (d_{fib}^{ten})\right] \left[\varepsilon_{fTen} + \left(\frac{\sigma_{SatTen}}{E_1} - \varepsilon_{fTen}\right) \min\left\{1, \max\left\{0, \frac{\max_t \varepsilon_{11}(t) - \varepsilon_{fTen}}{d_{o,fib}^{ten} - \varepsilon_{fTen}}\right\}\right\}\right], \tag{99}$$

Intuitively, the prescribed constant $d_{o,fib}^{ten}$ corresponds to the value of ε_{11} at which the saturation stress σ_{SatTen} is reached.

Additionally, tensile damage in the transverse direction yields a separate compliance enhancement term (denoted $\bar{\mathbf{C}}_2^{-1}$):

$$\bar{\mathbf{C}}_2^{-1} = C_t \, \mathbf{M}, \qquad C_t = \left(d_{tran}^{ten} - 1\right) \frac{d_{o,tran}^{ten}}{\hat{\sigma}_{fTen}}, \qquad \mathbf{M} = \begin{bmatrix} 0 & 0 & 0 & 0 & 0 \\ 0 & \langle \mathrm{sign}(\sigma_{22}) \rangle & 0 & 0 & 0 \\ 0 & 0 & D_{44} & 0 & 0 \\ 0 & 0 & 0 & D_{55} & 0 \\ 0 & 0 & 0 & 0 & 0 \end{bmatrix}, \tag{100}$$

subject to the transverse damage criterion:

$$\phi_d = \sqrt{\boldsymbol{\sigma} \cdot \mathbf{M} \cdot \boldsymbol{\sigma}} - \left[(\hat{\sigma}_{fTen} - \hat{\sigma}_{SatTen}) \exp\left(-\frac{d_{tran}^{ten}}{d_{o,tran}^{ten}} \right) + \hat{\sigma}_{SatTen} \right] \leq 0, \qquad d_{o,tran}^{ten} = \frac{2\hat{\Omega}_{Ten}}{(\hat{\sigma}_{fTen}) l_t}. \tag{101}$$

In the above, $\hat{\sigma}_{fTen}$ is the transverse tensile failure stress, $\hat{\sigma}_{SatTen}$ is the transverse tensile saturation stress, d_{tran}^{ten} is the transverse tensile damage parameter, $\hat{\Omega}_{Ten}$ is the transverse tensile damage energy, and l_t is the transverse characteristic element length.

Note: the expression given in equation (101) reflects the description of the model given in the DYNA3D manual [5]. In actuality, the behavior of the model as currently implemented in DYNA3D is given instead by the following transverse damage criterion:

$$\phi_d = \sqrt{\boldsymbol{\sigma} \cdot \mathbf{M} \cdot \boldsymbol{\sigma}} - \left[\frac{\hat{\sigma}_{fTen} - \hat{\sigma}_{SatTen}}{d_{tran}^{ten}} + \hat{\sigma}_{SatTen} \right] \leq 0, \tag{102}$$

where d_{tran}^{ten} possesses an initial value of 1 prior to failure initiation. It is advised that this inconsistency be remediated at a later time.

Collectively, the damaged plane stress material stiffness matrix $\bar{\mathbf{C}}$ is obtained via:

$$\bar{\mathbf{C}} = \left[\bar{\mathbf{C}}_0^{-1} + \bar{\mathbf{C}}_1^{-1} + \bar{\mathbf{C}}_2^{-1} \right]^{-1}. \tag{103}$$

Henceforth, the particular case where $\nu_{12} = 0$ is assumed, such that:

$$\bar{\mathbf{C}} = \begin{bmatrix} \frac{1}{E_1} + \langle \text{sign}(\varepsilon_{11}) \rangle C_f & 0 & 0 & 0 & 0 \\ 0 & \frac{1}{E_2} + \langle \text{sign}(\sigma_{22}) \rangle C_t & 0 & 0 & 0 \\ 0 & 0 & \frac{1}{\mu_{12}} + z\, C_f + D_{44}\, C_t & 0 & 0 \\ 0 & 0 & 0 & \frac{1}{\mu_{23}} + D_{55}\, C_t & 0 \\ 0 & 0 & 0 & 0 & \frac{1}{\mu_{13}} \end{bmatrix}^{-1}. \tag{104}$$

Additionally, model 50 incorporates plastic flow driven by the following form of Hill's yield criterion with power-law hardening:

$$f_y = \sqrt{\boldsymbol{\sigma} \cdot \mathbf{P} \cdot \boldsymbol{\sigma}} - G(\bar{\varepsilon}^p) \leq 0, \qquad G(\bar{\varepsilon}^p) = \sigma_0 \left(1 + \frac{\bar{\varepsilon}^p}{\varepsilon_0} \right)^n, \tag{105}$$

$$\mathbf{P} = \begin{bmatrix} \alpha & -\frac{\alpha}{2} & 0 & 0 & 0 \\ -\frac{\alpha}{2} & \delta & 0 & 0 & 0 \\ 0 & 0 & \iota\delta & 0 & 0 \\ 0 & 0 & 0 & \rho & 0 \\ 0 & 0 & 0 & 0 & \iota\delta \end{bmatrix}, \qquad \alpha = \left(\frac{G(\bar{\varepsilon}^p)}{\sigma_{y,fib}} \right)^2, \qquad \delta = \left(\frac{G(\bar{\varepsilon}^p)}{\hat{\sigma}_{y,tran}} \right)^2, \qquad \rho \approx 4. \tag{106}$$

Tensile loading in the fiber direction ultimately leads to failure being initiated by a maximum failure strain condition, i.e. when $\varepsilon_{11} = \varepsilon_{fTen}$, after which the stress evolves according to the compliance enhancement from equation (98):

$$\sigma_{11}(t) = \frac{E_1 \varepsilon_{11}(t)}{1 + E_1\, C_f(d_{fib}^{ten})}, \qquad \sigma_{12}(t) = \frac{2\mu_{12}\varepsilon_{12}(t)}{1 + \mu_{12}\, z\, C_f(d_{fib}^{ten})}, \tag{107}$$

and d_{fib}^{ten} evolves according to equation (99). This failure mode can be induced under uniaxial loading conditions (namely $\dot{\varepsilon}_{11} = 0.2$, $\dot{\varepsilon}_{22} = 0.0$) and for the material parameterization given in table 99. The quantitative results of this test are summarized in table 100 and figure 63, confirming the anticipated trilinear material response.

Table 99: Material parameterization for model 50 damage test 1

Parameter	Value
Elastic modulus, E	2.0
Poisson's ratio, ν	0.0
Fiber tensile failure strain, ε_{fTen}	0.1
Fiber tensile damage energy, Ω_{Ten}	0.03
Fiber tensile saturation stress, σ_{SatTen}	0.1

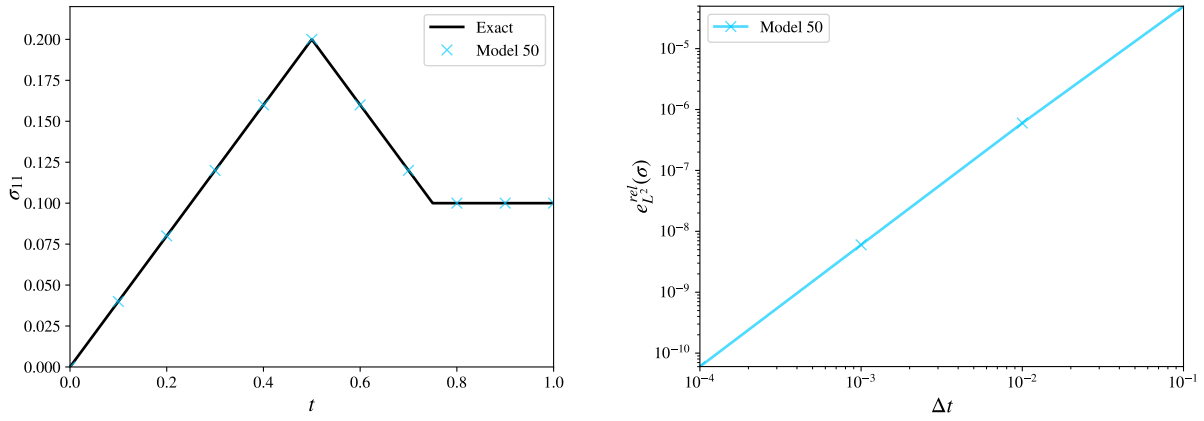

(a) Time-history plot of σ_{11} vs. t using $\Delta t = 0.1$.

(b) Convergence plot for $e_{L^2}^{\text{rel}}(\boldsymbol{\sigma})$ errors vs. Δt.

Figure 63: Model 50 damage test 1.

Table 100: Computed errors for the model 50 damage test 1.

Model	$e_{L^2}^{\text{rel}}(\boldsymbol{\sigma})$	r	$e_{L^2}^{\text{abs}}(\varepsilon_{33})$	r	$e_{L^2}^{\text{abs}}(\bar{\varepsilon}^p)$	r	Status
50	6.012e-11	1.92	0.000e+00	-	0.000e+00	-	✓

Tensile loading in the transverse direction leads to failure initiation by a maximum normal stress condition, i.e. when $\sigma_{22} = \hat{\sigma}_{fTen}$, after which the stress evolves according to the damage surface given by equation (101):

$$\varepsilon_{22}(t) = \left(\frac{1}{E_2} + \left(d_{tran}^{ten} - 1\right)\frac{d_{o,tran}^{ten}}{\hat{\sigma}_{fTen}}\right)\left[\left(\hat{\sigma}_{fTen} - \hat{\sigma}_{SatTen}\right)\exp\left(-\frac{d_{tran}^{ten}}{d_{o,tran}^{ten}}\right) + \hat{\sigma}_{SatTen}\right]. \tag{108}$$

This failure mode can be induced under uniaxial loading conditions (namely $\dot{\varepsilon}_{11} = 0.0$, $\dot{\varepsilon}_{22} = 0.2$) and for the material parameterization given in table 101. The quantitative results of this test are summarized in table 102 and figure 64, confirming the anticipated softening material response.

Table 101: Material parameterization for model 50 damage test 2

Parameter	Value
Elastic modulus, E	2.0
Poisson's ratio, ν	0.0
Transverse tensile strength, $\hat{\sigma}_{fTen}$	0.2
Transverse tensile damage energy, $\hat{\Omega}_{Ten}$	0.03
Transverse tensile saturation stress, $\hat{\sigma}_{SatTen}$	0.05

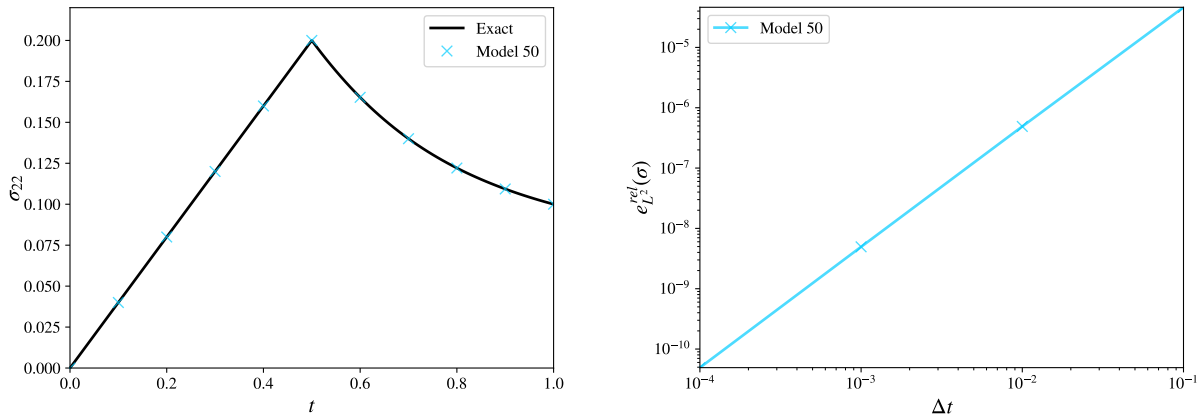

(a) Time-history plot of σ_{22} vs. t using $\Delta t = 0.1$.

(b) Convergence plot for $e_{L^2}^{\text{rel}}(\boldsymbol{\sigma})$ errors vs. Δt.

Figure 64: Model 50 damage test 2.

Table 102: Computed errors for the model 50 damage test 2.

Model	$e_{L^2}^{\text{rel}}(\boldsymbol{\sigma})$	r	$e_{L^2}^{\text{abs}}(\varepsilon_{33})$	r	$e_{L^2}^{\text{abs}}(\bar{\varepsilon}^p)$	r	Status
50	4.918e-11	1.98	0.000e+00	-	0.000e+00	-	✓

The compressive matrix damage mechanism activated during the conditions of plastic flow can be induced under compressive biaxial loading conditions (namely $\dot{\varepsilon}_{11} = -0.2$, $\dot{\varepsilon}_{22} = -0.2$) and for the material parameterization given in table 103. The quantitative results of this test are summarized in table 104 and figure 65, confirming the anticipated trilinear material response.

Table 103: Material parameterization for model 50 damage test 3

Parameter	Value
Elastic modulus, E	2.0
Poisson's ratio, ν	0.0
Yield stress, σ_0	0.2
Strain hardening exponent, n	0.0
Fiber compressive failure strain, ε_{fComp}	0.1
Fiber compressive damage energy, Ω_{Comp}	0.03
Fiber compressive saturation stress, $\sigma_{SatComp}$	0.1
Transverse compressive failure strain, $\hat{\varepsilon}_{fComp}$	0.1
Transverse compressive damage energy, $\hat{\Omega}_{Comp}$	0.03
Transverse compressive saturation stress, $\hat{\sigma}_{SatComp}$	0.1

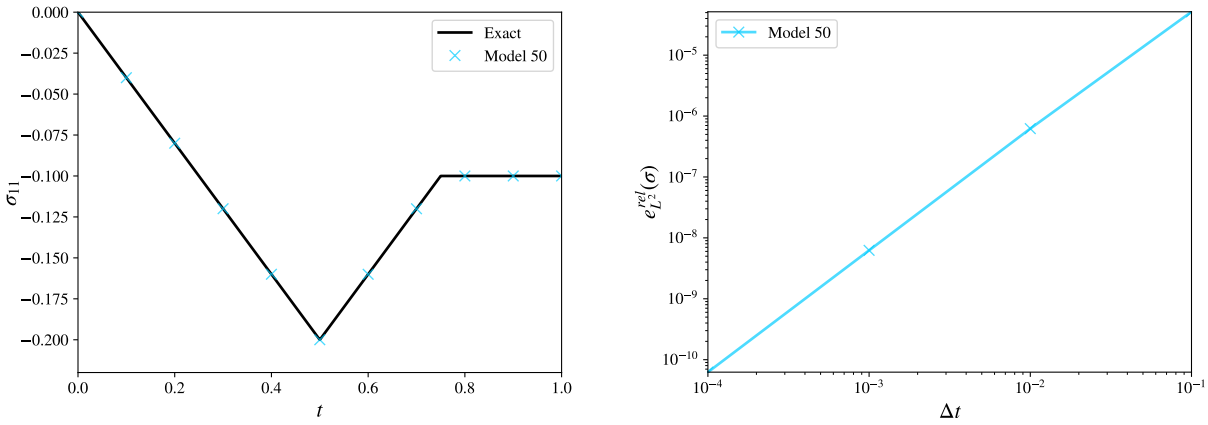

(a) Time-history plot of σ_{11} vs. t using $\Delta t = 0.1$.

(b) Convergence plot for $e^{\text{rel}}_{L^2}(\boldsymbol{\sigma})$ errors vs. Δt.

Figure 65: Model 50 damage test 3.

Table 104: Computed errors for the model 50 damage test 3.

Model	$e^{\text{rel}}_{L^2}(\boldsymbol{\sigma})$	r	$e^{\text{rel}}_{L^2}(\varepsilon_{33})$	r	$e^{\text{rel}}_{L^2}(\bar{\varepsilon}^p)$	r	Status
50	6.243e-11	1.92	1.137e-10	1.96	1.137e-10	1.96	✓

Under transverse compressive loading, the associated damage variable d_{tran}^{comp} (with an initial value of zero) evolves according to the following total effective compressive strain envelope:

$$\sqrt{\langle -\varepsilon_{22}\rangle^2 + \nu_f (2\varepsilon_{12})^2} \leq (1 + d_{tran}^{comp})\, \hat{\varepsilon}_{fComp}. \tag{109}$$

The compressive yield stress in the transverse direction (herein denoted $\hat{\sigma}_{yTran}$) is consequently degraded according to

$$\hat{\sigma}_{yTran} = (1 - \xi)\, G(\bar{\varepsilon}^p) + \xi\, \hat{\sigma}_{SatComp}, \tag{110}$$

$$\xi = \min\left\{1, \frac{d_{tran}^{comp}}{d_{o,tran}^{comp}}\right\}, \qquad d_{o,tran}^{comp} = \frac{2\hat{\Omega}_{Comp}}{\hat{\sigma}_{fComp}\hat{\varepsilon}_{fComp} l_t} - \frac{\hat{\sigma}_{fComp}}{E_2 \hat{\varepsilon}_{fComp}}. \tag{111}$$

If compressive failure is assumed to initiate in the elastic range, then $\hat{\sigma}_{fComp} = E_2 \hat{\varepsilon}_{fComp}$. Otherwise, $\hat{\sigma}_{fComp} = G(\bar{\varepsilon}^p)$ such that $\bar{\varepsilon}^p$ satisfies the following approximate relation:

$$E_2 \left[\hat{\varepsilon}_{fComp} - (\sqrt{3}\varepsilon_0)\bar{\varepsilon}^p\right] = G(\bar{\varepsilon}^p). \tag{112}$$

In the preceeding expression for $\mathbf{P}$ in equation (106), the value of the Hill yield surface parameter δ is ultimately computed as

$$\delta = \left(\frac{G(\bar{\varepsilon}^p)}{\hat{\sigma}_{yTran}}\right)^2, \tag{113}$$

starting with an initial value of $\delta = 1$ when $d_{tran}^{comp} = 0$ ($\hat{\sigma}_{yTran} = G(\bar{\varepsilon}^p)$).

In the special case where the compressive yield stress in the fiber direction (herein denoted $\hat{\sigma}_{yFib}$) far exceeds the transverse compressive yield stress, one obtains $\alpha \approx 0$ in the expression given for $\mathbf{P}$ in equation (106).

For load cases 2, 3, and 5, the effective stress may be expressed respectively as:

$$\bar{\sigma} = \sqrt{\delta}|\sigma_{22}|, \qquad \bar{\sigma} = \sqrt{\iota\delta}|\sigma_{12}|, \qquad \bar{\sigma} = \sqrt{\iota\delta}|\sigma_{13}|, \tag{114}$$

such that the corresponding plastic consistency condition in each case may be expressed as

$$\left|E_2\left(\varepsilon_{22} - \frac{G(\bar{\varepsilon}^p)}{\hat{\sigma}_{yTran}}\mathrm{sign}(\sigma_{22})\bar{\varepsilon}^p\right)\right| \leq \hat{\sigma}_{yTran}, \tag{115}$$

$$\left|\mu_{12}\left(2\varepsilon_{12} - \sqrt{\iota}\frac{G(\bar{\varepsilon}^p)}{\hat{\sigma}_{yTran}}\mathrm{sign}(\sigma_{12})\bar{\varepsilon}^p\right)\right| \leq \frac{\hat{\sigma}_{yTran}}{\sqrt{\iota}}, \tag{116}$$

$$\left|\mu_{13}\left(2\varepsilon_{13} - \sqrt{\iota}\frac{G(\bar{\varepsilon}^p)}{\hat{\sigma}_{yTran}}\mathrm{sign}(\sigma_{13})\bar{\varepsilon}^p\right)\right| \leq \frac{\hat{\sigma}_{yTran}}{\sqrt{\iota}}, \tag{117}$$

from which the time-history of the equivalent plastic strain $\bar{\varepsilon}^p$ may be determined directly from the prescribed strain history. Explicitly (assuming $\bar{\gamma} > 0$):

$$\bar{\varepsilon}^p = \frac{\hat{\sigma}_{yTran}}{E_2 G(\bar{\varepsilon}^p)}(-E_2\varepsilon_{22} - \hat{\sigma}_{yTran}) \quad \forall t > t_0, \qquad t_0 = -\frac{\sigma_0}{E_2\dot{\varepsilon}_{22}}, \tag{118}$$

$$\bar{\varepsilon}^p = \frac{\hat{\sigma}_{yTran}}{\mu_{12}\,\iota G(\bar{\varepsilon}^p)}(2\mu_{12}\sqrt{\iota}\varepsilon_{12} - \hat{\sigma}_{yTran}) \quad \forall t > t_0, \qquad t_0 = \frac{\sigma_0}{2\mu_{12}\sqrt{\iota}\dot{\varepsilon}_{12}}, \tag{119}$$

$$\bar{\varepsilon}^p = \frac{\hat{\sigma}_{yTran}}{\mu_{13}\,\iota G(\bar{\varepsilon}^p)}(2\mu_{13}\sqrt{\iota}\varepsilon_{13} - \hat{\sigma}_{yTran}) \quad \forall t > t_0, \qquad t_0 = \frac{\sigma_0}{2\mu_{13}\sqrt{\iota}\dot{\varepsilon}_{13}}. \tag{120}$$

In what follows, $G(\bar{\varepsilon}^p) = \sigma_0$ is assumed to remain constant for the sake of simplicity. This failure mode can be induced under isochoric loading conditions (namely $\dot{\varepsilon}_{11} = 0.2$, $\dot{\varepsilon}_{22} = -0.2$) and for the material parameterization given in table 105. The quantitative results of this test are summarized in table 106 and figure 66, confirming the anticipated trilinear material response.

Table 105: Material parameterization for model 50 damage test 4

Parameter	Value
Elastic modulus, E	2.0
Poisson's ratio, ν	0.0
Yield stress, σ_0	0.2
Strain hardening exponent, n	0.0
Transverse compressive failure strain, $\hat{\varepsilon}_{fComp}$	0.1
Transverse compressive damage energy, $\hat{\Omega}_{Comp}$	0.03
Transverse compressive saturation stress, $\hat{\sigma}_{SatComp}$	0.1

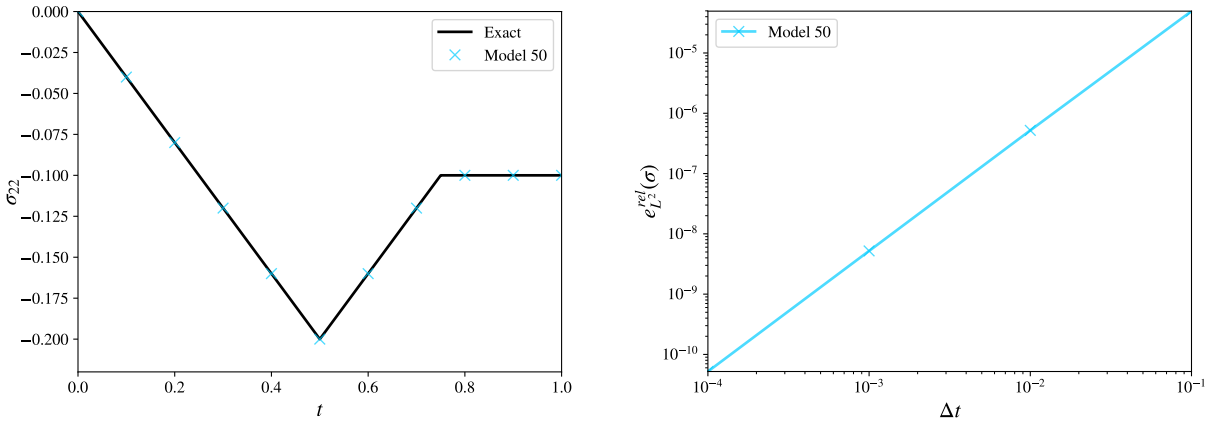

(a) Time-history plot of σ_{22} vs. t using $\Delta t = 0.1$.

(b) Convergence plot for $e_{L^2}^{\text{rel}}(\boldsymbol{\sigma})$ errors vs. Δt.

Figure 66: Model 50 damage test 4.

Table 106: Computed errors for the model 50 damage test 4.

Model	$e_{L^2}^{\text{rel}}(\boldsymbol{\sigma})$	r	$e_{L^2}^{\text{rel}}(\varepsilon_{33})$	r	$e_{L^2}^{\text{rel}}(\bar{\varepsilon}^p)$	r	Status
50	5.209e-11	1.98	1.137e-10	1.96	1.136e-10	1.96	✓

4.5.9 Model 52 Damage

Model 52 utilizes a microvoid growth-induced fracture model which checks for failure based upon an effective strain rate- and stress triaxiality-dependent maximum plastic strain condition. Once the accumulated plastic strain exceeds the current maximum value, the yield stress in the material is re-scaled by a damage-driven exponential softening function which eventually drives the yield stress to zero as damage increases.

Consider the motion given by load case 1 such that $\varepsilon_{11}(t) = \varepsilon_{22}(t) = \bar{\gamma}\, t$, $\varepsilon_{12}(t) = 0$, $\nu = 0$, and $\bar{\gamma} > 0$. These conditions yield $\bar{\sigma}(t) = \sigma_{11}(t) = \sigma_{22}(t) = E\left[\bar{\gamma}\, t - \frac{1}{2}\bar{\varepsilon}^p(t)\right]$, $\sigma_m(t) = \frac{2}{3}\bar{\sigma}(t)$, $\varepsilon_{33}(t) = -\bar{\varepsilon}^p(t)$, and a constant loading direction $\mathbf{n}$, specifically:

$$\mathbf{n} = \begin{bmatrix} 1/2 & 0 & 0 \\ 0 & 1/2 & 0 \\ 0 & 0 & -1 \end{bmatrix}. \tag{121}$$

Consequently, the stress triaxiality $\frac{\sigma_m}{\bar{\sigma}} = \frac{2}{3}$ and the effective (total) strain rate $\dot{\bar{\varepsilon}} = \frac{2}{3}(\bar{\gamma} + \dot{\bar{\varepsilon}}^p)$ remain constant during plastic loading, meaning that the fracture strain $\varepsilon_f(\dot{\bar{\varepsilon}}, \sigma_m/\bar{\sigma})$ will remain constant prior to failure. Moreover, the (constant) equivalent plastic strain rate prior to failure is given by

$$\dot{\bar{\varepsilon}}^p = \frac{E\,\bar{\gamma}}{E_p + \mu}, \tag{122}$$

assuming a constant linear hardening modulus of E_p. For the particular case where $E_p = 0$, then $\dot{\bar{\varepsilon}} = \dot{\bar{\varepsilon}}^p = 2\bar{\gamma}$, and $\bar{\sigma} = \sigma_0$ during plasticity. It follows that

$$\bar{\varepsilon}^p(t) = 2\bar{\gamma}\langle t - t_0\rangle \quad \forall t < t_f, \tag{123}$$

where $t_0 = \frac{\sigma_0}{E\bar{\gamma}}$, and t_f denotes the time at failure.

Once fracture initiates (i.e. when $\bar{\varepsilon}^p \geq \varepsilon_f$), the failure strain is held fixed as $\varepsilon_f^c = \varepsilon_f(t_f)$ at the time of failure, and the yield stress is re-scaled such that

$$\sigma_y(t) = \sigma_0 e^{A(1-\bar{\varepsilon}^p(t)/\varepsilon_f^c)} \quad \forall t \geq t_f = t_0 + \frac{\varepsilon_f^c}{2\bar{\epsilon}}. \tag{124}$$

The above constitutes an exponential softening plasticity model for valid post-fracture constant values $A > 0$, whose exact solution yields:

$$\bar{\varepsilon}^p(t) = \varepsilon_f^c + \frac{2\sigma_0}{E} + 2\bar{\epsilon}(t - t_f) + \frac{\varepsilon_f^c}{A} W\left(-\frac{A}{\varepsilon_f^c}\frac{2\sigma_0}{E}\, e^{-\frac{A}{\varepsilon_f^c}\left[\frac{2\sigma_0}{E} + 2\bar{\epsilon}(t-t_f)\right]}\right) \quad \forall t \geq t_f, \tag{125}$$

where $W(x)$ denotes the Lambert W function.

All model 52 damage tests utilize load case 1 ($\bar{\gamma} = 0.2$) and the generic material parameters given in table 107. The additional (variable) parameterizations used for each test are enumerated in table 108. The verified results of the model 52 damage tests 1-3 are presented respectively in tables 109-111, and figures 67-69.

Table 107: Material parameterization for the model 52 damage tests

Parameter	Value
Elastic modulus, E	2.0
Poisson's ratio, ν	0.0
Yield stress, σ_0	0.1
Flag for fracture, $NBRUCH$	1
Post-fracture constant, A	1.0

Table 108: Damage Tests for Model 52

Test	$\dot{\bar{\varepsilon}}$	$\sigma_m/\bar{\sigma}$	$\varepsilon_f(\dot{\bar{\varepsilon}}, \sigma_m/\bar{\sigma})$
1	$\{0.0\}$	$\{0.0\}$	$\{\{0.1\}\}$
2	$\{0.01, 1.0\}$	$\{0.0\}$	$\{\{0.1\}, \{0.2\}\}$
3	$\{0.0\}$	$\{0.0, 1.0\}$	$\{\{0.1, 0.2\}\}$

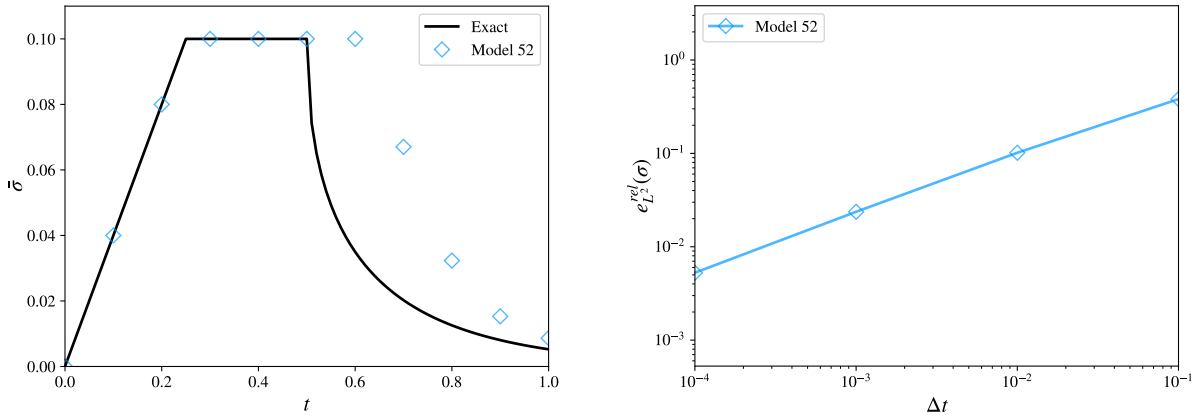

(a) Time-history plot of $\bar{\sigma}$ vs. t using $\Delta t = 0.1$.

(b) Convergence plot for $e^{\text{rel}}_{L^2}(\boldsymbol{\sigma})$ errors vs. Δt.

Figure 67: Model 52 damage test 1.

Table 109: Computed errors for model 52 damage test 1.

Model	$e^{\text{rel}}_{L^2}(\boldsymbol{\sigma})$	r	$e^{\text{rel}}_{L^2}(\varepsilon_{33})$	r	$e^{\text{rel}}_{L^2}(\bar{\varepsilon}^p)$	r	Status
52	5.270e-03	0.58	1.572e-03	0.58	1.572e-03	0.58	✓

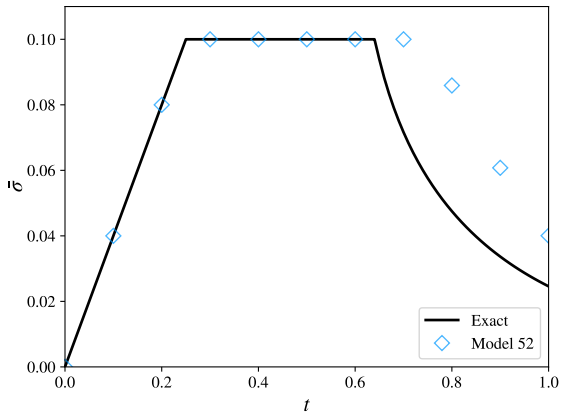

(a) Time-history plot of $\bar{\sigma}$ vs. t using $\Delta t = 0.1$.

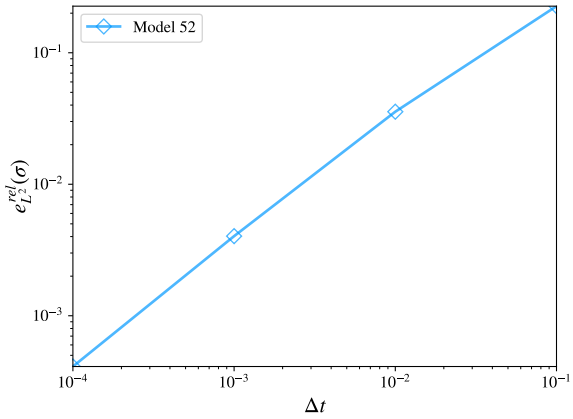

(b) Convergence plot for $e^{\text{rel}}_{L^2}(\boldsymbol{\sigma})$ errors vs. Δt.

Figure 68: Model 52 damage test 2.

Table 110: Computed errors for model 52 damage test 2.

Model	$e^{\text{rel}}_{L^2}(\boldsymbol{\sigma})$	r	$e^{\text{rel}}_{L^2}(\varepsilon_{33})$	r	$e^{\text{rel}}_{L^2}(\bar{\varepsilon}^p)$	r	Status
52	4.111e-04	0.79	1.731e-04	0.80	1.731e-04	0.80	✓

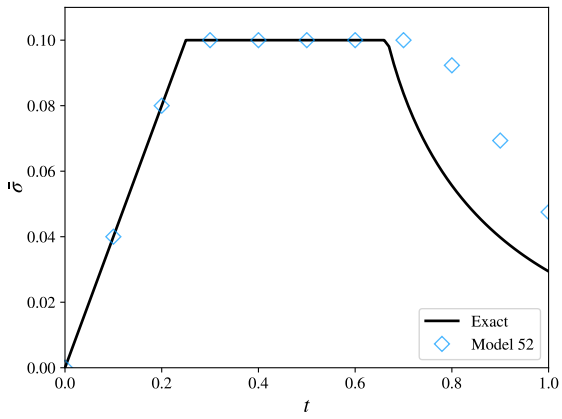

(a) Time-history plot of $\bar{\sigma}$ vs. t using $\Delta t = 0.1$.

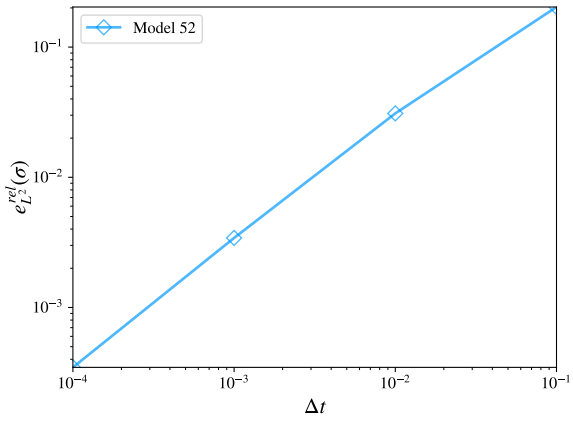

(b) Convergence plot for $e^{\text{rel}}_{L^2}(\boldsymbol{\sigma})$ errors vs. Δt.

Figure 69: Model 52 damage test 3.

Table 111: Computed errors for model 52 damage test 3.

Model	$e^{\text{rel}}_{L^2}(\boldsymbol{\sigma})$	r	$e^{\text{rel}}_{L^2}(\varepsilon_{33})$	r	$e^{\text{rel}}_{L^2}(\bar{\varepsilon}^p)$	r	Status
52	3.468e-04	0.81	1.538e-04	0.81	1.538e-04	0.81	✓

4.5.10 Model 74 Damage

Model 74 defines a laminated composite which may have fibers oriented in many different in-plane directions, resulting in a transversely isotropic material. The model includes delamination damage and in-plane damage which evolve independently according to the definition of their respective failure surfaces.

For shell elements, the damage surfaces themselves may be expressed directly in terms of the (implicitly time-varying) strain components, as

$$\phi_{delam} = \sqrt{\left(\frac{2G_{bc}\,\varepsilon_{23}(t)}{S_5}\right)^2 + \left(\frac{2G_{ca}\,\varepsilon_{13}(t)}{S_6}\right)^2} - R_{delam} \leq 0, \tag{126}$$

$$\phi_{inplane} = \sqrt{\left(\frac{\max(0,\varepsilon_1(t))}{\varepsilon_{ten}}\right)^2 + \left(\frac{\min(0,\varepsilon_2(t))}{\varepsilon_{comp}}\right)^2} - R_{inplane} \leq 0, \tag{127}$$

subject to the additional KKT conditions: $\dot{R}_{delam} \geq 0$, $\dot{R}_{delam}\phi_{delam} = 0$, $\dot{R}_{inplane} \geq 0$, $\dot{R}_{inplane}\phi_{inplane} = 0$. Under monotonic loading conditions, it suffices to express the damage variables as linear functions of time for fixed rates of loading:

$$R_{delam}(t) = \left[\left(\frac{2G_{bc}\,\dot{\varepsilon}_{23}}{S_5}\right)^2 + \left(\frac{2G_{ca}\,\dot{\varepsilon}_{13}}{S_6}\right)^2\right]^{\frac{1}{2}} t, \tag{128}$$

$$R_{inplane}(t) = \left[\left(\frac{\max(0,\dot{\varepsilon}_1)}{\varepsilon_{ten}}\right)^2 + \left(\frac{\min(0,\dot{\varepsilon}_2)}{\varepsilon_{comp}}\right)^2\right]^{\frac{1}{2}} t, \tag{129}$$

where

$$\dot{\varepsilon}_1, \dot{\varepsilon}_2 = \frac{(\dot{\varepsilon}_{11} + \dot{\varepsilon}_{22}) \pm \sqrt{(\dot{\varepsilon}_{11} - \dot{\varepsilon}_{22})^2 + 4\,\dot{\varepsilon}_{12}^2}}{2}. \tag{130}$$

Both the delamination and in-plane damage scale factors (d_{delam} and $d_{inplane}$, respectively) may assume an exponential or hyperbolic tangent form:

$$d_*(t) = \begin{cases} 0 & R_*(t) < 1 \\ 1 - \exp\left(\frac{1-R_*(t)}{F_*}\right) & R_*(t) \geq 1 \end{cases}, \tag{131}$$

or

$$d_*(t) = \frac{1}{2}\left[\tanh\left(\frac{R_*(t) - \bar{R}_*}{F_*}\right) + 1\right], \tag{132}$$

where the quantities subscripted by $*$ may pertain to either the *delam* or *inplane* damage criteria. In either case, these damage scale factors are consequently expressed as explicit functions of time for the chosen load cases.

The Cauchy stress may therefore be expressed as a direct function of time according to the degraded response for shell elements:

$$\boldsymbol{\sigma}(t) = (1 - d_{inplane}(t))\,\mathbb{C} : \{\boldsymbol{\varepsilon}(t) - d_{delam}(t)\,\boldsymbol{\varepsilon}_{delam}(t)\} + d_{inplane}(t)\,\mathbb{C}_f : \boldsymbol{\varepsilon}(t), \tag{133}$$

or, in terms of the individual stress components:

$$\begin{Bmatrix} \sigma_{11}(t) \\ \sigma_{22}(t) \\ \sigma_{33}(t) \\ \sigma_{12}(t) \\ \sigma_{23}(t) \\ \sigma_{13}(t) \end{Bmatrix} = (1 - d_{inplane}(t)) \begin{Bmatrix} \sigma^e_{11}(t) \\ \sigma^e_{22}(t) \\ 0 \\ \sigma^e_{12}(t) \\ (1 - d_{delam}(t))\,\sigma^e_{23}(t) \\ (1 - d_{delam}(t))\,\sigma^e_{13}(t) \end{Bmatrix} + d_{inplane}(t) \begin{Bmatrix} \delta_1 \bar{E}_f \varepsilon_{11}(t) \\ \delta_2 \bar{E}_f \varepsilon_{22}(t) \\ 0 \\ 2S_f \bar{G}_f \varepsilon_{12}(t) \\ 2S_f \bar{G}_f \varepsilon_{23}(t) \\ 2S_f \bar{G}_f \varepsilon_{13}(t) \end{Bmatrix}, \tag{134}$$

assuming the material axes are aligned with the global coordinate axes, where $\boldsymbol{\sigma}^e(t) = \mathbb{C} : \boldsymbol{\varepsilon}(t)$, and

$$\delta_i = \begin{cases} 1 & \varepsilon_{ii} \leq 0 \\ S_f & \varepsilon_{ii} > 0 \end{cases} . \tag{135}$$

The model 74 damage test utilizes load case 6 ($\bar{\gamma} = 0.1$) and the material parameterization given in table 112. The expected results are confirmed in table 113 and figure 70, where both delamination and in-plane failure are observed to occur at staggered times.

Table 112: Material parameterization for the model 74 damage test

Parameter	Value
Elastic modulus, E	7.5
Poisson's ratio, ν	0.25
Fully-damaged nominal shell Young's modulus, $\bar{E}_f$	6.0
Fully-damaged nominal shell shear modulus, $\bar{G}_f$	3.0
Fully-damaged material scale factor, S_f	0.1
Delamination - B-C shear strength, S_5	0.5
Delamination - A-C shear strength, S_6	0.5
Delamination damage growth factor, F_{delam}	0.1
Hyperbolic delamination evolution factor, $\bar{R}_{delam}$	0.0
Fiber tensile strain at failure, ε_{ten}	0.1
Fiber compressive strain at failure, ε_{comp}	-0.1
In-plane damage growth factor, $F_{inplane}$	0.1
Hyperbolic in-plane evolution factor, $\bar{R}_{inplane}$	0.0

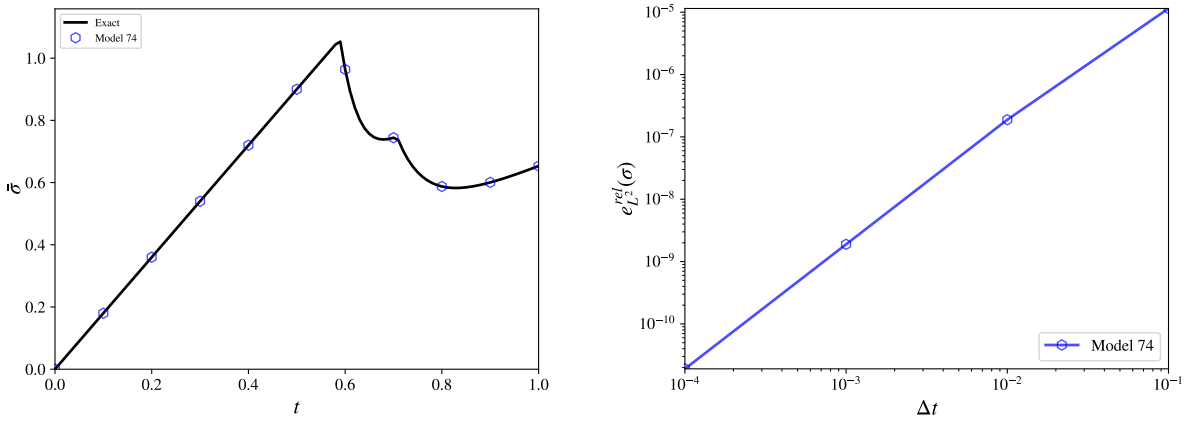

(a) Time-history plot of $\bar{\sigma}$ vs. t using $\Delta t = 0.1$.

(b) Convergence plot for $e^{\text{rel}}_{L^2}(\boldsymbol{\sigma})$ errors vs. Δt.

Figure 70: Model 74 damage test.

Table 113: Computed errors for model 74 damage test.

Model	$e^{\text{rel}}_{L^2}(\boldsymbol{\sigma})$	r	$e^{\text{abs}}_{L^2}(\varepsilon_{33})$	r	$e^{\text{abs}}_{L^2}(\bar{\varepsilon}^p)$	r	Status
74	1.903e-11	1.78	6.265e-15	2.00	0.000e+00	-	✓

4.6 Miscellaneous Model Features

In addition to the categorically grouped features discussed in the preceeding sections, a number of additional miscellaneous features are available for shell elements which provide unique functionalities. These features (some of which are specific to individual models) are presented in the following sub-sections.

4.6.1 Shear Factor

All shell element material models allow for the specification of a "shear correction factor" (denoted κ) which is used to re-scale the elastic moduli for transverse shear deformations. For many elasto-plasticity models, this behavior is effectively achieved by instead re-scaling the transverse shear strains ε_{13} and ε_{23}, directly. While this simplification results in characteristically different behavior under plastic loading, it conveniently avoids complicating the existing implementation of the radial return algorithm for isotropic materials.

To verify the correct behavior of the shear factor, a simple test is devised involving pure transverse shearing, occuring simultaneously in the ε_{13} and ε_{23} components of strain (using the loading parameters $-\dot{\theta}_1 = \dot{\theta}_2 = 2\bar{\gamma}$ with $\bar{\gamma} = 0.01$), and the material parameterization given in table 114. For the chosen problem setup, purely elastic material behavior is expected to give rise to transverse shear stresses which are effectively diminished by a factor of κ.

The results of the shear factor test presented in table 115 and figure 71 confirm the expected behavior consistent with the original isotropic elasticity tests 4 and 5 from [3], with all models yielding sufficiently small errors (on the order of machine precision) in all metrics.

Table 114: Material parameterization for the shear factor test.

Parameter	Value
Elastic modulus, E	7.5
Poisson's ratio, ν	0.25
Shear factor, κ	0.5

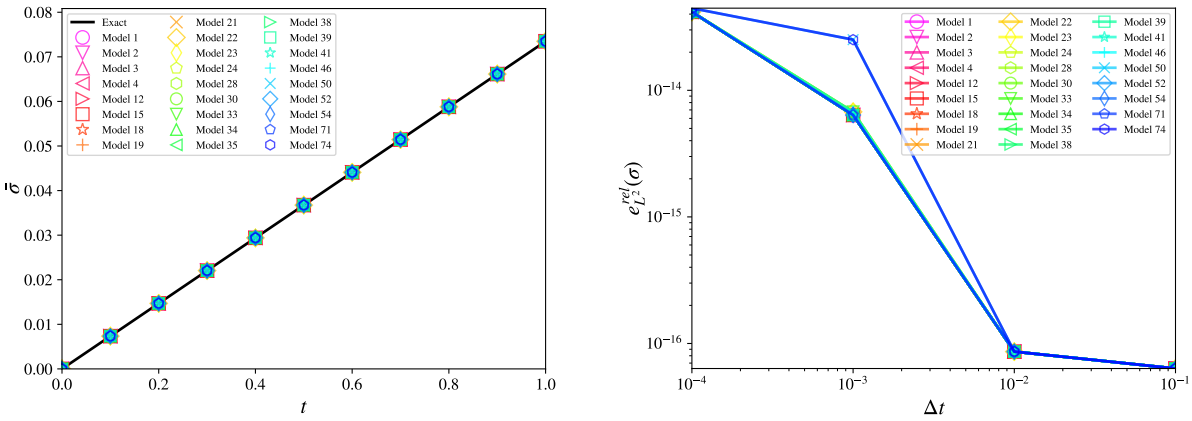

(a) Time-history plot of $\bar{\sigma}$ vs. t using $\Delta t = 0.1$.

(b) Convergence plot for $e_{L^2}^{\text{rel}}(\boldsymbol{\sigma})$ errors vs. Δt.

Figure 71: Shear factor test.

Table 115: Computed errors for the shear factor test.

Model	$e_{L^2}^{\text{rel}}(\boldsymbol{\sigma})$	r	$e_{L^2}^{\text{abs}}(\varepsilon_{33})$	r	$e_{L^2}^{\text{abs}}(\bar{\varepsilon}^p)$	r	Status
1	4.163e-14	-	0.000e+00	-	0.000e+00	-	✓
2	4.163e-14	-	0.000e+00	-	0.000e+00	-	✓
3	4.163e-14	-	0.000e+00	-	0.000e+00	-	✓
4	4.163e-14	-	0.000e+00	-	0.000e+00	-	✓
12	4.163e-14	-	0.000e+00	-	0.000e+00	-	✓
15	4.163e-14	-	0.000e+00	-	0.000e+00	-	✓
18	4.163e-14	-	0.000e+00	-	0.000e+00	-	✓
19	4.163e-14	-	0.000e+00	-	0.000e+00	-	✓
21	4.163e-14	-	0.000e+00	-	0.000e+00	-	✓
22	4.163e-14	-	0.000e+00	-	0.000e+00	-	✓
23	4.163e-14	-	0.000e+00	-	0.000e+00	-	✓
24	4.163e-14	-	0.000e+00	-	0.000e+00	-	✓
28	4.163e-14	-	0.000e+00	-	0.000e+00	-	✓
30	4.163e-14	-	0.000e+00	-	0.000e+00	-	✓
33	4.163e-14	-	0.000e+00	-	0.000e+00	-	✓
34	4.163e-14	-	0.000e+00	-	0.000e+00	-	✓
35	4.163e-14	-	0.000e+00	-	0.000e+00	-	✓
38	4.163e-14	-	0.000e+00	-	0.000e+00	-	✓
39	4.163e-14	-	0.000e+00	-	0.000e+00	-	✓
41	4.163e-14	-	0.000e+00	-	0.000e+00	-	✓
46	4.163e-14	-	0.000e+00	-	0.000e+00	-	✓
50	4.455e-14	-	0.000e+00	-	0.000e+00	-	✓
52	4.163e-14	-	0.000e+00	-	0.000e+00	-	✓
54	4.163e-14	-	0.000e+00	-	0.000e+00	-	✓
71	4.163e-14	-	0.000e+00	-	0.000e+00	-	✓
74	4.456e-14	-	0.000e+00	-	0.000e+00	-	✓

4.6.2 Multi-Material Shell (Model 42)

Shell model 42 permits the specification of different material models and property sets at each through-thickness integration point of the element, thereby allowing for the modeling of laminated composite structures.

To verify the compatible behavior of model 42 with every other shell element material model, a variation on isotropic elasticity test 1 (presented in [3]) is adapted with the corresponding material parameterization given in table 116, entailing the definition of 26 through-thickness integration points – one for each stand-alone shell model considered in the original isotropic elasticity test suite.

The results for each such sub-model (summarized in table 117 and figure 72) are observed to be identical to the results obtained for isotropic elasticity test 1, thereby confirming the correct behavior of model 42 when used in conjunction with any other shell element material model.

Table 116: Material parameterization for the multi-material shell test

Parameter	Value
Elastic modulus, E	7.5
Poisson's ratio, ν	0.25
β angle input flag, α	1
Material angle, β	0.0
Number of materials, N_{mats}	26

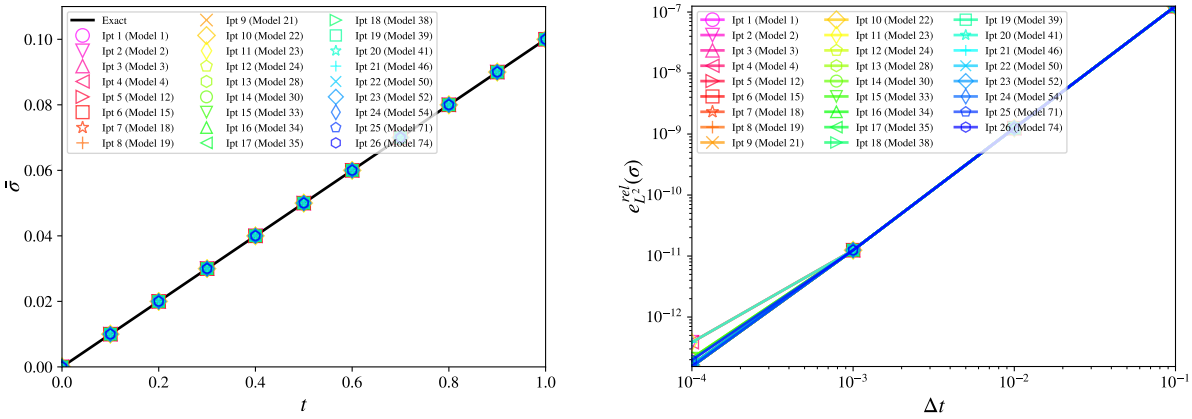

(a) Time-history plot of $\bar{\sigma}$ vs. t using $\Delta t = 0.1$.

(b) Convergence plot for $e^{\text{rel}}_{L^2}(\boldsymbol{\sigma})$ errors vs. Δt.

Figure 72: Multi-material shell (model 42) test.

Table 117: Computed errors for the multi-material shell model test.

Ipt	$e^{\text{rel}}_{L^2}(\boldsymbol{\sigma})$	r	$e^{\text{rel}}_{L^2}(\varepsilon_{33})$	r	$e^{\text{abs}}_{L^2}(\bar{\varepsilon}^p)$	r	Status
1 (Model 1)	1.971e-13	1.80	2.236e-13	1.75	0.000e+00	-	✓
2 (Model 2)	3.861e-13	1.51	2.236e-13	1.75	0.000e+00	-	✓
3 (Model 3)	1.545e-13	1.91	2.236e-13	1.75	0.000e+00	-	✓
4 (Model 4)	3.861e-13	1.51	2.236e-13	1.75	0.000e+00	-	✓
5 (Model 12)	1.545e-13	1.91	2.236e-13	1.75	0.000e+00	-	✓
6 (Model 15)	1.545e-13	1.91	2.236e-13	1.75	0.000e+00	-	✓
7 (Model 18)	1.545e-13	1.91	2.236e-13	1.75	0.000e+00	-	✓
8 (Model 19)	1.656e-13	1.88	2.236e-13	1.75	0.000e+00	-	✓
9 (Model 21)	1.545e-13	1.91	2.236e-13	1.75	0.000e+00	-	✓
10 (Model 22)	1.545e-13	1.91	2.236e-13	1.75	0.000e+00	-	✓
11 (Model 23)	3.861e-13	1.51	2.236e-13	1.75	0.000e+00	-	✓
12 (Model 24)	1.545e-13	1.91	2.236e-13	1.75	0.000e+00	-	✓
13 (Model 28)	2.113e-13	1.77	2.236e-13	1.75	0.000e+00	-	✓
14 (Model 30)	2.113e-13	1.77	2.236e-13	1.75	0.000e+00	-	✓
15 (Model 33)	2.113e-13	1.77	2.236e-13	1.75	0.000e+00	-	✓
16 (Model 34)	1.545e-13	1.91	2.236e-13	1.75	0.000e+00	-	✓
17 (Model 35)	1.656e-13	1.88	2.236e-13	1.75	0.000e+00	-	✓
18 (Model 38)	1.656e-13	1.88	2.236e-13	1.75	0.000e+00	-	✓
19 (Model 39)	1.656e-13	1.88	2.236e-13	1.75	0.000e+00	-	✓
20 (Model 41)	1.545e-13	1.91	2.236e-13	1.75	0.000e+00	-	✓
21 (Model 46)	3.861e-13	1.51	2.236e-13	1.75	0.000e+00	-	✓
22 (Model 50)	1.972e-13	1.80	2.236e-13	1.75	0.000e+00	-	✓
23 (Model 52)	1.656e-13	1.88	2.236e-13	1.75	0.000e+00	-	✓
24 (Model 54)	1.545e-13	1.91	2.236e-13	1.75	0.000e+00	-	✓
25 (Model 71)	1.545e-13	1.91	2.236e-13	1.75	0.000e+00	-	✓
26 (Model 74)	1.972e-13	1.80	2.236e-13	1.75	0.000e+00	-	✓

4.6.3 Material Axes Options

All orthotropic elastic models (2, 21, 22, 23, 33, 41, 46, 50, and 74) allow for their local material axes (denoted **a**, **b**, **c**) to be specified via the *AOPT* flag. The *AOPT* variable may assume a value of 0-6 or 11, corresponding to the following definitions:

$AOPT = 0$ The default option, where the in-plane vectors **a** and **d** are colinear to the element edges emanating from the first node, and subsequently orthonormalized to obtain **b** and **c**.

$AOPT = 1$ Determines the vector $\mathbf{a} = \mathbf{x}_c - \mathbf{x}_p$ as the difference between the element center $\mathbf{x}_c$ and a point P with global coordinates $\mathbf{x}_p$, and the vector **d** is colinear with the global $z-$axis. Subsequently, the vectors $\mathbf{c} = \mathbf{a} \times \mathbf{d}$ and $\mathbf{b} = \mathbf{c} \times \mathbf{a}$ are computed.

$AOPT = 2$ Two vectors **a** and **d** are directly specified, and used to compute $\mathbf{c} = \mathbf{a} \times \mathbf{d}$ and $\mathbf{b} = \mathbf{c} \times \mathbf{a}$.

$AOPT = 3$ The vector **v** and angle β are specified and used to compute $\mathbf{a} = \mathbf{R}_\beta \cdot (\mathbf{v} \times \mathbf{n})$, where **n** is the shell normal and $\mathbf{R}_\beta$ is a rotation matrix which rotates vectors about the shell normal axis by the angle β. Subsequently, the vectors $\mathbf{c} = \mathbf{n}$ and $\mathbf{b} = \mathbf{c} \times \mathbf{a}$ are computed.

$AOPT = 4$ A cylindrical coordinate system is specified with its origin at point P with coordinate $\mathbf{x}_p$, and with the cylindrical axis aligned with the vector **d**. For a given element with center coordinate $\mathbf{x}_c$, the remaining vectors are determined by $\mathbf{b} = (\mathbf{x}_c - \mathbf{x}_p) \times \mathbf{d}$, $\mathbf{c} = \mathbf{d} \times \mathbf{b}$, and $\mathbf{a} = \mathbf{b} \times \mathbf{c}$ (such that **a** and **d** are parallel).

$AOPT = 5$ A conical coordinate system with conical angle α is specified with its origin at $\mathbf{x}_p$, and with the conical axis aligned with the vector **d**. Letting $\mathbf{d} \leftarrow \mathbf{d}/||\mathbf{d}||_2$ (an assumption that needs to be verified for each material model), the coordinate system established at point $\mathbf{x}_c$ is given by the vectors $\mathbf{c} = (\mathbf{1} - \mathbf{d} \otimes \mathbf{d}) \cdot (\mathbf{x}_c - \mathbf{x}_p)$, $\mathbf{a} = \cos(\alpha)\mathbf{d} - \sin(\alpha)\mathbf{c}$, and $\mathbf{b} = \mathbf{c} \times \mathbf{a}$.

$AOPT = 6$ An ellipsoidal coordinate system centered at $\mathbf{x}_p$ is specified with principal radii r_a, r_b, r_c (whose ratios are specified by $r_1 = \frac{r_a}{r_c}$, $r_2 = \frac{r_b}{r_c}$), with the vector **d** colinear with the first axis of the ellipse, and the vector **u** coplanar with the first and third axes. Assuming $\mathbf{d} \leftarrow \mathbf{d}/||\mathbf{d}||_2$, a transformation **J** from the global ellipsoidal coordinate system to a local spherical coordinate system is obtained via

$$\mathbf{J} = \begin{bmatrix} \mathbf{v}_a/r_1 \\ \mathbf{v}_b/r_2 \\ \mathbf{d} \end{bmatrix}, \tag{136}$$

where $\mathbf{v}_b = \frac{\mathbf{d} \times \mathbf{u}}{||\mathbf{d} \times \mathbf{u}||_2}$ and $\mathbf{v}_a = \frac{\mathbf{v}_b \times \mathbf{d}}{||\mathbf{v}_b \times \mathbf{d}||_2}$. The position $\mathbf{g} = \mathbf{J} \cdot (\mathbf{x}_c - \mathbf{x}_p)$ established in the spherical coordinate system can be used to determine the angles $\phi = \cos^{-1}(g_3/||\mathbf{r}||_2)$ and $\theta = \tan^{-1}(g_2/g_1)$ measured from the local $\mathbf{e}_3$ and $\mathbf{e}_1$ axes, respectively. The vectors **a**, **b**, and **c** are then determined as

$$\mathbf{a} = \mathbf{J}^{-1} \cdot \begin{Bmatrix} -\cos\phi\,\cos\theta \\ -\cos\phi\,\sin\theta \\ \sin\phi \end{Bmatrix}, \qquad \mathbf{b} = \mathbf{c} \times \mathbf{a}, \qquad \mathbf{c} = \mathrm{cof}(\mathbf{J}^{-1}) \cdot \begin{Bmatrix} \sin\phi\,\cos\theta \\ \sin\phi\,\sin\theta \\ \cos\phi \end{Bmatrix}, \tag{137}$$

where $\mathrm{cof}(\mathbf{J}^{-1}) = \frac{1}{\det \mathbf{J}}\mathbf{J}^T$.

$AOPT = 11$ The vectors **a** and **b** are specified directly for individual shell elements, using as many element material axes cards.

Following the computation/specification of vectors **a** and **b**, a modified set of material axes $\mathbf{a}_p$ and $\mathbf{b}_p$ lying in the plane of the shell are obtained in the following fashion using the shell normal **n**: if **a** and **n** are not colinear, $\mathbf{b}_p = \mathbf{n} \times \mathbf{a}$ and $\mathbf{a}_p = \mathbf{b}_p \times \mathbf{n}$; otherwise $\mathbf{a}_p = \mathbf{b} \times \mathbf{n}$ and $\mathbf{b}_p = \mathbf{a}_p \times \mathbf{n}$.

All of the subsequently defined material axes option tests (for options 1-6 and 11) are equivalent to orthotropic elasticity test 7 presented in [3]. The material axes options are specified such that the same orthotropic material axes are obtained as in the original test using the default option $AOPT = 0$, and thus the numerical results are expected to be identical.

The extending parameterizations for the material axis options employed by each test are summarized in tables 118 ($AOPT = 1$), 120 ($AOPT = 2$), 122 ($AOPT = 3$), 124 ($AOPT = 4$), 126 ($AOPT = 5$), 128 ($AOPT = 6$), and 130 ($AOPT = 11$). The corresponding results for each of the aforementioned parameter sets are presented respectively in tables 119, 121, 123, 125, 127, 129, 131, and figures 73-79. For all tests, resulting errors on the order of machine precision indicate that the material axes options are functioning as intended.

Table 118: Material parameterization for the material axes option 1 test

Parameter	Value
Point P x-coordinate, x_p	0.0
Point P y-coordinate, y_p	0.0
Point P z-coordinate, z_p	0.0

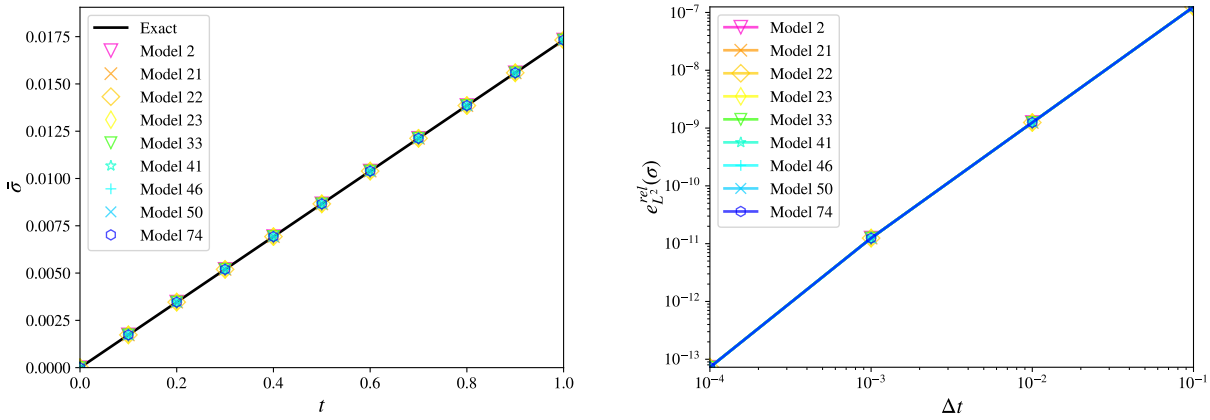

(a) Time-history plot of $\bar{\sigma}$ vs. t using $\Delta t = 0.1$.

(b) Convergence plot for $e^{\text{rel}}_{L^2}(\boldsymbol{\sigma})$ errors vs. Δt.

Figure 73: Material axes option 1 test.

Table 119: Computed errors for the material axes option 1 test.

Model	$e^{\text{rel}}_{L^2}(\boldsymbol{\sigma})$	r	$e^{\text{abs}}_{L^2}(\varepsilon_{33})$	r	$e^{\text{abs}}_{L^2}(\bar{\varepsilon}^p)$	r	Status
2	7.274e-14	2.00	0.000e+00	-	0.000e+00	-	✓
21	7.274e-14	2.00	0.000e+00	-	0.000e+00	-	✓
22	7.274e-14	2.00	0.000e+00	-	0.000e+00	-	✓
23	7.274e-14	2.00	0.000e+00	-	0.000e+00	-	✓
33	7.274e-14	2.00	0.000e+00	-	0.000e+00	-	✓
41	7.274e-14	2.00	0.000e+00	-	0.000e+00	-	✓
46	7.274e-14	2.00	0.000e+00	-	0.000e+00	-	✓
50	7.274e-14	2.00	0.000e+00	-	0.000e+00	-	✓
74	7.274e-14	2.00	0.000e+00	-	0.000e+00	-	✓

Table 120: Material parameterization for the material axes option 2 test

Parameter	Value
Vector **a** x-coordinate, a_x	1.0
Vector **a** y-coordinate, a_y	0.0
Vector **a** z-coordinate, a_z	0.0
Vector **d** x-coordinate, d_x	0.0
Vector **d** y-coordinate, d_y	1.0
Vector **d** z-coordinate, d_z	0.0

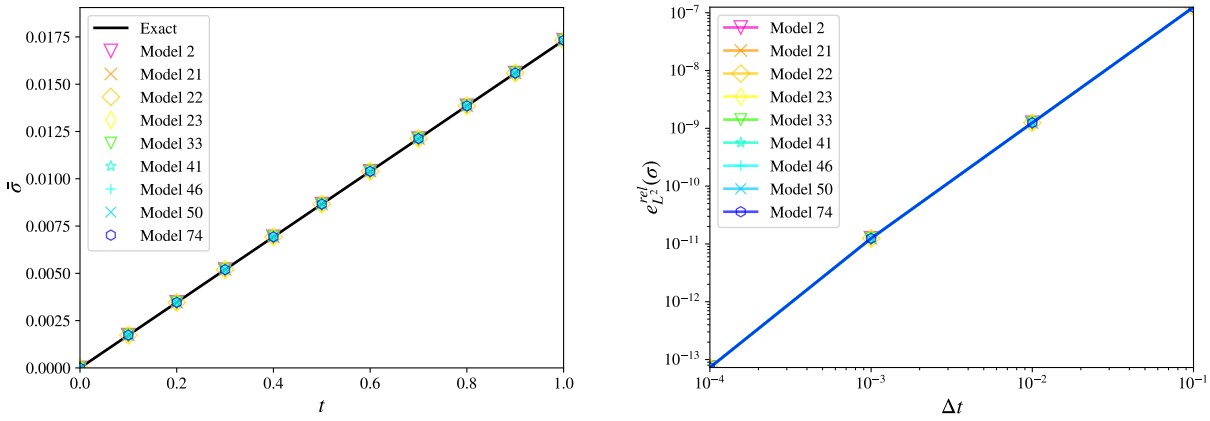

(a) Time-history plot of $\bar{\sigma}$ vs. t using $\Delta t = 0.1$.

(b) Convergence plot for $e_{L^2}^{\text{rel}}(\boldsymbol{\sigma})$ errors vs. Δt.

Figure 74: Material axes option 2 test.

Table 121: Computed errors for the material axes option 2 test.

Model	$e_{L^2}^{\text{rel}}(\boldsymbol{\sigma})$	r	$e_{L^2}^{\text{abs}}(\varepsilon_{33})$	r	$e_{L^2}^{\text{abs}}(\bar{\varepsilon}^p)$	r	Status
2	7.274e-14	2.00	0.000e+00	-	0.000e+00	-	✓
21	7.274e-14	2.00	0.000e+00	-	0.000e+00	-	✓
22	7.274e-14	2.00	0.000e+00	-	0.000e+00	-	✓
23	7.274e-14	2.00	0.000e+00	-	0.000e+00	-	✓
33	7.274e-14	2.00	0.000e+00	-	0.000e+00	-	✓
41	7.274e-14	2.00	0.000e+00	-	0.000e+00	-	✓
46	7.274e-14	2.00	0.000e+00	-	0.000e+00	-	✓
50	7.274e-14	2.00	0.000e+00	-	0.000e+00	-	✓
74	7.274e-14	2.00	0.000e+00	-	0.000e+00	-	✓

Table 122: Material parameterization for the material axes option 3 test

Parameter	Value
Vector **v** x-coordinate, v_x	1.0
Vector **v** y-coordinate, v_y	0.0
Vector **v** z-coordinate, v_z	0.0
Material angle, β	-90.0

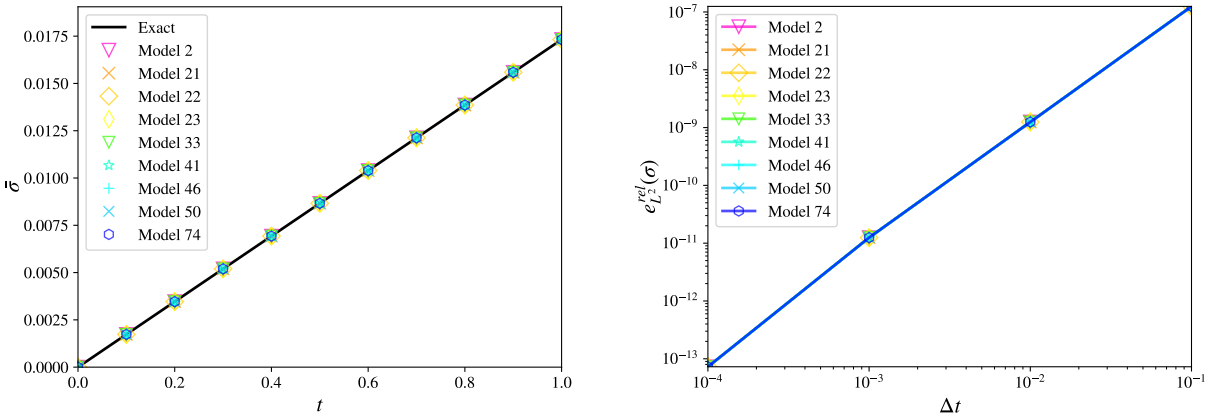

(a) Time-history plot of $\bar{\sigma}$ vs. t using $\Delta t = 0.1$.

(b) Convergence plot for $e^{\text{rel}}_{L^2}(\boldsymbol{\sigma})$ errors vs. Δt.

Figure 75: Material axes option 3 test.

Table 123: Computed errors for the material axes option 3 test.

Model	$e^{\text{rel}}_{L^2}(\boldsymbol{\sigma})$	r	$e^{\text{abs}}_{L^2}(\varepsilon_{33})$	r	$e^{\text{abs}}_{L^2}(\bar{\varepsilon}^p)$	r	Status
2	7.274e-14	2.00	0.000e+00	-	0.000e+00	-	✓
21	7.274e-14	2.00	0.000e+00	-	0.000e+00	-	✓
22	7.274e-14	2.00	0.000e+00	-	0.000e+00	-	✓
23	7.274e-14	2.00	0.000e+00	-	0.000e+00	-	✓
33	7.274e-14	2.00	0.000e+00	-	0.000e+00	-	✓
41	7.274e-14	2.00	0.000e+00	-	0.000e+00	-	✓
46	7.274e-14	2.00	0.000e+00	-	0.000e+00	-	✓
50	7.274e-14	2.00	0.000e+00	-	0.000e+00	-	✓
74	7.274e-14	2.00	0.000e+00	-	0.000e+00	-	✓

Table 124: Material parameterization for the material axes option 4 test

Parameter	Value
Point P x-coordinate, x_p	0.0
Point P y-coordinate, y_p	0.0
Point P z-coordinate, z_p	0.0
Vector $\mathbf{d}$ x-coordinate, d_x	0.0
Vector $\mathbf{d}$ y-coordinate, d_y	0.0
Vector $\mathbf{d}$ z-coordinate, d_z	1.0

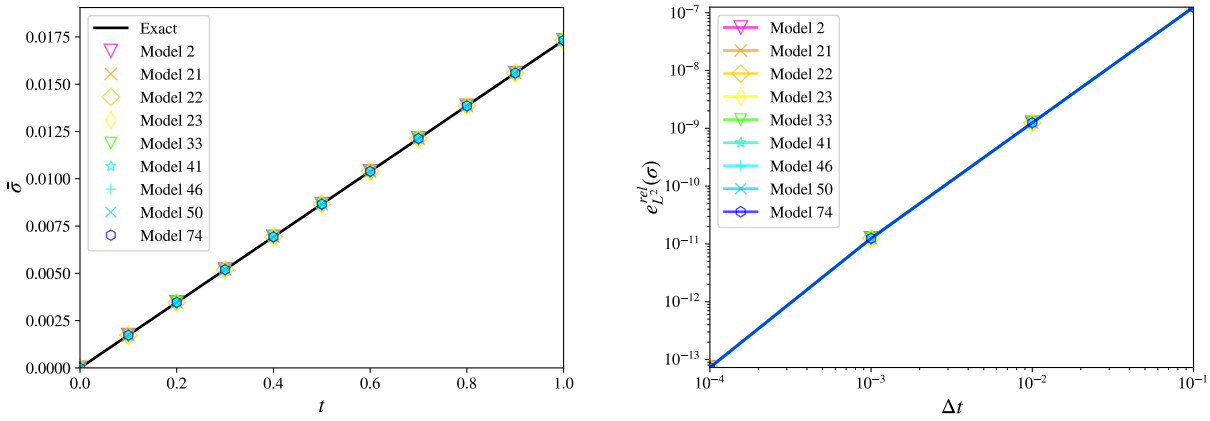

(a) Time-history plot of $\bar{\sigma}$ vs. t using $\Delta t = 0.1$.

(b) Convergence plot for $e_{L^2}^{\text{rel}}(\boldsymbol{\sigma})$ errors vs. Δt.

Figure 76: Material axes option 4 test.

Table 125: Computed errors for the material axes option 4 test.

Model	$e_{L^2}^{\text{rel}}(\boldsymbol{\sigma})$	r	$e_{L^2}^{\text{abs}}(\varepsilon_{33})$	r	$e_{L^2}^{\text{abs}}(\bar{\varepsilon}^p)$	r	Status
2	7.274e-14	2.00	0.000e+00	-	0.000e+00	-	✓
21	7.274e-14	2.00	0.000e+00	-	0.000e+00	-	✓
22	7.274e-14	2.00	0.000e+00	-	0.000e+00	-	✓
23	7.274e-14	2.00	0.000e+00	-	0.000e+00	-	✓
33	7.274e-14	2.00	0.000e+00	-	0.000e+00	-	✓
41	7.274e-14	2.00	0.000e+00	-	0.000e+00	-	✓
46	7.274e-14	2.00	0.000e+00	-	0.000e+00	-	✓
50	7.274e-14	2.00	0.000e+00	-	0.000e+00	-	✓
74	7.274e-14	2.00	0.000e+00	-	0.000e+00	-	✓

Table 126: Material parameterization for the material axes option 5 test

Parameter	Value
Conical angle, α	45.0
Point P x-coordinate, x_p	0.0
Point P y-coordinate, y_p	0.0
Point P z-coordinate, z_p	0.0
Vector $\mathbf{d}$ x-coordinate, d_x	1.0
Vector $\mathbf{d}$ y-coordinate, d_y	0.0
Vector $\mathbf{d}$ z-coordinate, d_z	1.0

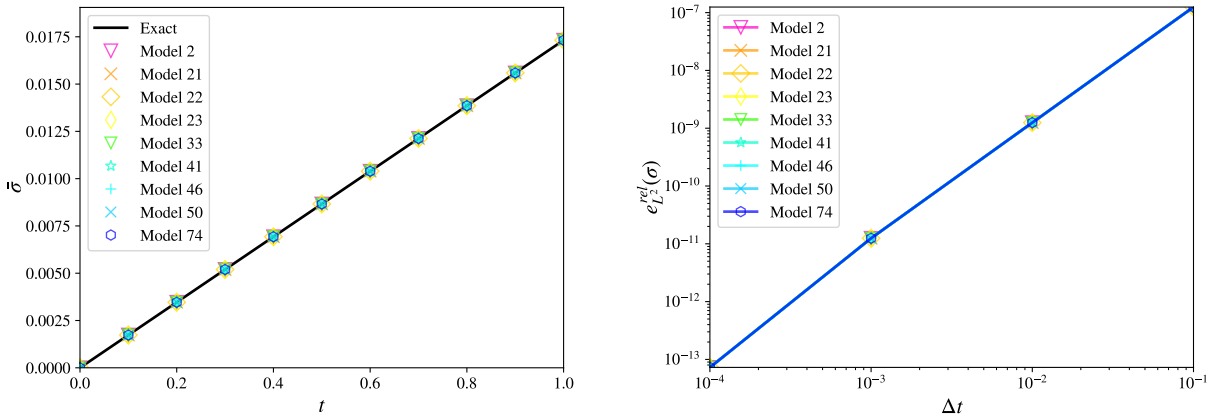

(a) Time-history plot of $\bar{\sigma}$ vs. t using $\Delta t = 0.1$.

(b) Convergence plot for $e^{\text{rel}}_{L^2}(\boldsymbol{\sigma})$ errors vs. Δt.

Figure 77: Material axes option 5 test.

Table 127: Computed errors for the material axes option 5 test.

Model	$e^{\text{rel}}_{L^2}(\boldsymbol{\sigma})$	r	$e^{\text{abs}}_{L^2}(\varepsilon_{33})$	r	$e^{\text{abs}}_{L^2}(\bar{\varepsilon}^p)$	r	Status
2	7.274e-14	2.00	0.000e+00	-	0.000e+00	-	✓
21	7.274e-14	2.00	0.000e+00	-	0.000e+00	-	✓
22	7.274e-14	2.00	0.000e+00	-	0.000e+00	-	✓
23	7.274e-14	2.00	0.000e+00	-	0.000e+00	-	✓
33	7.274e-14	2.00	0.000e+00	-	0.000e+00	-	✓
41	7.274e-14	2.00	0.000e+00	-	0.000e+00	-	✓
46	7.274e-14	2.00	0.000e+00	-	0.000e+00	-	✓
50	7.274e-14	2.00	0.000e+00	-	0.000e+00	-	✓
74	7.274e-14	2.00	0.000e+00	-	0.000e+00	-	✓

Table 128: Material parameterization for the material axes option 6 test

Parameter	Value
Ratio of principal radii a and c, r_1	2.0
Ratio of principal radii b and c, r_2	3.0
Point P x-coordinate, x_p	0.0
Point P y-coordinate, y_p	0.0
Point P z-coordinate, z_p	-1.0
Vector $\mathbf{u}$ x-coordinate, u_x	0.0
Vector $\mathbf{u}$ y-coordinate, u_y	1.0
Vector $\mathbf{u}$ z-coordinate, u_z	0.0
Vector $\mathbf{d}$ x-coordinate, d_x	1.0
Vector $\mathbf{d}$ y-coordinate, d_y	0.0
Vector $\mathbf{d}$ z-coordinate, d_z	0.0

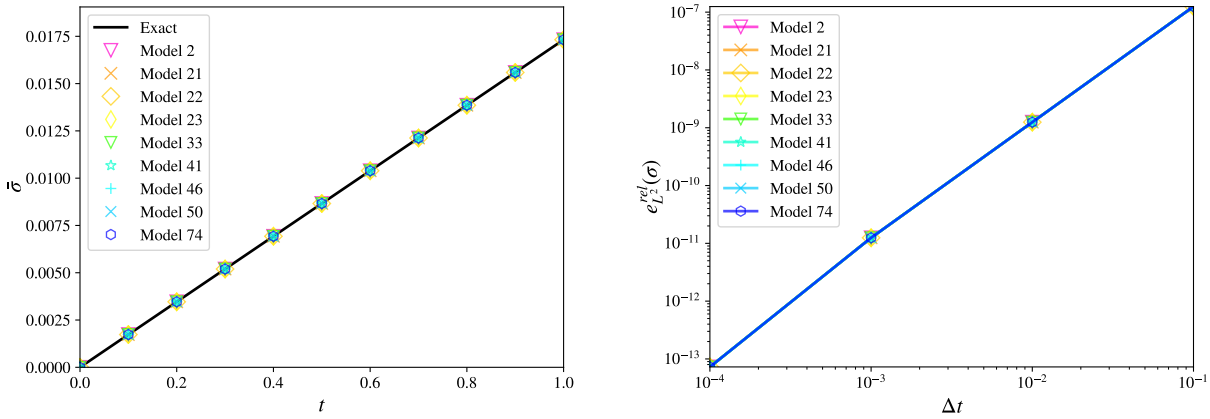

(a) Time-history plot of $\bar{\sigma}$ vs. t using $\Delta t = 0.1$.

(b) Convergence plot for $e^{\text{rel}}_{L^2}(\boldsymbol{\sigma})$ errors vs. Δt.

Figure 78: Material axes option 6 test.

Table 129: Computed errors for the material axes option 6 test.

Model	$e^{\text{rel}}_{L^2}(\boldsymbol{\sigma})$	r	$e^{\text{abs}}_{L^2}(\varepsilon_{33})$	r	$e^{\text{abs}}_{L^2}(\bar{\varepsilon}^p)$	r	Status
2	7.274e-14	2.00	0.000e+00	-	0.000e+00	-	✓
21	7.274e-14	2.00	0.000e+00	-	0.000e+00	-	✓
22	7.274e-14	2.00	0.000e+00	-	0.000e+00	-	✓
23	7.274e-14	2.00	0.000e+00	-	0.000e+00	-	✓
33	7.274e-14	2.00	0.000e+00	-	0.000e+00	-	✓
41	7.274e-14	2.00	0.000e+00	-	0.000e+00	-	✓
46	7.274e-14	2.00	0.000e+00	-	0.000e+00	-	✓
50	7.274e-14	2.00	0.000e+00	-	0.000e+00	-	✓
74	7.274e-14	2.00	0.000e+00	-	0.000e+00	-	✓

Table 130: Material parameterization for the material axes option 11 test

Parameter	Value
Vector **a** x-coordinate, a_x	1.0
Vector **a** y-coordinate, a_y	0.0
Vector **a** z-coordinate, a_z	0.0
Vector **b** x-coordinate, b_x	0.0
Vector **b** y-coordinate, b_y	1.0
Vector **b** z-coordinate, b_z	0.0

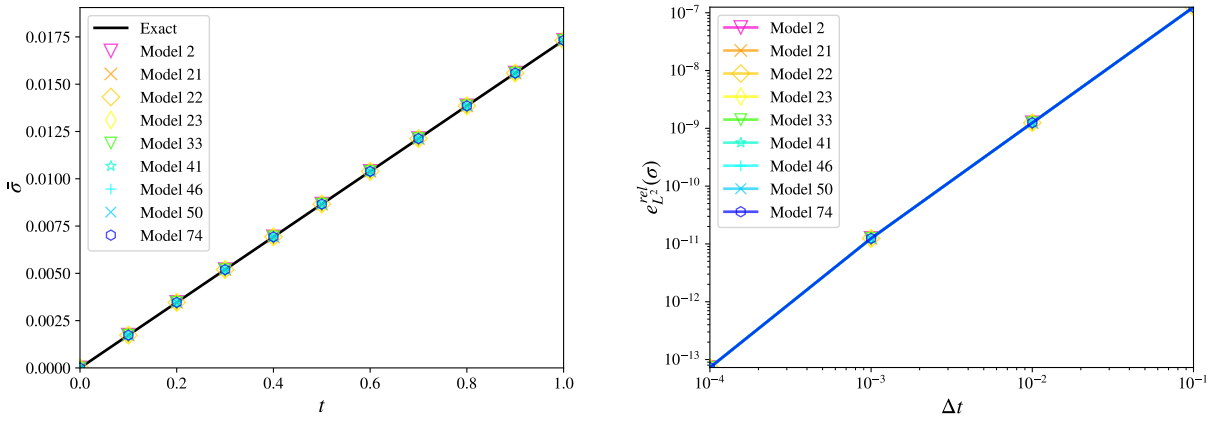

(a) Time-history plot of $\bar{\sigma}$ vs. t using $\Delta t = 0.1$.

(b) Convergence plot for $e_{L^2}^{\text{rel}}(\boldsymbol{\sigma})$ errors vs. Δt.

Figure 79: Material axes option 11 test.

Table 131: Computed errors for the material axes option 11 test.

Model	$e_{L^2}^{\text{rel}}(\boldsymbol{\sigma})$	r	$e_{L^2}^{\text{abs}}(\varepsilon_{33})$	r	$e_{L^2}^{\text{abs}}(\bar{\varepsilon}^p)$	r	Status
2	7.274e-14	2.00	0.000e+00	-	0.000e+00	-	✓
21	7.274e-14	2.00	0.000e+00	-	0.000e+00	-	✓
22	7.274e-14	2.00	0.000e+00	-	0.000e+00	-	✓
23	7.274e-14	2.00	0.000e+00	-	0.000e+00	-	✓
33	7.274e-14	2.00	0.000e+00	-	0.000e+00	-	✓
41	7.274e-14	2.00	0.000e+00	-	0.000e+00	-	✓
46	7.274e-14	2.00	0.000e+00	-	0.000e+00	-	✓
50	7.274e-14	2.00	0.000e+00	-	0.000e+00	-	✓
74	7.274e-14	2.00	0.000e+00	-	0.000e+00	-	✓

4.6.4 Debug Run

Models 2 and 46 provide the option of invoking a "debug run" via a flag specified in the material card input section. Activation of a debug run triggers a single time step to be taken, and the output of additional plotting data (namely the material axes **a** and **b** used by orthotropic models).

The debug run test for models 2 and 46 is a direct adaptation of the setup used by isotropic elasticity test 1 (refer to [3]) with the debug run flag set equal to 1. As noted in table 132, activation of the debug run feature is easily verified by direct examination of the model-specific messages contained in the .hsp file, or by observing that only the first output state is reported to the .hsp and .plt files; no stress-based output is therefore provided by the analysis.

Table 132: Recorded results for the debug run test.

Model	.hsp message confirmation	number of output states	Status
2	yes	1	✓
46	yes	1	✓

4.6.5 Non-linear Shear

Models 22 and 41 accomodate non-linear shear behavior characterized by the following relationship between the material-aligned shear stress σ_{ab} and shear strain ε_{ab}:

$$2\varepsilon_{ab} = \frac{\sigma_{ab}}{\mu_{ab}} + \alpha\,\sigma_{ab}^3, \tag{138}$$

where α denotes the non-linear shear parameter, as described in reference [2].

For load case 3 ($\bar{\gamma} = 0.1$) with $\varepsilon_{ab}(t) = \bar{\gamma}t$ and the material parameterization given in table 133, an exact solution for $\sigma_{ab}(t)$ is obtained as

$$\sigma_{ab}(t) = \frac{1}{f(t)} - \frac{f(t)}{3\alpha\mu_{ab}}, \qquad f(t) = \left[\sqrt{\left[(3\mu_{ab})^3\alpha^2\bar{\gamma}t\right]^2 + (3\mu_{ab})^3\alpha^3} - (3\mu_{ab})^3\alpha^2\bar{\gamma}t\right]^{\frac{1}{3}}. \tag{139}$$

The results of the non-linear shear test for models 22 and 41 reproduce the above expected behavior, as demonstrated in table 134 and figure 80.

Table 133: Material parameterization for the model 22 & 41 non-linear shear test

Parameter	Value
Elastic modulus, E	2.0
Poisson's ratio, ν	0.0
Nonlinear shear stress parameter, α	1000.0

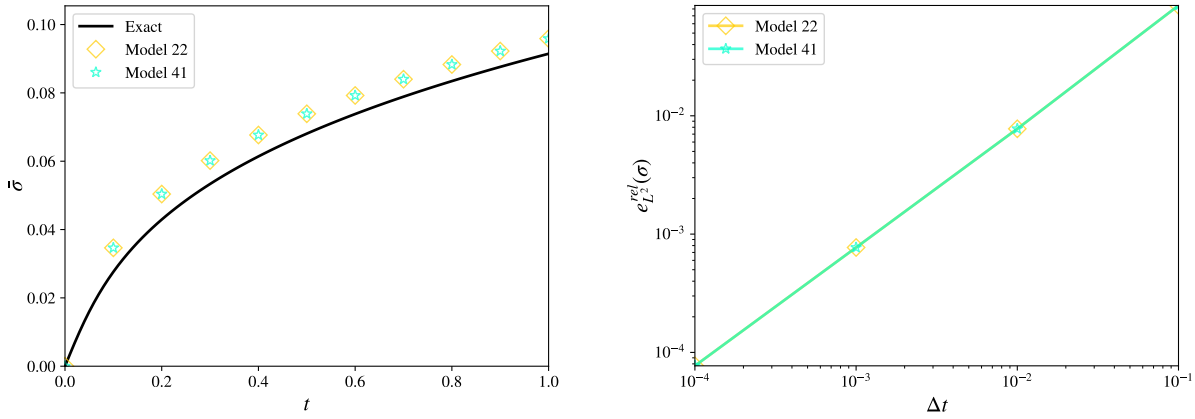

(a) Time-history plot of $\bar{\sigma}$ vs. t using $\Delta t = 0.1$.

(b) Convergence plot for $e^{\text{rel}}_{L^2}(\boldsymbol{\sigma})$ errors vs. Δt.

Figure 80: Model 22 and 41 non-linear shear test.

Table 134: Computed errors for the model 22 and 41 non-linear shear test.

Model	$e^{\text{rel}}_{L^2}(\boldsymbol{\sigma})$	r	$e^{\text{abs}}_{L^2}(\varepsilon_{33})$	r	$e^{\text{abs}}_{L^2}(\bar{\varepsilon}^p)$	r	Status
22	7.702e-05	1.00	0.000e+00	-	0.000e+00	-	✓
41	7.702e-05	1.00	0.000e+00	-	0.000e+00	-	✓

4.6.6 Kinematic Formulation

Models 41 and 50 allow for the optional use of either a hypo-elastic or hyper-elastic kinematic formumulation for shell elements via the specification of a kinematic formulation flag. By default, the hypo-elastic formulation is used (consistent with all other shell element material models).

Nominally, the hyper-elastic formulation specifies a direct linear relationship between the 2$^{\text{nd}}$ Piola-Kirchhoff stress $\mathbf{S}$ and the Biot strain measure $\mathbf{E}_{(1/2)} = \mathbf{U} - \mathbf{1}$:

$$\mathbf{S} = \mathbb{C} : \mathbf{E}_{(1/2)}, \tag{140}$$

where $\mathbf{U} = \left(\mathbf{F}^T\mathbf{F}\right)^{\frac{1}{2}}$ denotes the right stretch tensor, and $\mathbf{U} = \mathbf{F}$ for the special case when $\mathbf{F}$ is symmetric (i.e. for all pre-defined load cases, entailing zero material spin). The Cauchy stress $\boldsymbol{\sigma}$ is subsequently computed via the following push-forward operation:

$$\boldsymbol{\sigma} = \frac{1}{J}\mathbf{F}\mathbf{S}\mathbf{F}^T. \tag{141}$$

Despite the description given in the manual consistent with the above, the current implementation in DYNA3D utilizes the Green-Lagrange strain tensor $\mathbf{E} = \frac{1}{2}\left(\mathbf{C} - \mathbf{1}\right)$ in lieu of the Biot strain. This is done for the sake of numerical efficiency and simplicity in the ensuing computations.

In what follows, consider the special case of isotropic elasticity with the Lamé parameter $\lambda = 0$ ($\nu = 0$):

$$\mathbf{S} = 2\mu\,\mathbf{E}, \tag{142}$$

and when $\mathbf{U} = \mathbf{F}$:

$$\boldsymbol{\sigma} = \frac{\mu}{J}\left[\mathbf{U}^4 - \mathbf{U}^2\right]. \tag{143}$$

Additionally, if $\mathbf{U}$ is diagonalizable such that $\mathbf{U} = \mathbf{Q}\boldsymbol{\Lambda}\mathbf{Q}^T$, where $\boldsymbol{\Lambda}$ is a diagonal tensor with $\lambda_3 = 1$, and $\mathbf{Q}$ is an orthogonal tensor, then

$$\mathbf{Q}^T\boldsymbol{\sigma}\mathbf{Q} = \begin{bmatrix} 2\mu\frac{\lambda_1}{\lambda_2}E_1 & 0 & 0 \\ 0 & 2\mu\frac{\lambda_2}{\lambda_1}E_2 & 0 \\ 0 & 0 & 0 \end{bmatrix}, \tag{144}$$

where $E_i = \frac{1}{2}(\lambda_i^2 - 1)$ and $E_1 = -E_2$, $E_3 = 0$. For the particular case of $\mathbf{Q} = \mathbf{1}$, the above yields a direct expression for $\boldsymbol{\sigma}$.

The kinematic formulation test exploits the above conditions, utilizing load case 2 ($\bar{\gamma} = 0.01$) and the material parameterization given in table 135. The results are presented in table 136 and figure 81, indicating that the expected behavior is achieved with all metrics measuring errors on the order of machine precision across all levels of temporal refinement.

However, a negative rate of convergence in the stress error metric is obtained as a consequence of the chosen constitutive update algorithm. In particular, the hyper-elastic formulation option maintains consistency with the (default) hypo-elastic implementation by computing and utilizing a strain increment for each time step, obtained by direct differencing of the total hyper-elastic strain measure:

$$\Delta\mathbf{E}_k^{k+1} = \mathbf{E}(t_{k+1}) - \mathbf{E}(t_k). \tag{145}$$

In so doing, however, round-off errors on the order of $O(\Delta t^{-1})$ are introduced into the computations, leading to a counter-intuitive increase in the relative solution errors as the time step size is decreased. Nonetheless, the obtained results are consistent with this anticipated behavior.

Table 135: Material parameterization for the kinematic formulation test.

Parameter	Value
Elastic modulus, E	2.0
Poisson's ratio, ν	0.0
Kinematic formulation flag	1

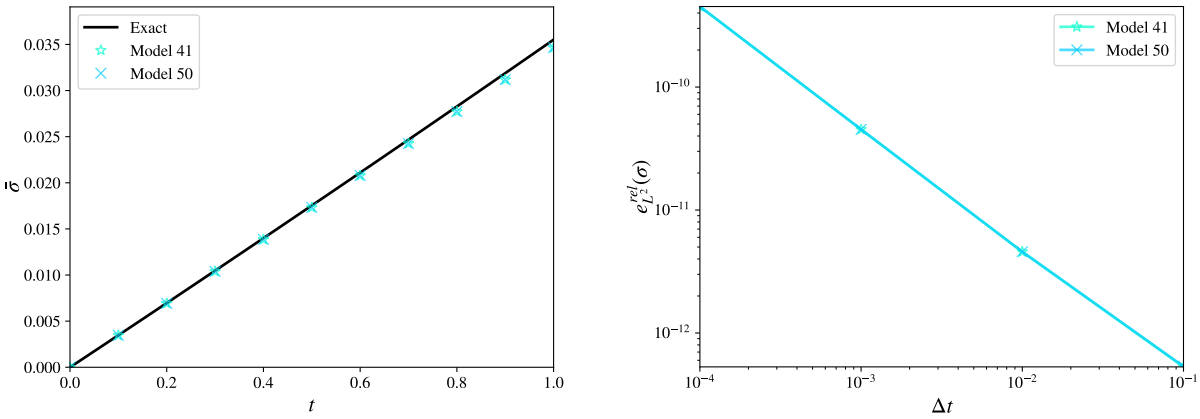

(a) Time-history plot of $\bar{\sigma}$ vs. t using $\Delta t = 0.1$.

(b) Convergence plot for $e_{L^2}^{\text{rel}}(\boldsymbol{\sigma})$ errors vs. Δt.

Figure 81: Kinematic formulation test.

Table 136: Computed errors for the kinematic formulation test.

Model	$e_{L^2}^{\text{rel}}(\boldsymbol{\sigma})$	r	$e_{L^2}^{\text{abs}}(\varepsilon_{33})$	r	$e_{L^2}^{\text{abs}}(\bar{\varepsilon}^p)$	r	Status
41	4.516e-10	-1.00	0.000e+00	-	0.000e+00	-	✓
50	4.518e-10	-1.00	0.000e+00	-	0.000e+00	-	✓

As an aside: it is advised that the present implementation of the hyper-elastic kinematic formulation option be revisited (or deprecated). Specifically, the second Piola-Kirchhoff stress tensor is presently decomposed into pseudo-deviatoric and volumetric parts, and used directly within the radial return-mapping plasticity algorithm of model 50. However, because the pseudo-deviatoric part of the second P-K stress is not properly work-conjugated with an isochoric strain measure, the classical assumptions of incompressible plastic flow are consequently violated. A proposed solution to the aforementioned modeling inconsistency entails the use of the Lagrangian logarithmic (Hencky) strain measure instead of the Green-Lagrange or Biot strain measures, albeit at the expense of computing the matrix logarithm of $\mathbf{U}$.

4.6.7 Bilinear Stiffening

Model 41 allows for a material stiffening effect to emulate the initial slackness in woven fabrics. During the initial stages of tensile loading, the longitudinal stiffness in any in-plane direction is proportional to $E_{\text{soft}} = E\delta$, where δ is the ratio of the initially soft longitudinal modulus E_{soft} to the fully stiffened modulus E.

The uniaxial tensile behavior of the material is such that a linear elastic response with modulus E_{soft} is obtained for all values of axial stress $\sigma < \sigma_{sl}$. For $\sigma > \sigma_{sl}$, the material gradually stiffens according to the following transition formula expressed in terms of the corresponding axial strain ε:

$$\sigma = \begin{cases} E_{\text{soft}}\varepsilon & \varepsilon \le \sigma_{sl}/E_{\text{soft}} \\ y_c - \sqrt{R_{fil}^2 - (E\varepsilon - x_c)^2} & \sigma_{sl}/E_{\text{soft}} < \varepsilon \le \left(x_c + \sqrt{R_{fil}^2/2}\right)/E \\ y_c - x_c - 2\sqrt{R_{fil}^2/2} + E\varepsilon & \varepsilon > \left(x_c + \sqrt{R_{fil}^2/2}\right)/E \end{cases}, \tag{146}$$

where

$$x_c = \sigma_{sl}/\delta - R_{fil}\cos(\beta), \qquad y_c = \sigma_{sl} + R_{fil}\sin(\beta), \qquad \beta = \tan^{-1}(1/\delta), \tag{147}$$

defines the center of the circle with radius R_{fil} in stress space (i.e. $E\varepsilon$ vs. σ) which defines the fillet transition between soft and stiff behavior.

Appropriate biaxial tensile loading conditions consistent with the uniaxial transition behavior described in equation (146) are obtained for load case 1 ($\bar{\gamma} = 0.2$) and the material parameterization given in table 137. The results are depicted in figure 82 and table 138, confirming the expected bilinear stiffening behavior of the model, with a brief fillet transition region.

Table 137: Material parameterization for the model 41 stiffening test

Parameter	Value
Elastic modulus, E	2.0
Poisson's ratio, ν	0.0
Ratio of soft E to stiff E, δ	0.5
Stress value at transition, σ_{sl}	0.1
Fillet radius for transition, R_{fil}	0.2

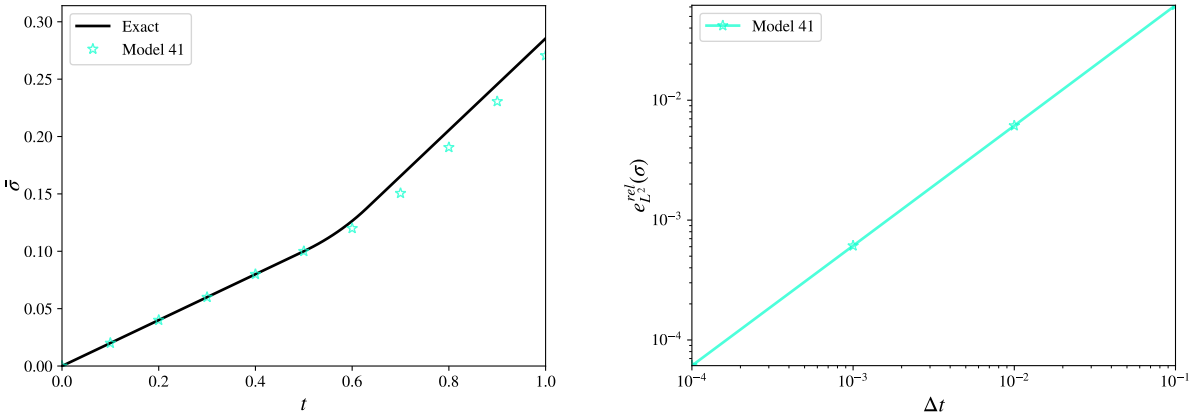

(a) Time-history plot of $\bar{\sigma}$ vs. t using $\Delta t = 0.1$.

(b) Convergence plot for $e^{\text{rel}}_{L^2}(\boldsymbol{\sigma})$ errors vs. Δt.

Figure 82: Model 41 stiffening test.

Table 138: Computed errors for the model 41 stiffening test.

Model	$e^{\text{rel}}_{L^2}(\boldsymbol{\sigma})$	r	$e^{\text{abs}}_{L^2}(\varepsilon_{33})$	r	$e^{\text{abs}}_{L^2}(\bar{\varepsilon}^p)$	r	Status
41	6.108e-05	1.00	0.000e+00	-	0.000e+00	-	✓

4.6.8 Laser Option (Model 23)

Model 23 allows for the optional specification of laser-induced heating effects, prescribed via a collection of load curves to determine the radius of the laser heat source as a function of time, and the normalized thermal profile of the laser as a function of radial distance from the spot center $\mathbf{x}_s$ (assumed as a fixed location).

The intensity of the laser is varied in time by means of an additional load curve defining the global temperature time history, specified via thermal option 1. Model 23 implicitly assumes that the amplitude of the thermal profile is uniformly scaled by the load curve specifying the temperature time history. Temperatures outside of the thermal radius are automatically assigned a value of zero. For the sake of consistency in determining the resulting thermal strains in the surrounding material, the initial ambient temperature (and consequently the initial temperature of the laser heat source) should be prescribed as zero.

The laser option verification test utilizes load case 8 (uniform heating with initial temperature $T_0 = 0$ and heating rate $\bar{T} = 1$, prescribed using a load curve), along with the material parameterization given in table 139. An exact solution for the resulting temperature time history can be surmised from the general solution for isotropic thermal expansion derived in [3]. The correct behavior of the laser option features is consequently confirmed by the results presented in figure 83 and table 140, demonstrating relative errors on the order of machine precision.

Table 139: Material parameterization for the laser option test.

Parameter	Value
Elastic modulus, E	7.5
Poisson's ratio, ν	0.25
Coefficient of thermal expansion, α	0.01
Thermal radius vs. time, $\{(t_i, R_i)\}_{i=1}^{N_{times}}$	$\{(0.0, 0.0), (1.0, 6.0)\}$
Normalized thermal profile vs. radius, $\{(R_i, T_i)\}_{i=1}^{N_{radii}}$	$\{(0.0, 1.0), (1.0, 0.0)\}$
Spot center, $\{x_s, y_s, z_s\}$	$\{1.0, 2.0, 2.0\}$

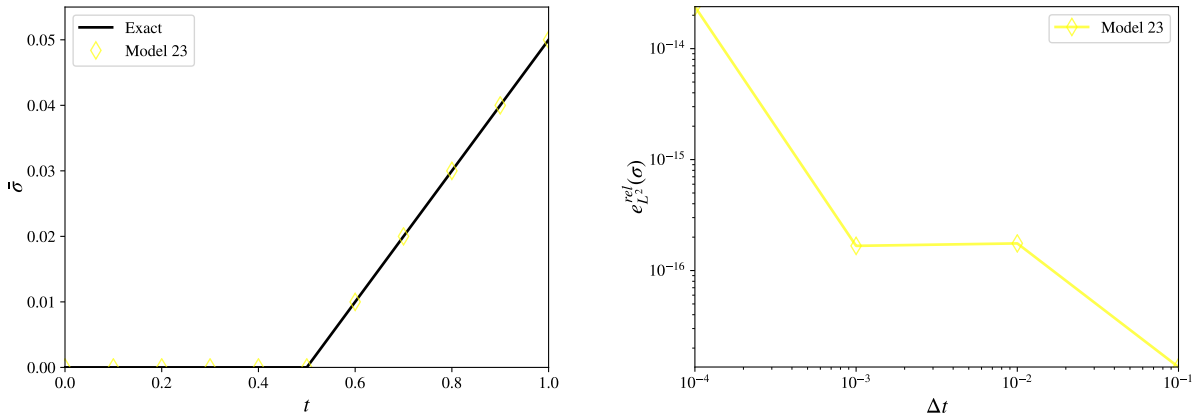

(a) Time-history plot of $\bar{\sigma}$ vs. t using $\Delta t = 0.1$.

(b) Convergence plot for $e_{L^2}^{\text{rel}}(\boldsymbol{\sigma})$ errors vs. Δt.

Figure 83: Model 23 laser option test.

Table 140: Computed errors for the model 23 laser option test.

Model	$e_{L^2}^{\text{rel}}(\boldsymbol{\sigma})$	r	$e_{L^2}^{\text{rel}}(\varepsilon_{33})$	r	$e_{L^2}^{\text{abs}}(\bar{\varepsilon}^p)$	r	Status
23	2.390e-14	-	4.168e-14	-	0.000e+00	-	✓

4.6.9 Strength Differential Ratio

Model 52 permits the specification of a variable strength differential ratio (SDR) between the compressive and tensile yield stresses of the material. If the strength differential option is active, the tabulated yield stresses correspond to their values under tensile loading, whereas the yield stress under compressive loading is scaled by the tabulated SDR values.

Load case 1 is specified with $\bar{\gamma} = \pm 0.2$ for tests 1 (tensile) and 2 (compressive), respectively, with both tests utilizing the material parameterization given in table 141. The results each test are presented in figures 84 and 85, and tables 142 and 143, confirming the expected perfectly plastic material behavior with asymmetric yielding under tensile/compressive loading.

Table 141: Material parameterization for the model 52 SDR tests

Parameter	Value
Elastic modulus, E	2.0
Poisson's ratio, ν	0.0
Yield stress, σ_0	0.1
Flag for strength-differential effect, SD	1
Strength-differential ratio, SDR	1.5

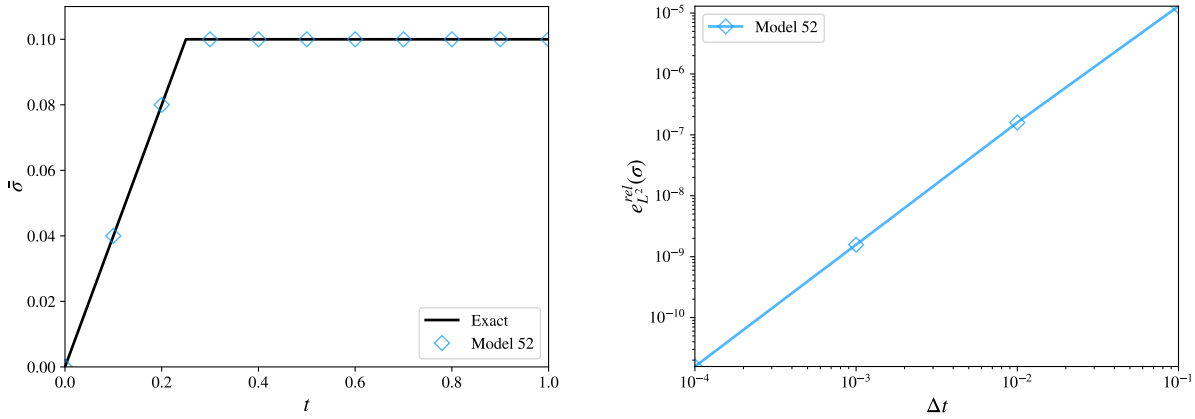

(a) Time-history plot of $\bar{\sigma}$ vs. t using $\Delta t = 0.1$.

(b) Convergence plot for $e^{\text{rel}}_{L^2}(\boldsymbol{\sigma})$ errors vs. Δt.

Figure 84: Model 52 SDR test 1.

Table 142: Computed errors for model 52 SDR test 1.

Model	$e^{\text{rel}}_{L^2}(\boldsymbol{\sigma})$	r	$e^{\text{rel}}_{L^2}(\varepsilon_{33})$	r	$e^{\text{rel}}_{L^2}(\bar{\varepsilon}^p)$	r	Status
52	1.572e-11	1.91	7.439e-11	2.00	7.448e-11	2.00	✓

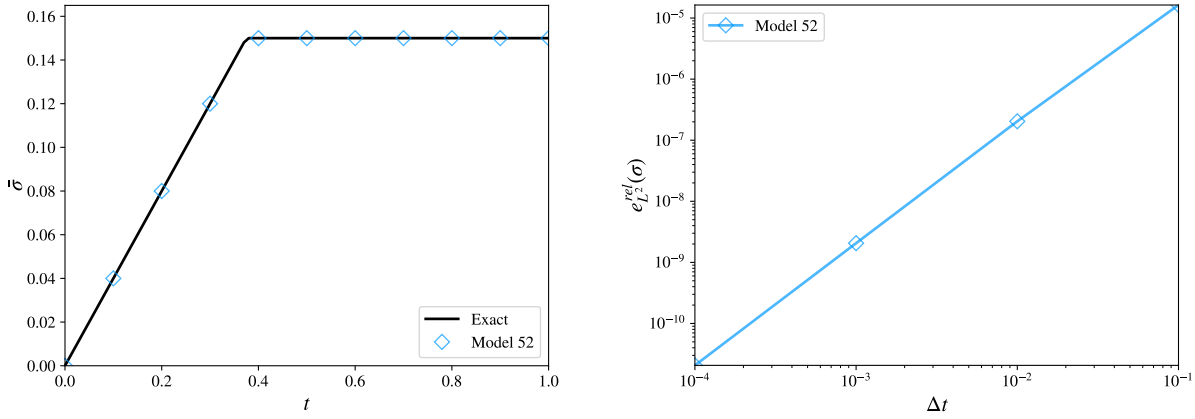

(a) Time-history plot of $\bar{\sigma}$ vs. t using $\Delta t = 0.1$.

(b) Convergence plot for $e^{\text{rel}}_{L^2}(\boldsymbol{\sigma})$ errors vs. Δt.

Figure 85: Model 52 SDR test 2.

Table 143: Computed errors for model 52 SDR test 2.

Model	$e^{\text{rel}}_{L^2}(\boldsymbol{\sigma})$	r	$e^{\text{rel}}_{L^2}(\varepsilon_{33})$	r	$e^{\text{rel}}_{L^2}(\bar{\varepsilon}^p)$	r	Status
52	2.061e-11	1.90	1.011e-10	2.00	1.011e-10	2.00	✓

4.6.10 Randomly Varied Material Properties

Model 15 incorporates randomly varied material properties: the pressure cutoff value p_{cut} and the first and second failure parameters D_1 and D_2 may be randomly distributed according to independent Weibull distributions or load curves defining the inverse CDF for the varied parameter.

Additionally, while model 18 allows for the maximum principal failure stress p_f to randomly vary according to a Weibull distribution with an optional offset value, this option is not valid for shell elements.

For a given random variable X (where X is used to denote one of p_{cut}, D_1, or D_2 for model 15), the probability $p(x)$ that a given material point will possess a value of $x \geq 0$ for the selected random variable is determined by the Weibull distribution:

$$p(x) = \frac{w}{\lambda}\left(\frac{x}{\lambda}\right)^{w-1} e^{-\left(\frac{x}{\lambda}\right)^{w}}, \tag{148}$$

where $w > 1$ is the Weibull modulus (the shape parameter), and λ is the scale parameter for the Weibull distribution. The mode $x_m = \lambda(1-1/w)^{1/w}$ may be used to specify an alternative parameterization in terms of w and x_m:

$$p(x) = \frac{w-1}{x}\left(\frac{x}{x_m}\right)^{w} e^{\frac{1-w}{w}\left(\frac{x}{x_m}\right)^{w}}. \tag{149}$$

The associated cumulative distribution function $F_X(x)$ for the Weibull random variable then takes the form:

$$F_X(x) = 1 - e^{\frac{1-w}{w}\left(\frac{x}{x_m}\right)^{w}}, \tag{150}$$

and its inverse yields:

$$x(F_X) = x_m\left(\frac{w}{1-w}\log(1-F_X)\right)^{\frac{1}{w}} \quad \forall F_X \in [0,1). \tag{151}$$

If x is expressed within a shifted coordinate system $x = x' - x'_0$ for some $x'_0 \in \mathbb{R}$ (as is the case for model 18), then one may write

$$x'(F_X) = x'_0 + x_m\left(\frac{w}{1-w}\log(1-F_X)\right)^{\frac{1}{w}}, \tag{152}$$

where $x' \geq x'_0$ if $x \geq 0$. Consequently, x'_0 may be interpreted as a strict lower bound on $x' \in [x'_0, +\infty)$.

It should be emphasized that x_m is the mode (not the mean) of the Weibull distrubtion. Rather, the mean (herein denoted $\bar{x}$) is given by $\bar{x} = \lambda\,\Gamma(1+1/w)$, where $\Gamma(\cdot)$ denotes the Gamma function (an extension of the factorial function to non-integer arguments). Moreover, $x'_m = x'_0 + x_m$ is the mode (not the mean) of the shifted Weibull distribution (expressed in terms of the shifted coordinate x'). This conflicts with the terminology used to describe material model 15 (and 18) in the DYNA3D manual, which claims that the aforementioned quantities are the "mean average values" of the Weibull distrubition.

The correct Weibull distribution for each of the aformentioned random variables ($X = p_{cut}$, D_1, D_2) is verified by examining the resulting variation in material properties generated for a discrete sample size of N shell elements. For simplicity, the commonly defined set of parameters in table 144 are utilized for each random variable, yielding identical parameter distributions. For a given sample size N, a fitted Weibull distribution is computed from the randomly generated material property data, and compared against the exact Weibull distribution in the $e^{\text{rel}}_{L^2}(p(x))$ error metric, where $p(x)$ denotes the corresponding probability density function expressed in terms of a given random value $x \in X$. Convergence of these errors with respect to increasing sample size N indicates that the resulting randomly generated distribution of material parameters agrees with the chosen Weibull input parameters. This result is confirmed by figure 86 and table 145, demonstrating that the errors for each random variable converge with increasing N, implying that all such features are functioning as intended.

Table 144: Material parameterization for the randomly varied material properties test

Parameter	Value
Weibull-distributed random variable, $X = p_{cut} = D_1 = D_2$	1.0
Weibull modulus (for $X = p_{cut} = D_1 = D_2$), w	2.0
Random number seed value (for $X = p_{cut} = D_1 = D_2$), *seed*	1

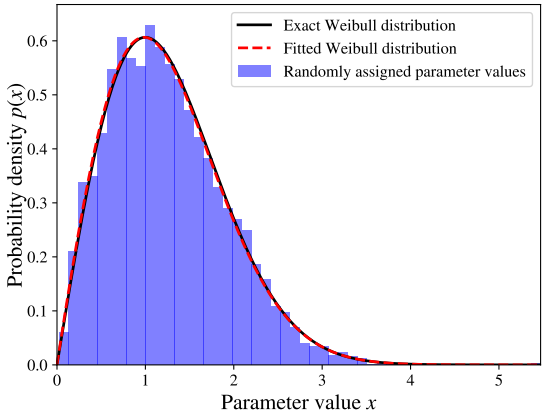

(a) Identical probability density $p(x)$ vs. x for each randomly varied parameter ($X = p_{cut}$, D_1, D_2) using 4096 elements.

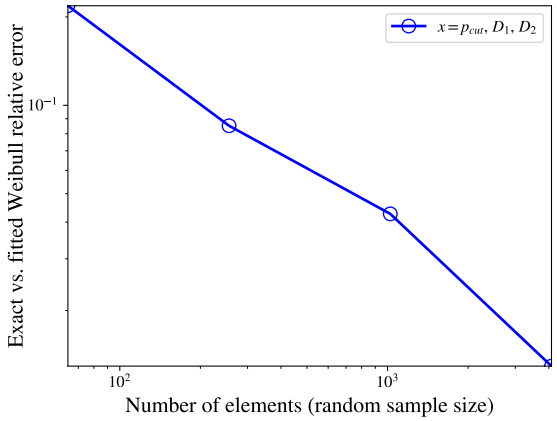

(b) Convergence plot for $e^{\text{rel}}_{L^2}(p(x))$ errors vs. number of elements.

Figure 86: Randomly varying material property tests.

Table 145: Computed errors for the Weibull-distrubted parameter tests

Parameter x	$e^{\text{rel}}_{L^2}(p(x))$	r	Status
p_{cut}	1.293e-2	0.50	✓
D_1	1.293e-2	0.50	✓
D_2	1.293e-2	0.50	✓

A separate issue which should be regarded as a potential validation effort concerns the means by which random material properties are assigned to a given mesh. The present approach consists of selecting a random number $r \in [0, 1)$ for a given element (or quadrature point, as the case may be), and then evaluating $x'(r)$ to determine the randomly varied material property at the chosen location in the mesh. For a fixed discretization, consistent results between repeated analyses are guaranteed through the use of a random number seed value. However, consistency under mesh refinement is not guaranteed, since the random number drawing sequence depends upon a given element's global index, rather than its spatial position. Moreover, randomly varied properties are presumed to lack spatial regularity, and may therefore be randomly assigned without regard for the properties assigned to neighboring material points. The implications of such a procedure result in mesh-dependent failure of a given specimen due to the chosen (spatially uncorrelated) random sampling process. At present, these concerns regarding the validation of model 15 (and 18) are deemed to be beyond the scope of the present verification efforts. Nonetheless, it is recommended that these issues be revisited at a later time.

5 Conclusions and Future Work

In supplement to the previous work [3], the verification test suite collectively proposed in parts 1 and 2 of this effort comprehensively test all of the currently available features for shell element material models in DYNA3D. Moreover, the chosen methodology used to verify all tested features establishes a high degree of fidelity for the broad functionality of each material model.

In addition to creating and documenting the results of the currently proposed suite of verification tests, a substantial effort was also invested in developing an extensible testing infrastructure with the purpose of generating and documenting additional verification tests more easily. It is intended that this framework be used to extend the current suite of tests for shell models to establish a similar such suite of comprehensive verification tests for solid elements.

Tables 146 and 147 provide prospective users with an indication of a given model's level of fidelity in terms of the scope of its currently tested features.

5.1 Resolved Issues

In process of creating the proposed verification suite, examination of the results for each test led to the discovery of 24 independent shell model-related issues. Each discovered issue was subsequently documented in Jira, and later resolved. For reference, a short description (the Jira ticket name) of each issue is provided below, along with its corresponding Jira ticket number. For specific details regarding each issue, the reader is referred to the corresponding documentation for each ticket in Jira.

PARADYN-150: Shell model 15 computes spall incorrectly, or not at all

PARADYN-151: The DYNA3D manual incorrectly states the failure criteria for models 22 and 41

PARADYN-152: The DYNA3D manual incorrectly states the delamination failure criteria for model 74

PARADYN-153: The DYNA3D manual incorrectly states the pincipal strains for model 74

PARADYN-165: Shell model 46 disallows the use of AOPT = 3

PARADYN-166: Shell model 50 sets the material offset angle incorrectly for AOPT=3

PARADYN-167: Shell model 41 sets the "hyper" flag incorrectly

PARADYN-168: Added integration point failure flag history variable to model 54

PARADYN-169: Adjusted sound speed for shell models 19, 22, 41

PARADYN-170: Shell model 54 issues failed convergence warning despite achieving convergence

PARADYN-175: Model 39 utilizes incorrect/inconsistent definition of effective stress in triaxiality-dependent damage update

PARADYN-176: Shell model 22 does not exhibit non-linear shear stress-strain response

PARADYN-177: Model 35 uses incorrect strain ratio for failure when IFLD = 2 or 3

PARADYN-178: Improved accuracy of offset pressure computation for model 35

PARADYN-179: Added input checking for select model 52 material parameters

PARADYN-180: Shell models 4 and 23 do not apply the shear correction factor to transverse shear stresses

PARADYN-181: Model 23 handles temperature-dependent thermal expansion differently from other models

PARADYN-182: Model 52 extrapolates invalid yield stresses at small strain rates

PARADYN-186: Improve accuracy of shell model 23's laser option computations

PARADYN-187: Shell model 52's strength-differential effect exhibits sudden jump in yield stress

PARADYN-188: Behavior of shell model 23's laser option needs clarification

PARADYN-189: Shell model 42 prints inconsistent variables to 7-th slot in hsp element print blocks for orthotropic shell models

PARADYN-191: Provide input checking for the strain rate-dependence coefficient in model 15

PARADYN-192: Shell model 50 does not implement the use of the fiber tensile saturation stress

5.2 Final Summary of Verification Test Results

Tables 146 and 147 provide a complete summary of the determined verification status of all tested features for shell element material models in DYNA3D. A "passing" status (✓) for a specific test is reserved only for those models which have been thoroughly verified to be consistent with the exact mathematical solutions for all feature-specific problems, and consistent with the assumptions made by other relevant models in DYNA3D. In this regard, prospective users of a given feature can be assured that the indicated models are functioning correctly.

Table 146: Verification status of shell model features tested in [3]

Model	Isotropic Elasticity	Orthotropic Elasticity	Isotropic Thermal Expansion	Orthotropic Thermal Expansion	Linear Hardening	Piecewise Hardening	Power-Law Hardening	Exponential Hardening	Hill Yield Criterion	Linear Rate-Hardening	Logarithmic Rate-Hardening	Drucker-Prager Yield Criterion
1	✓	-	-	-	-	-	-	-	-	-	-	-
2	✓	✓	-	-	-	-	-	-	-	-	-	-
3	✓	-	-	-	✓	-	-	-	-	-	-	-
4	✓	-	✓	-	✓	-	-	-	-	-	-	-
12	✓	-	-	-	✓	-	-	-	-	-	-	-
15	✓	-	-	-	✓	-	✓	-	-	-	-	✓
18	✓	-	-	-	-	-	✓	-	-	-	-	-
19	✓	-	-	-	✓	-	-	-	-	-	-	-
21	✓	✓	✓	✓	-	-	-	-	-	-	-	-
22	✓	✓	-	-	-	-	-	-	-	-	-	-
23	✓	✓	✓	✓	-	-	-	-	-	-	-	-
24	✓	-	-	-	✓	✓	✓	-	-	✓	-	✓
28	⚠	-	-	-	⚠	-	-	-	-	-	-	-
30	✓	-	-	-	✓	-	-	-	-	-	-	-
33	✓	✓	-	-	✓	-	-	-	✓	-	-	-
34	✓	-	-	-	✓	-	-	-	⚠	-	-	-
35	✓	-	-	-	✓	✓	-	-	-	-	-	-
38	✓	-	-	-	✓	-	-	-	-	-	-	-
39	✓	-	-	-	✓	-	-	-	-	-	-	-
41	✓	✓	-	-	-	-	-	-	-	-	-	-
42	-	-	-	-	-	-	-	-	-	-	-	-
46	✓	✓	-	-	-	-	-	-	-	-	-	-
50	✓	✓	-	-	-	-	-	-	-	-	-	-
52	✓	-	-	-	✓	✓	-	-	-	-	-	-
54	✓	-	-	-	✓	-	✓	-	-	✓	-	-
71	✓	-	✓	-	✓	-	✓	✓	-	✓	✓	✓
74	✓	✓	-	-	-	-	-	-	-	-	-	-

✓: Passed all verification tests.
⚠: Inconsistent model assumption.
✗: Failed one or more verification tests.
?: Model feature currently remains untested.

Table 147: Verification status of newly proposed tests for shell material models in DYNA3D

Model	Kinematic Hardening (4.1)	Temp.-Dependent Elasticity (4.2.1)	Temp.-Dependent CTE (4.2.2)	Temp.-Dependent Plasticity (4.2.3-4.2.5)	Heat Generation & Softening (4.2.6)	Strain Rate-Dependent Plasticity (4.3)	Baumann Plasticity (4.4)	Minimum Time Step Deletion (4.5.1)	Plastic Strain Deletion (4.5.2)	Instantaneous Failure (4.5.3-4.5.6)	Progressive Damage (4.5.7-4.5.10)	Shear Correction Factor (4.6.1)	Material Axes Options (4.6.3)	Debug Run (4.6.4)	Non-linear Shear (4.6.5)	Kinematic Formulation (4.6.6)	Misc. (4.6.7-4.6.10)
1	-	-	-	-	-	-	-	-	-	-	-	✓	-	-	-	-	-
2	-	-	-	-	-	-	-	-	-	-	-	✓	✓	✓	-	-	-
3	✓	-	-	-	-	-	-	-	-	-	-	✓	-	-	-	-	-
4	-	✓	⚠	✓	-	-	-	-	-	-	-	✓	-	-	-	-	-
12	-	-	-	-	-	-	-	-	-	-	-	✓	-	-	-	-	-
15	-	-	-	✓	✓	✓	-	✓	-	✓	-	✓	-	-	-	-	✓
18	-	-	-	-	-	-	-	-	✓	-	-	✓	-	-	-	-	-
19	-	-	-	-	-	✓	-	✓	-	✓	-	✓	-	-	-	-	-
21	-	-	-	-	-	-	-	-	-	-	-	✓	✓	-	-	-	-
22	-	-	-	-	-	-	-	✓	-	✓	-	✓	✓	-	✓	-	-
23	-	✓	✓	-	-	-	-	-	-	-	-	✓	✓	-	-	-	✓
24	-	-	-	-	-	-	-	✓	✓	-	-	✓	-	-	-	-	-
28	-	-	-	-	-	-	-	-	-	-	-	✓	-	-	-	-	-
30	✓	-	-	-	-	-	-	-	-	-	-	✓	-	-	-	-	-
33	-	-	-	-	-	-	-	-	-	-	-	✓	✓	-	-	-	-
34	-	-	-	-	-	-	-	-	-	-	-	✓	-	-	-	-	-
35	-	-	-	-	-	✓	-	-	⚠	✓	-	✓	-	-	-	-	-
38	✓	-	-	-	✓	-	✓	-	-	-	-	✓	-	-	-	-	-
39	✓	-	-	-	✓	-	✓	-	-	-	✓	✓	-	-	-	-	-
41	-	-	-	-	-	-	-	✓	-	✓	-	✓	✓	-	✓	✓	✓
42	-	-	-	-	-	-	-	-	-	-	-	-	-	-	-	-	-
46	-	-	-	-	-	-	-	-	-	-	-	✓	✓	✓	-	-	-
50	-	-	-	-	-	-	-	✓	-	-	✓	✓	✓	-	-	✓	-
52	-	-	-	-	✓	✓	-	✓	✓	-	✓	✓	-	-	-	-	✓
54	-	-	-	✓	✓	✓	-	✓	✓	-	-	✓	-	-	-	-	-
71	-	-	✓	✓	✓	-	-	-	✓	-	-	✓	-	-	-	-	-
74	-	-	-	-	-	-	-	-	-	-	✓	✓	✓	-	-	-	-

✓: Passed all verification tests.
⚠: Inconsistent model assumption.
✗: Failed one or more verification tests.
?: Model feature currently remains untested.

References

[1] D. Bammann, M. Chiesa, Mark Horstemeyer, and L. Weingarten. Failure in ductile materials using finite element methods. *Structural Crashworthiness and Failure*, pages 1–54, 1993.

[2] Fu-Kuo Chang and Kuo-Yen Chang. Post-failure analysis of bolted composite joints in tension or shear-out mode failure. *Journal of Composite Materials*, 21(9):809–833, 1987.

[3] B.D. Giffin. Shell Element Material Model Verification Problems for DYNA3D. Technical Report LLNL-TR-792469, Lawrence Livermore National Laboratory, 2019.

[4] R W Logan, D B Thomas, and G K Young. Implementation of a pressure and rate dependent forming limit diagram model into nike and dyna. 6 1995.

[5] E. Zywicz and B. D. Giffin. *DYNA3D: A Nonlinear, Explicit, Three-Dimensional Finite Element Code for Solid and Structural Mechanics User Manual - Version 19*. Lawrence Livermore National Laboratory, October, 2019.